이학박사 학위논문

Investigation of quasiparticle band gaps and exciton binding energies in bulk transition metal dichalcogenides

벌크 전이금속 칼코겐화합물의 준입자 밴드 갭 및 엑시톤 결합 에너지에 대한 연구

2019 년 2 월

서울대학교 대학원

물리천문학부

김 범 서

Investigation of quasiparticle band gaps and exciton binding energies in bulk transition metal dichalcogenides

Beom Seo Kim

Supervised by

Professor Changyoung Kim

A Dissertation submitted to the Faculty of Seoul National University in Partial Fulfillment of the Requirements for the Degree of Doctor of Philosophy

February 2019

Department of Physics and Astronomy

Graduate School

Seoul National University

ABSTRACT

Investigation of quasiparticle band gaps and exciton binding energies in bulk transition metal dichalcogenides

Beom Seo Kim
Department of Physics and Astronomy
The Graduate School
Seoul National University

Recently, atomically thin two-dimensional (2D) materials have been drawn much attention due to their possibility of application as well as extraordinary physical properties that encompass insulator (h-BN), semiconductors (Group 6, 7 transition metal dichalcogenides / black phosphorus), semimetal (Graphene), and metal (Group 5 transition metal dichalcogenides). These 2D materials can cover a broad range of electrical and optical properties due to their sizable or zero band gap but also tunable band gap. Especially, bulk semiconducting transition metal dichalcogenides (TMD) often exhibit qualitatively different physical properties compared to their monolayer. In this thesis, I explore electronic structure of direct/indirect band gap semiconductors in the bulk form using angle-resolved photoemission spectroscopy (ARPES), optical spectroscopy (OS), and scanning tunneling microscopy (STM).

First of all, I study electronic band structure of bulk MX_2 (M = Mo, W; X = S, Se) via ARPES. Among the TMD, the group 6 TMD, MX_2 exhibit interesting

electronic properties such as indirect (bulk) to direct (monolayer) band gap transition, valley degeneracy and spin-orbit interaction induced spin band splitting at the K and $-$K points of the hexagonal Brillouin zone. Although monolayer MX_2 is interesting due to the direct band gap, the information on the electronic structure of bulk MX_2 is also important as stacked layers affect the electronic structure. In this study, I extract all the electronic band parameters of bulk MX_2 from the ARPES data and compare the results with those of previously studied MX_2 thin films including monolayer.

Secondly, I study electric field effect on the band gap in bulk $MoSe_2$. Direct band gap plays the central role in optoelectronic applications including light emitting and laser diodes. In this regard, monolayer MX_2 has emerged as a new class of nanomaterials due to its novel optoelectronic properties stemming from the direct band gap and valley degeneracy. Unfortunately, the more practically usable bulk and multilayer MX_2 have indirect band gaps. Therefore, it is highly desired to turn bulk/multilayer MX_2 into direct band gap semiconductors by controlling external parameters. In this study, I suggest the possibility for electric field induced indirect to direct band gap transition in bulk $MoSe_2$ using alkali metal dosing ARPES which can mimic the situation of surface electric field. This can pave the way towards optoelectronic application of bulk materials.

Thirdly, I study electronic band structure of bulk ReX_2 (X = S, Se). ReX_2 materials have one-dimensional (1D) characters in their crystal structure as well as optical and electrical properties due to the formation of Re chain structure stemming from the distortion in the 1T structure phase. More interestingly, ReX_2 has much weaker layer-layer interaction than other layered TMD. In spite of these interesting properties, systematic studies on the 1D character of charge carriers have not been done yet. In this study, I demonstrate systematic and comparative studies on the energy-momentum dispersion relationships and extract effective mass of hole carriers along the all k direction of ReX_2 using ARPES.

Lastly, I study exciton binding energy of bulk ReX_2. Generally, monolayer

semiconductors have extremely large exciton binding energy in comparison to the bulk form due to the reduced electronic screening and strong Coulomb interaction. However, ReX_2 has very weak layer-layer interaction which indicates almost isolated 2D nature. From ARPES data, I find that $ReSe_2$ has extremely weak layer-layer interaction in spite of bulk form. In this study, I find large exciton binding energy in bulk $ReSe_2$ subtracting optical band gap from electronic band gap which can be achieved by OS (optical band gap) and STM (electronic band gap). Such large exciton binding energy in bulk $ReSe_2$ opens up the possibility for optoelectronic device application and/or studying exciton related many-body physics.

Key Words : Angle-resolved photoemission spectroscopy, transition metal dichalcogenides, indirect band gap semiconductor, direct band gap semiconductor, exciton binding energy, $in\text{-}situ$ alkali metal dosing, electronic structure.

Contents

List of Figures

List of Tables

1 Introduction

In this chapter, I will introduce the history of the research in layered material. Since the discovery of graphene, enormous amounts of research on layered materials including transition metal dichalcogenides (TMDs) have emerged in the physics community. TMD can be classified by the location of the constituent atoms in the periodic table. Especially, group 6 and 7 TMDs not only have semiconducting properties which can be useful for device application but also have extraordinary physical properties such as indirect to direct band gap transition or anisotropic electronic structure. I will briefly describe crystal structures, experimental/theoretical electronic structures and physical properties of MX_2 and ReX_2 which are main systems that I studied. The contents of my research during the Ph. D course are described in the theses 'highlights' at the end of this chapter.

1.1 Background

1.1.1 Graphene

Graphite, the base material of graphene, is a crystalline allotrope of carbon and the most stable form of carbon under ambient conditions. Starting from the discovery of zero-dimensional fullerenes (1985)[1], and 1D carbon nanotube (1991)[2], 2D graphene (2004)[3] was discovered, isolated, and characterized. Successful exfoliation and isolation of graphene have stimulated enormous fundamental scientific interest in a wider family of 2D layered materials.

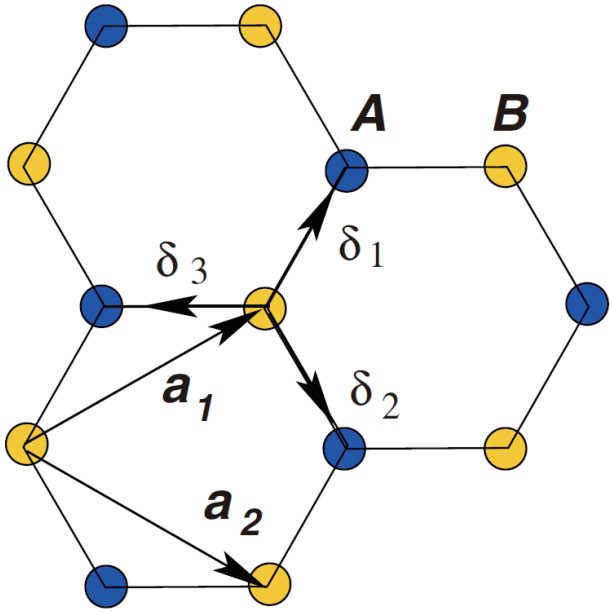

Fig. 1.1: Lattice structure of graphene[4].

Graphene was the subject of explosive research because it not only is the first 2D structure to be isolated, but also has an unusual electronic band structure. Graphene is a 2D single layer of carbon atoms that form sp^2 bonds. It has a hexagonal lattice with two equivalent carbon atoms as sublattice as shown in Figure 1.1[4]. The p_z orbital of a carbon atom plays the crucial role in the electrical and optical properties.

Band structure of graphene shows that valence and conduction bands meet at six points in the Brillouin zone (three at K and other three at $-$K points), so called Dirac point. At Dirac point, the dispersion has a cone shape where band dispersion is linear as shown in Figure 1.2[4]. K and $-$K points are often called K and $-$K valleys. Graphene exhibits different physical properties at K and $-$K valleys. Because of three valleys with different properties, graphene is one of important material in valleytronics.

One important aspect of Dirac points is the unique linear band dispersion as mentioned above. As the Fermi energy at the Dirac point, the carrier type

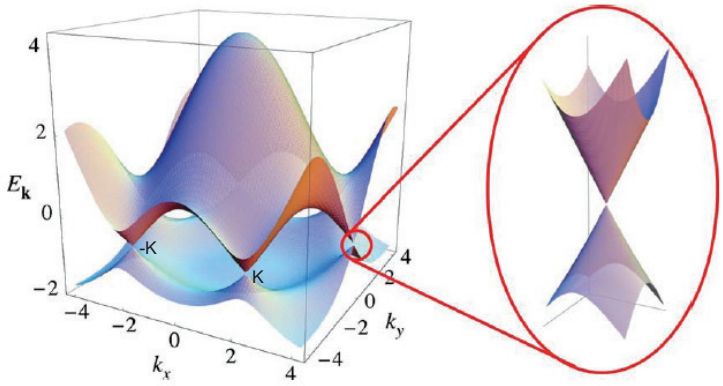

Fig. 1.2: Electronic structure of graphene[4].

changes from hole to electron (or electron to hole) across the Dirac point. Low-energy electron in graphene behaves like massless electrons, so-called massless Dirac fermions. Due to these properties, the motion of low-energy electron in graphene is described by the Dirac equation rather than the usual Schrödinger equation.

1.1.2 Beyond graphene: other layered materials

After the initial discovery of graphene, exfoliation and isolation techniques for graphene were developed and are widely used to exfoliate other layered materials that have strong in-plane covalent and weak out-of-plane van der Waals bonds. Such weak out-of-plane bonding character reduces the dimensionality from 3D to 2D and allows us to obtain monolayer systems by the exfoliation method. Monolayer systems often exhibit qualitatively different electrical and optical properties compared to the bulk systems[5, 6, 7]. For this reason, layered materials have attracted enormous interest in solid state physics community.

There are three families of materials that have played major roles in the research. First, hexagonal boron nitride (h-BN) which is a well known in-

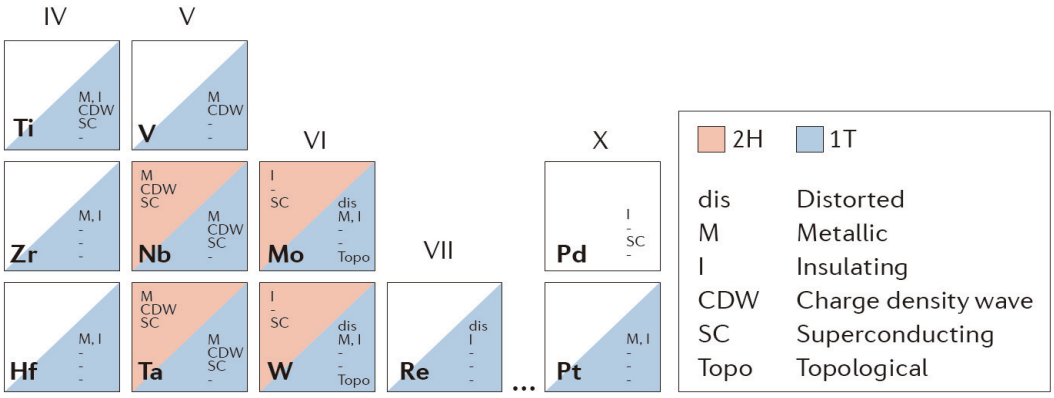

Fig. 1.3: Possible phases of various TMD[10].

sulator is widely used as a substrate for monolayer systems. h-BN is very stable under ambient condition and its wide band gap allows to easily identify monolayer systems using microscopy. Its insulating behavior is also very important for measuring transport properties. For these reasons, most of monolayer systems are transferred onto h-BN and studied.

Second example is black phosphorus. Black phosphorus is a semiconductor which has a tunable band gap from 2 to 0 eV under a surface electric field[8]. Black phosphorus has orthorhombic crystal structure which is not isotropic even in monolayer. Due to the anisotropic crystal structure, its electronic band structure is qualitatively different along the armchair and zigzag direction[9].

Last is transition metal dichalcogenides (TMD) family which are my main systems studied in Ph. D course. TMD consist of one transition metal and two chalcogen atoms (S, Se, Te). In the periodic table, there are variety of transition metal and chalcogen elements which means there should be many combinations between them. As many of the possible combinations are available, variety of physical properties of TMD including superconductivity and charge density waves exist as shown in Fig 1.3[10]. There are also various phases within the same configuration such as 1T, 2H, and 3R

which have octahedral, trigonal prismatic, and trigonal prismatic metal coordination, respectively. In this thesis, I focus only on electronic properties of semiconducting group 6 TMD (MX_2) and group 7 TMD (ReX_2).

1.2 Group 6 TMD MX_2 (M = Mo, W; X = S, Se)

Group 6 TMD, MX_2 material family (MoS_2, $MoSe_2$, WS_2, and WSe_2) have drawn much attention in the condensed matter physics community because of its potential for device applications in optoelectronics, spintronics, and valleytronics. Monolayer MX_2 is especially important because it has direct band gap at K and $-$K points in spite of the indirect band gap in the bulk form. Optical transitions at K and $-$K points can be selectively excited by right- and left-circularly polarized light[11]. The valence band at the K and $-$K points also shows spin-orbit interaction (SOI) induced spin band splitting.

1.2.1 Crystal and electronic structure

MX_2 has a honeycomb lattice structure as graphene does with strong intralayer bonding and weak interlayer bonding. In comparison to graphene, there are two main differences. The first is orbital character. In MX_2 systems, d-electron orbitals which come from the transition metal atom (Mo or W) plays important roles such as large SOI induced spin band splitting. The other is broken inversion symmetry in odd number of layers. In the monolayer case, site A has a transition metal atom and site B has two chalcogen atoms. Due to this different atoms in sublattice A and B sites, odd number of layers of TMD have intrinsic broken inversion symmetry which results in distinct electronic structure from graphene.

On the other hand, in even number of layers, inversion symmetry is restored and inversion center is located between two layers. Figure 1.4 shows crystal structure of MX_2 (2H phase)[12]. Right figure illustrates the side view of MX_2 and one can see that each layer has no inversion center which

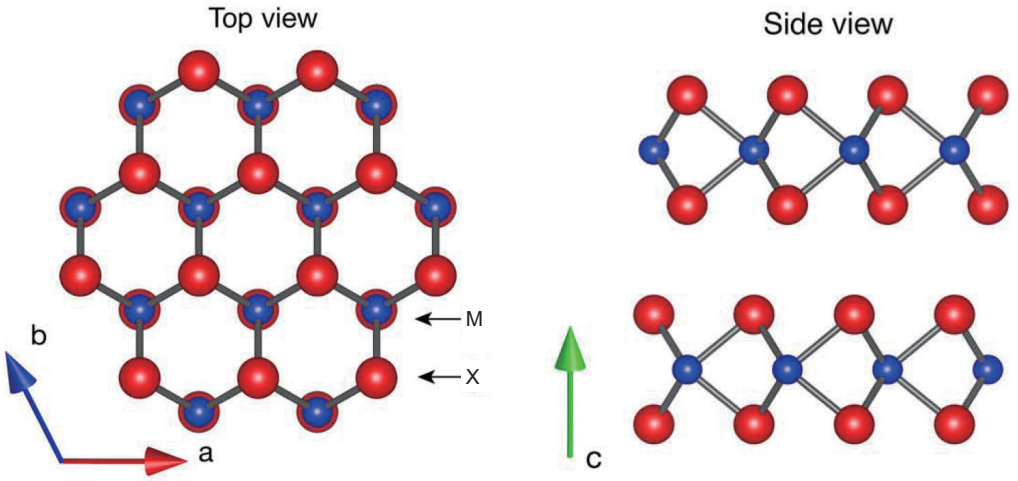

Fig. 1.4: Crystal structure of MX_2. Left figure shows that top view of the crystal structure while right figure is the side view[12].

means intrinsic broken symmetry in monolayer MX_2. Broken inversion symmetry provides other unique advantages for optoelectronics, spintronics, and valleytronics.

Figure 1.5 shows theoretical electronic band structure of monolayer and bulk MX_2 with and without SOI[13]. Here, SOI have same meaning with spin-orbit coupling (SOC) in Figure 1.5. In comparison to the graphene case, instead of a Dirac cone dispersion with zero band gap, it has direct band gap at K and $-$K points in monolayer. This difference in electronic band structure between graphene and MX_2 originates from difference in inversion symmetry.

Bulk and monolayer MX_2 have two main differences. First, in the monolayer limit, there is no valence spin band splitting at K point without SOI. On the other hand, in bulk case, there is valence band splitting in spite of without SOI. Due to the number of layers, except for the monolayer case, there is valence spin band splitting at K point even without SOI.

The other main difference is that monolayer MX_2 has a direct band gap at the K and $-$K points while bulk has an indirect band gap. The valence band

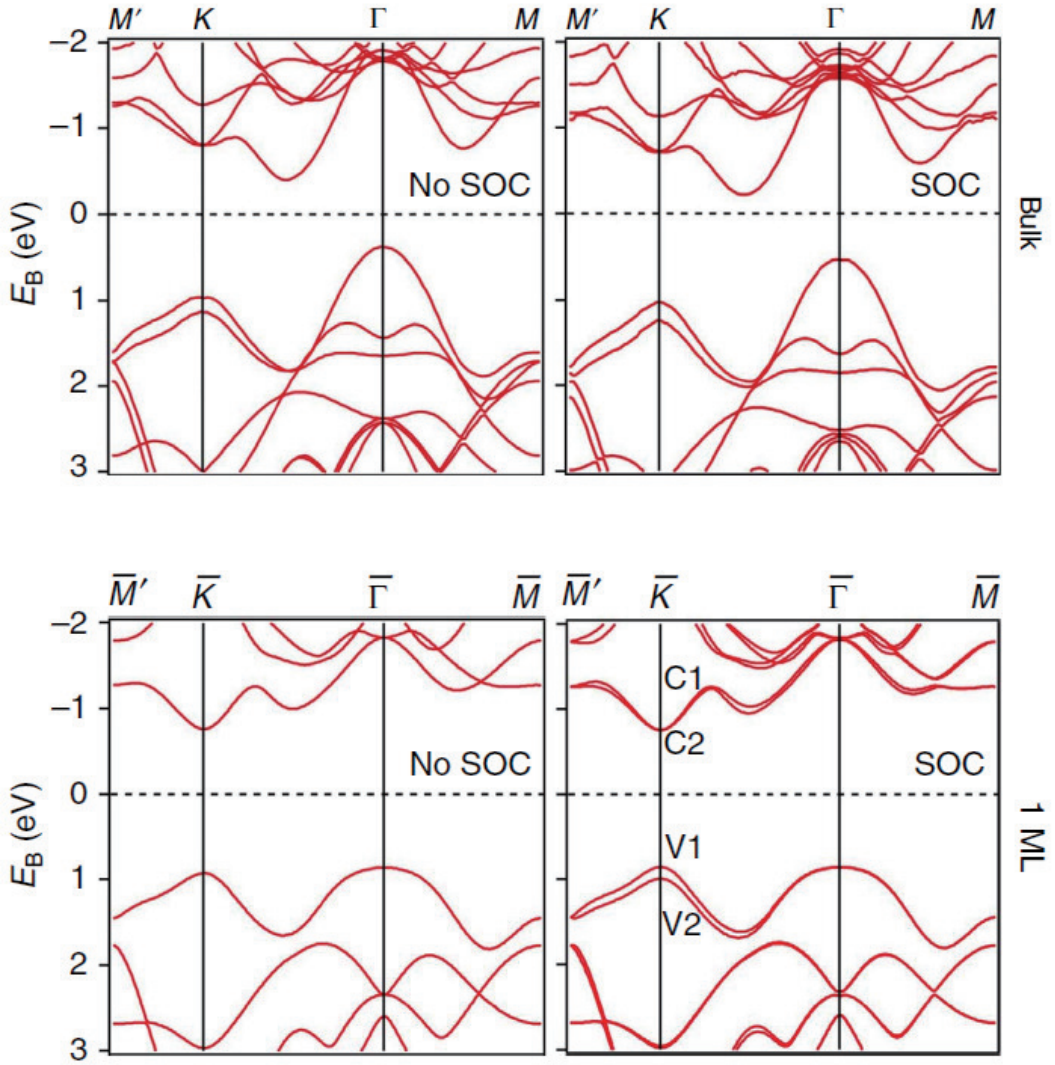

Fig. 1.5: Electronic structures of monolayer and bulk MX_2[13]. Upper figures are bulk band structures while lower figures show monolayer band structures. Left and right figures are for without and with SOI, respectively.

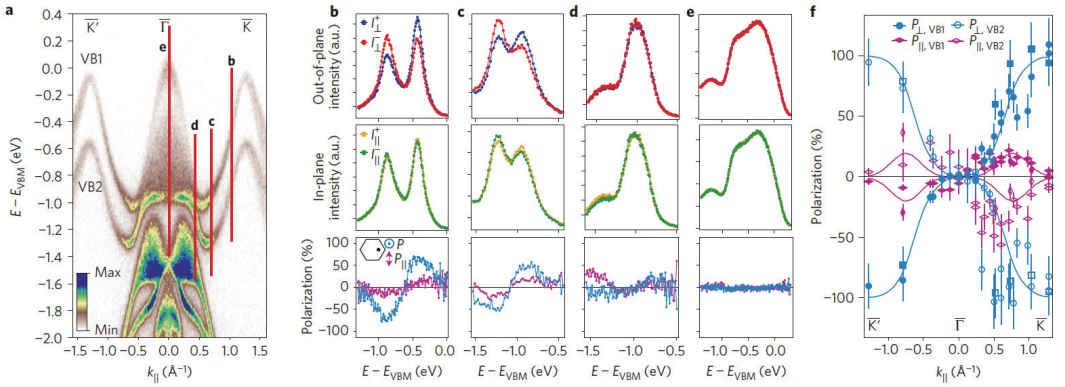

Fig. 1.6: Spin-resolved ARPES data of bulk WSe_2[14]. (a) High symmetry cut ARPES data along the $\Gamma - K$ direction. (b)-(e) Spin resolved energy distribution curves (EDCs) along the lines labelled by the corresponding vertical lines in (a). (f) The out-of-plane ($P_\perp$) and in-plane ($P_{||}$) spin polarization determined from fitting additional EDCs.

maximum and conduction band minimum is located at the K and $-$K points in the monolayer case. On the other hand, the valence band maximum is located at Γ point and conduction band minimum is at the so-called Σ point located between the K and Γ points. The energy of Σ point is influenced by both number of layers and SOI. I will discuss detailed information about the conduction band minimum position of bulk MX_2 in chapter 3.

Another important issue to discuss is on orbital characters at high symmetry points, especially, K and Γ points. At the Γ point, the main orbital character is d_{z^2} of the transition metal atom (Mo and W). On the other hand, the states at K and $-$K points are composed of d_{xy} and $d_{x^2-y^2}$ of the transition metal atom. The contribution from chalcogen orbitals are almost negligible for near E_F states. This is because that the portion of the orbital character is much smaller than transition metal atom and the direction of orbital characters is same with transition metal atom (p_z for Γ point, p_x and p_y for K point). So, inclusion of chalcogen orbitals does not significantly affect the trend of orbital characters.

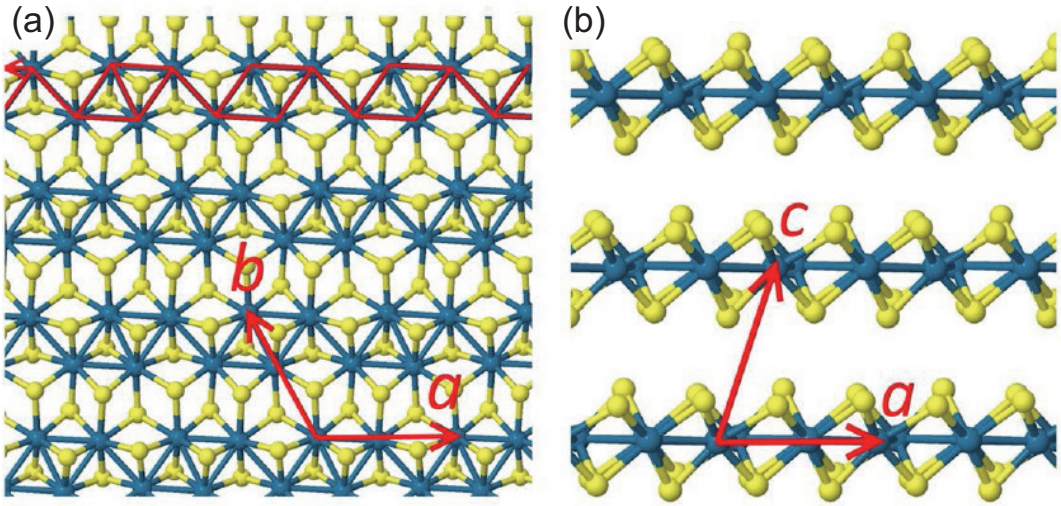

Fig. 1.7: Crystal structure of ReX_2[17]. (a) Top view of the single layer lattice structure. Blue indicates Re atom and Yellow indicates Se atom, respectively. a direction indicates the Re chain direction. (b) Side view of the lattice structure.

1.2.2 Physical property

MX_2 has valley spin related physical properties. In general, valley states refer to degenerate local electronic band structures in the momentum space arising from crystal symmetry. Silicon and GaAs which have diamond-like lattice structure is a well-known example with valleys. MX_2 also has valley states at K and $-$K points in the momentum space as in the graphene case. While graphene has massless Dirac fermion with zero band gap at K and $-$K points, MX_2 has massive Dirac fermions with non-zero band gap at K and $-$K points. MX_2 also has SOI induced spin-band splitting at K and $-$K points. In the monolayer limit, due to the broken inversion symmetry, spin is lifted via coupling to valley states. Such spin-valley locking can be useful for spintronics/valleytronics device applications.

Bulk MX_2 has an indirect band gap. In comparison to monolayer, bulk materials have inversion symmetry and degenerate SOI induced spin band

splitting at K and $-$K points. Due to the indirect band gap which results in low photoluminescence quantum yield and low possibility for device applications, bulk MX_2 has been less studied than monolayer. However, each layer of bulk MX_2 has lifted spin degeneracy as confirmed by spin resolved ARPES as shown in Figure 1.6[14]. Figure 1.6 (b) and (c) indicate lifted spin degeneracy in surface layer of bulk WSe_2. These results provide direct experimental evidence for not only spin-valley locking but also locking of spin and layer in MX_2.

1.3 Group 7 TMD ReX_2 (X = S, Se)

The rhenium-based group 7 TMD ReX_2 is an unusual compound amongst the layered TMD due to the low symmetry in the crystal structure. In comparison to group 6 TMD, ReX_2 has characteristic in-plane anisotropic feature in optical property as well as electronic structure due to the chain-like Re sublattice in the lattice structure. ReX_2 preserves inversion symmetry independent of the number of layers and has been proposed to have extraordinary decoupling nature between layers. In contrast to group 6 TMD, ReX_2 is expected to have no SOI induced spin band splitting even for odd number of layers. Due to above mentioned properties, ReX_2 is recognized as promising materials for device applications such as field-effect transistor, polarization-sensitive photodetectors and polarization controlled modulators[15, 16].

1.3.1 Crystal and electronic structure

ReX_2 has a very different lattice structure from MX_2. ReX_2 has triclinic crystal structure as shown in Figure 1.7[17]. This can be described via a structural distortion of 1T structure which is found for some group 5 TMD such as VSe_2 and TaS_2. In the undistorted 1T structure, the transition metal atom is located at the center of an octahedron formed by chalcogen atoms. Due to this structural distortion, there exists not only clear out-of-plane buckling

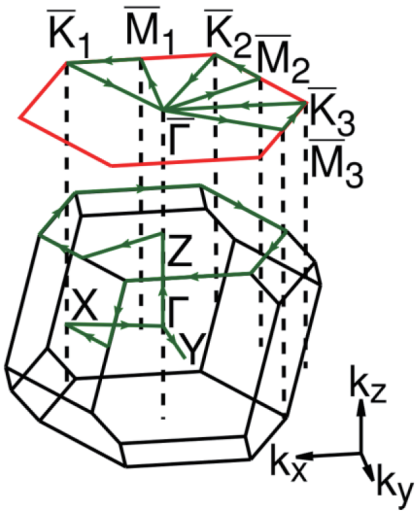

Fig. 1.8: Brillouin zone of triclinic crystal structure ReX_2[18]. Upper side is surface Brillouin zone with high symmetry points and lower is bulk Brillouin zone of ReX_2.

of the chalcogen layers as shown in Figure 1.7 (b) but also zigzag Re chain which is highlighted in Figure 1.7 (a). In addition, the unit cell of ReX_2 is approximately doubled owing to the distortion, and only two-fold symmetry exists.

The electronic band structure of ReX_2 is quite complicate and controversial due to the low crystal symmetry. While the surface Brillouin zone remains almost hexagonal as shown in Figure 1.8[18], the constant energy contour of ReX_2 shows stripelike shape due to the Re chain structure. Unlike group 6 TMD materials, it was suggested that ReX_2 has no indirect-to-direct band gap transition as reducing the number of layers. This indicates that the difference between monolayer and bulk structure is not important for device application[19]. However, there are several indications that there is a band gap transition in ReS_2. The issue could not be resolved as the exact band structure of ReX_2 is controversial. I will discuss detailed information on the controversies in the electronic band structure of ReX_2 in chapter 5.

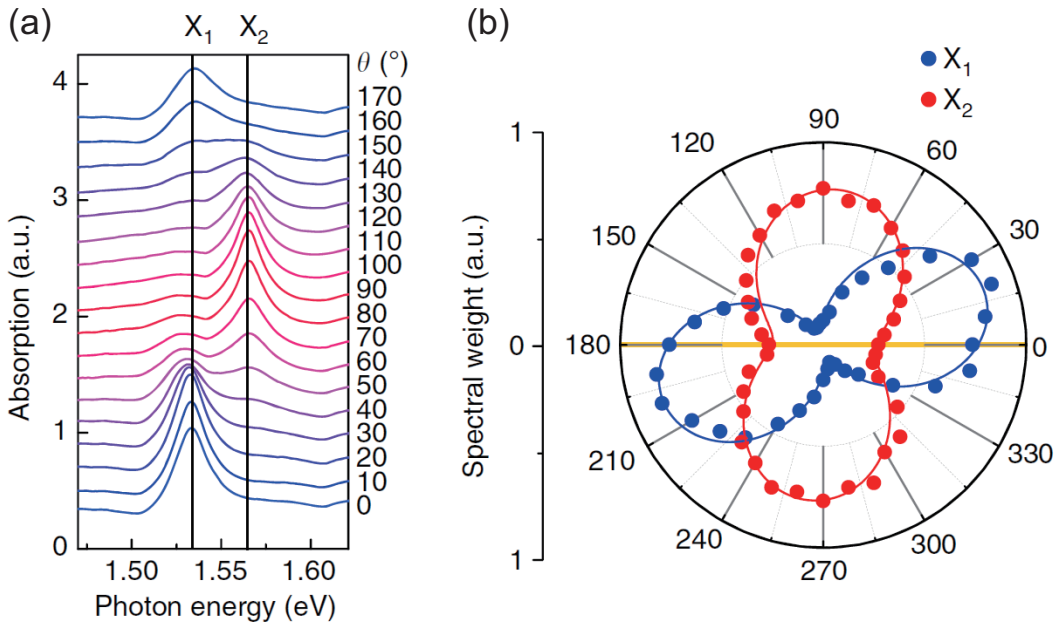

Fig. 1.9: (a) Polarization dependent absorption spectra of few layer ReS_2[20]. (b) Polar plot of angle dependent spectral weight of absorption peaks of each exciton states labelled from (a).

1.3.2 Optical property

The anisotropic nature of ReX_2 shows up not only in the electronic band structure but also in the optical properties measured by Raman spectroscopy and other optical spectroscopic techniques. In monolayer group 6 TMD MX_2, circularly polarized light can manipulate excitons of each valley. For example, right circularly polarized light can excite electrons at the K point and left circularly polarized light can excite electrons at the $-$K point. In contrast to group 6 TMD, excitons of ReX_2 can be manipulated using linear polarizations. There are two low energy exciton peaks around 1.5 eV in optical spectra from ReX_2. We can detect both exciton modes with unpolarized radiation, or one of them with particular polarization. Due to this anisotropy, ReX_2 has been studied for polarization dependent photodetectors.

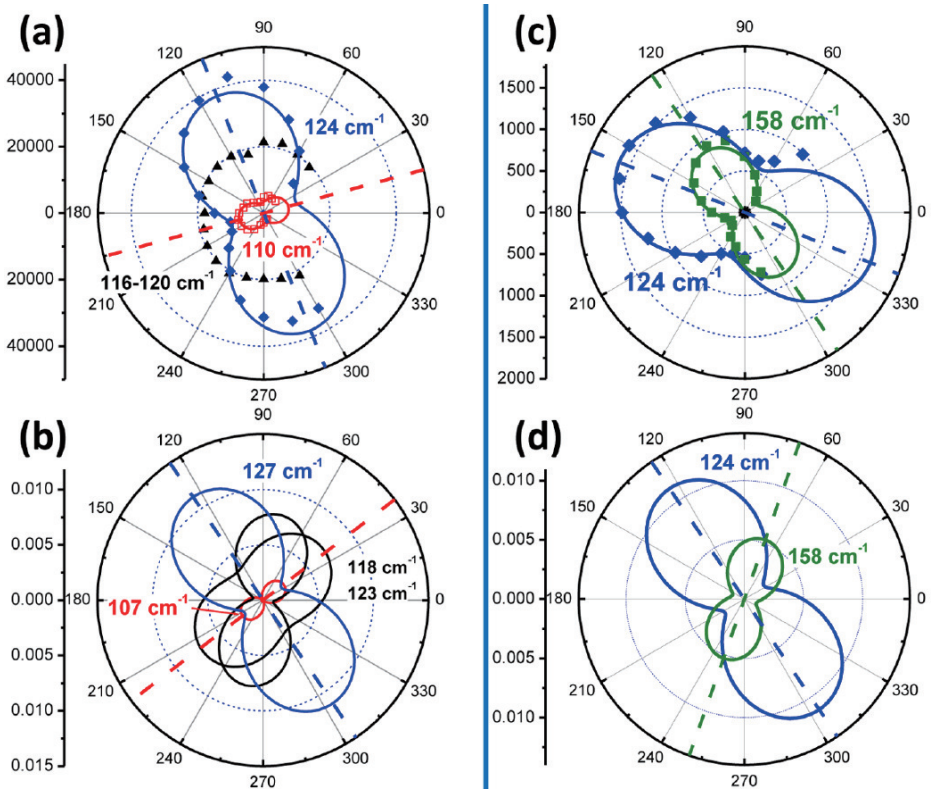

Fig. 1.10: Multiple Raman modes of $ReSe_2$[21]. (a) and (c) show the Raman intensity polar plots from experimental results for Raman modes. (b) and (d) indicate polar plots of Raman intensity based on theoretical results using density functional perturbation theory.

Figure 1.9 shows polarization dependent optical spectra of monolayer ReS_2 using absorption spectroscopy[20]. There are two exciton peaks, so-called X_1 and X_2 which are selectively shown in Figure 1.9 (a). These absorption peaks that arise from the two lowest energy states are direct exciton states near the Γ point. Figure 1.9 (b) is a polar plot of the spectral weights of Lorentzians corresponding to X_1 and X_2. This spectral weight plot also shows anisotropic feature.

Not only the absorption spectra but also Raman modes of ReX_2 show very strong anisotropy in the intensity. In contrast to group 6 TMD which have

only four Raman active modes due to the low in-plane symmetry of ReX_2, there are 18 first-order Raman active modes in ReX_2. Figure 1.10 shows polar plots of intensities of multiple Raman modes in $ReSe_2$ which show highly anisotropic characteristics[21]. In the Raman results, ReX_2 has no low frequency rigid-layer vibrational modes due to the rather weak interlayer interaction[22].

1.4 Thesis highlights

In the following chapters, I will briefly describe the main my experimental technique and show the results of my work based on electronic band structure of semiconducting TMD, MX_2 and ReX_2. After that I will summarize my work during Ph. D course.

In Chapter 2, I will introduce ARPES which is the most powerful tool to study electronic band structures of solids. In performing ARPES measurements, there is a significant technique to modify the surface of the sample so-called $in\text{-}situ$ alkali metal dosing (evaporation) method. I will also briefly explain this technique.

In Chapter 3, I experimentally determine the band parameters of indirect band gap semiconductor bulk MX_2 using ARPES and $in\text{-}situ$ alkali metal dosing. There are many studies on monolayers. But there is almost no research on the band parameters for bulk materials. Several physical properties such as band gap and conduction band minimum position of layered TMD materials are strongly affected by the number of layers. For this reason, I study the band parameters of bulk MX_2 using ARPES for experimental data and tight-binding model calculations as a theoretical approach.

In Chapter 4, after determining the band parameters of bulk MX_2, I demonstrate electric field effect on the surface of bulk $MoSe_2$. The reason why I choose bulk $MoSe_2$ will be elaborated in chapter 4. The orbital character of each high symmetry points (Γ and K) are very different. Γ point has out-of-

plane orbital characters while K point has in-plane orbital characters. Due to this difference in orbital character of two points, when external field is applied along the direction perpendicular to the crystallographic in-plane, the electronic structures evolve differently. This phenomenon is explained within the electrical Stark effect.

In Chapter 5, I investigate about the anisotropic electronic structure of group 7 TMD ReX_2 with triclinic lattice structure. First of all, I will show the constant energy maps of both systems to elucidate the effect of rhenium chain in the crystal. There are several issues on these materials such as the exact location of the valence band maximum. Due to the possibility of changing dimensionality, TMD materials have been studied for promising and potential device applications. For the device applications, it is important to determine the effective mass of carriers in such anisotropic materials. Here, I systematically and quantitatively analyze the electronic band structure using quadratic fitting and extract the angle dependent effective mass of hole carriers.

In Chapter 6, we demonstrate the relation between k_z dispersion relationship and exciton binding energy of ReX_2. I will explain the concept of exciton and exciton binding energy. In order to measure the exciton binding energy, I will introduce two more experimental tools, scanning tunneling spectroscopy (STS) and ellipsometry. We measure the electronic band gap using STS and the optical band gap using ellipsometry. By subtracting the optical band gap from the electronic band gap, we can extract the exciton binding energy of ReX_2.

In Chapter 7, I will summarize my work during Ph. D course, elaborated from chapter 3 to chapter 6.

2 Experimental methods

The main experimental tool to investigate the electronic band structure of single crystal in my Ph. D course is ARPES. In the ARPES experiments, I have used various photon energies from 50 eV to 110 eV of light to get the information about k_z ($k_\perp$) direction band dispersion relationship. In this chapter, I will briefly describe ARPES including photon energy dependent method and $in\text{-}situ$ alkali metal dosing method. I will discuss how the photon energy and surface alkali metal affect the ARPES result.

2.1 Angle-resolved photoemission spectroscopy (ARPES)

Angle resolve photoemission spectroscopy (ARPES) is one of most powerful experimental tools to investigate the distribution of the electrons in the reciprocal/momentum space (k-space) of solid single crystals[23]. Photoelectron spectroscopy is based on the photoelectric effect originally observed by Hertz and was later explained as a manifestation of the quantum nature of light by Einstein[24, 25]. When mono-energy/monochromatic light is incident on a single crystal system by discharge lamp or a synchrotron, an electron can absorb a photon and escape from the material into the vacuum in all directions with a maximum kinetic energy $E_{ph} - \phi$ (where E_{ph} is photon energy of incident light and ϕ is the material work function).

An electron, bound in a solid single crystals with biding energy E_B (the relative energy from the Fermi energy, E_F), has a kinetic energy of $E_{kin} = E_{ph} - \phi - E_B$. By collecting the photoelectrons with an electron energy

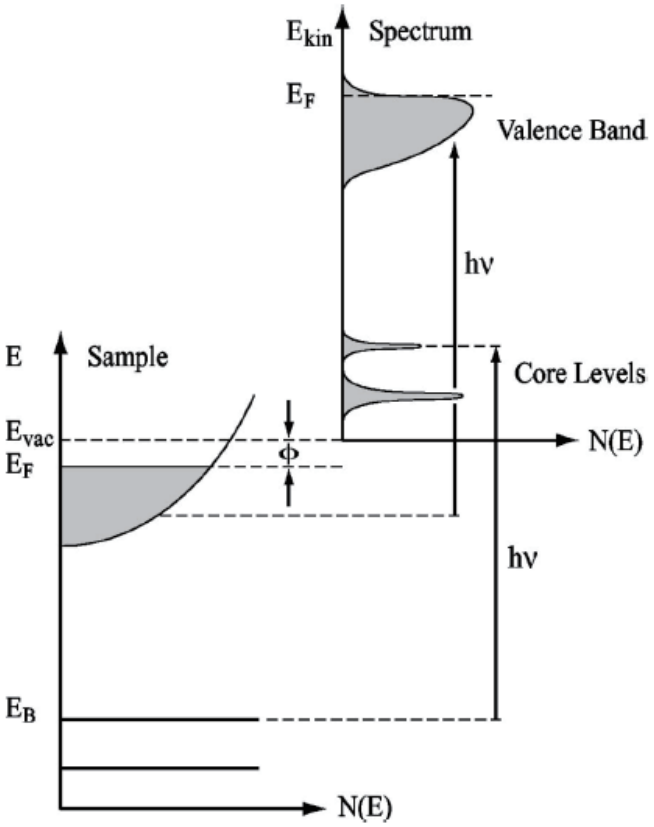

Fig. 2.1: Energetics of the photoemission process. The kinetic energy distribution of photoelectrons produced by incident photon can be translated into the electronic density of state as a function of the binding energy[26].

analyzer characterized by a finite acceptance angle one can directly measure the kinetic energy of the photoelectron for a given emission angle. Therefore, we can deduce the binding energy of electrons in the single crystal from the energy conservation relation. In this way, we can get the information about relative density of states (DOS) from the intensity of the photoelectron at a specific kinetic energy, as described in Fig 2.1.

In addition, one can obtain the momentum information of electrons in solids by measuring the kinetic energy and the emission angle of the photo-

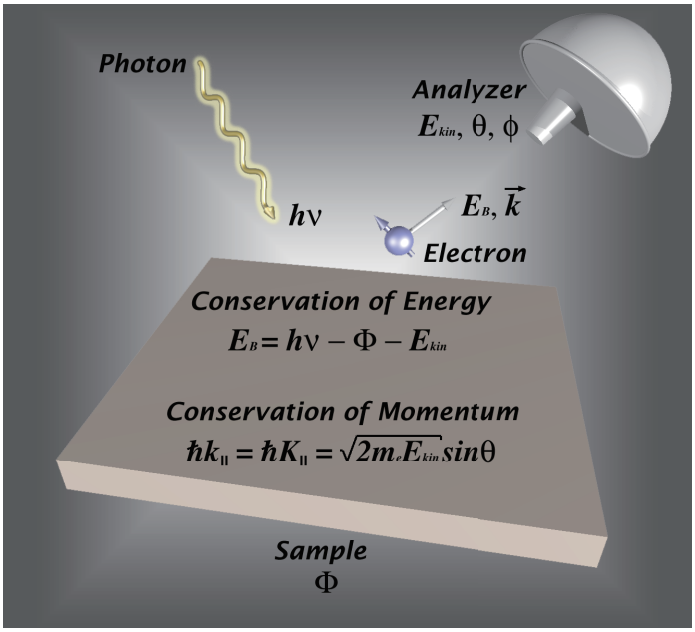

Fig. 2.2: Schematic figure of a photoemission process. Energy and momentum conservation formulae shown in figure are used to reconstruct the spectrum[27].

electron. The emission angle of the photoelectron can be translated into the electron momentum in initial state by energy and momentum conservation laws (Here, the momentum of photon is negligible.),

$$E_{kin} = E_{ph} - \phi - E_B \tag{2.1}$$

$$p_{\parallel} = \hbar k_{\parallel} = \sqrt{2mE_{kin}} sin\theta \tag{2.2}$$

where $p_{\parallel}$ is the in-plane component of the electron crystal momentum in the extended zone scheme and angle θ is defined as the angle between electron emission direction and surface normal direction (Fig. 2.2). Upon going to larger θ angles, one can probe electrons with k lying in higher-order Brillouin zones. The translational symmetry requires that the component of electron momentum in the plane of sample is conserved.

Unfortunately, out-of-plane component of momentum $p_{\perp}$ is not conserved

due to the lack of translational symmetry across the surface. Therefore, a different approach is required to determine the value of $p_\perp$. In fact, several experimental methods for three dimensional band dispersion have been developed, which are rather complex and require additional and complementary experimental data. The typical way of dealing with this is to assume that the final state is a free-electron-like state.

$$E_f(k) = \frac{\hbar^2 k^2}{2m} - |E_0| = \frac{\hbar^2(k_\parallel^2 + k_\perp^2)}{2m} - |E_0| \tag{2.3}$$

Because $E_f = E_{kin} + \phi$ and $\frac{\hbar^2 k_\parallel^2}{2m} = E_{kin} sin^2\theta$, one obtains,

$$k_\perp = \frac{1}{\hbar}\sqrt{2m(E_{kin} cos^2\theta + V_0} \tag{2.4}$$

where the inner potential $V_0 = E_0 + \phi$ corresponds to an energy of valence band bottom from vacuum. By using photon energy dependence experiment, we can estimate the inner potential of solid. Therefore, we can obtain the relationship between out-of-plane momentum and binding energy of solids.

The electronic dispersion in monolayer/2D materials, there is no $k_\perp$ dispersion. In contrast, in bulk/3D systems the $k_\perp$ band structure is quite dispersive. The stronger interlayer hopping (more 3D-like) in bulk materials correspond to the more dispersive band structure in $k_\perp$ direction. In this manner, we can determine whether the system is 2D-like or 3D-like using photon energy dependent ARPES techniques.

Before moving on to the next section, it is worth pointing out that most ARPES experiments are performed at photon energies below 110 eV. There are two reasons. First, in lower photon energies, it is possible to achieve higher momentum and energy resolution. Second, in higher photon energies, we cannot neglect the momentum of photon. If the photon momentum is not negligible, the photoemission process should take into account the

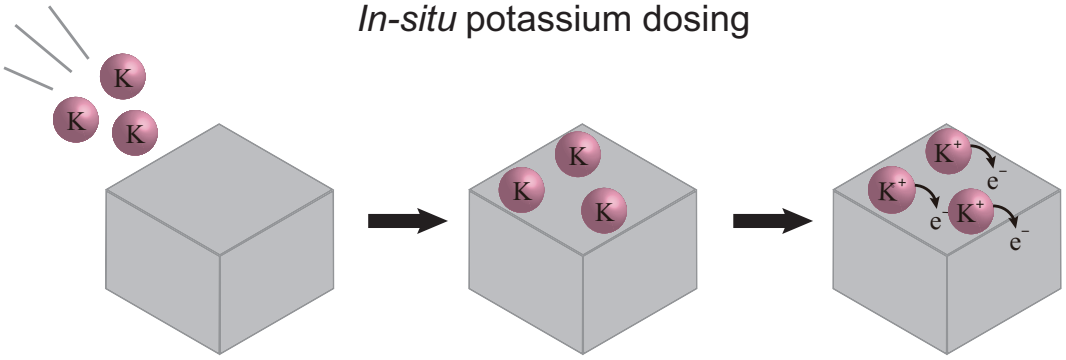

Fig. 2.3: Schematic figure for $in\text{-}situ$ alkali metal (K) dosing and its electron doping effect. Gray box indicates the solid single crystal.

photon momentum.

2.2 $In\text{-}situ$ alkali metal dosing

$In\text{-}situ$ alkali metal dosing (evaporation) on the surface of a material is a widely used method in surface related research field. Because alkali metals including potassium (K), rubidium (Rb), sodium (Na), and cesium (Cs) are willing to donate electrons from themselves to adjacent materials (Fig 2.3), this method is usually used to dope electrons to certain surface states when one performs surface sensitive studies.

Not only electron doping effect, but also there exist electric field effect due to the surface alkali metal. After electron is doped from alkali metal to surface of the solids, there still exist alkali metal on top of the surface of the solid single crystals. Due to the electron doping, the charge of alkali metal is $1+$, not neutral. Due to this non-neutral charge alkali metal layer, there exist surface electric field in downward direction which is illustrated in Figure 2.4. I used surface sensitive $in\text{-}situ$ alkali metal dosing ARPES method with K and Rb during my Ph. D course which precisely discussed in chapter 3 and 4. I will discuss some examples and results of alkali metal dosing method

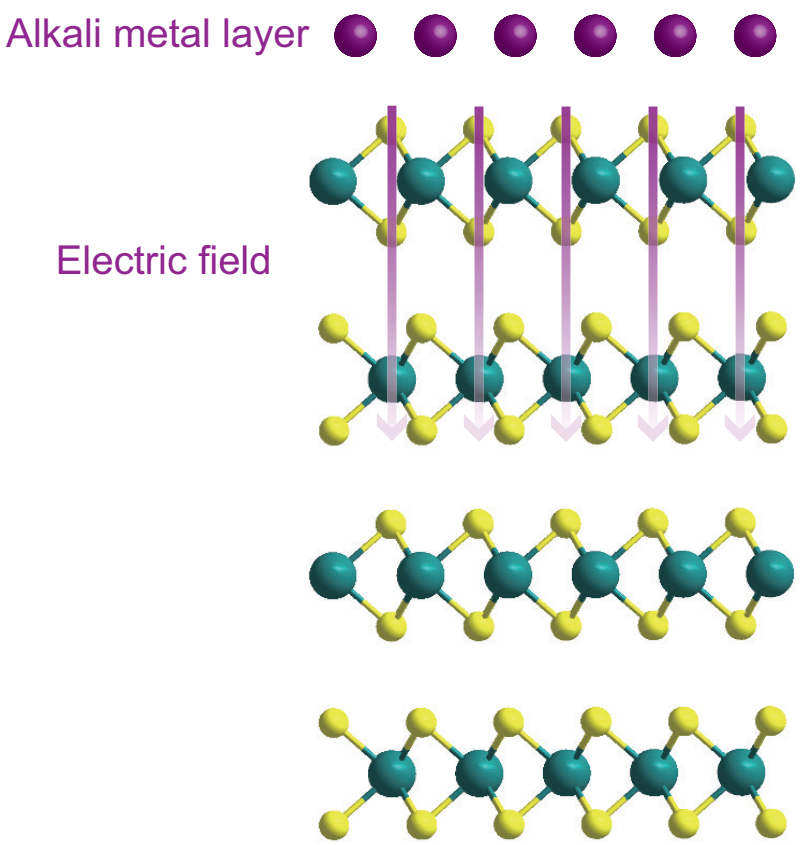

Fig. 2.4: Schematic figure for surface alkali metal induced surface electric field. Purple circles on top of the sample indicate alkali metal layer and arrows indicate surface electric field due to the alkali metal layer.

including appearance of conduction band minimum, electrical Stark effect due to surface electric field, and enhanced superconducting temperature in iron-based superconductors.

Fig 2.5 illustrates one example of alkali metal dosing methods. Rb alkali metal is used for electron doping and surface electric field. There are two effects from alkali metal dosing. One is electron doping from Rb, another is surface electric field from Rb surface layer. Due to electron doping we can access the conduction band minimum which originated from the unoccupied states and due to strong surface electric field, there exist electrical Stark

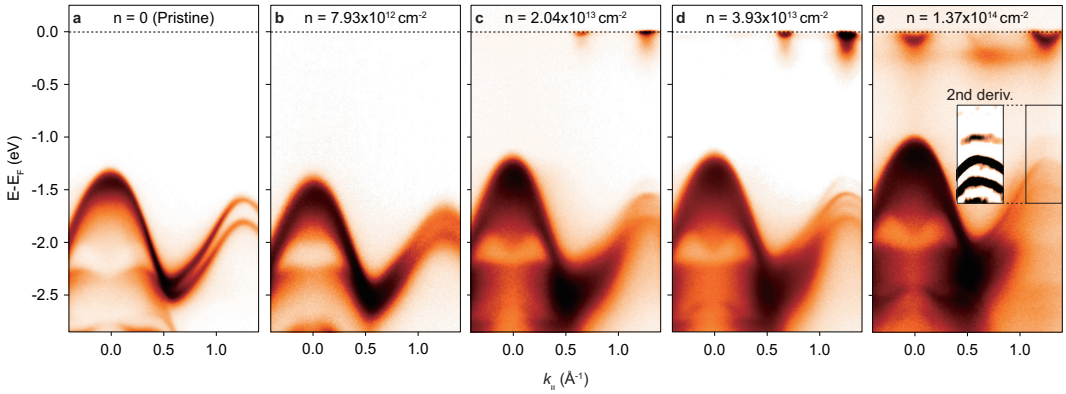

Fig. 2.5: One example for ARPES experiments with $in\text{-}situ$ alkali metal dosing method[29]. Sample is bulk $MoSe_2$ and alkali metal is rubidium. n indicates electron density by electron doping from Rb.

effect which induced reduction of the band gap size. As increasing electron density, the band gap size is reduced and conduction band minimum appears. Detailed information about these two effects on bulk $MoSe_2$ will be discussed in chapter 4.

Another example is illustrated in Figure 2.6. There are two iron-based superconductors. One is iron chalcogenides superconductor FeSe and the other is iron pnictides superconductor $Ba(Fe_{1.94}Co_{0.06})_2As_2$. For FeSe case, alkali metal is Na and for $Ba(Fe_{1.94}Co_{0.06})_2As_2$ case, alkali metal is K. Regardless of alkali metal source, both materials have enhanced superconducting transition temperature. From 8 K to 20 K for FeSe case and from 24 K to 41.5 K for $Ba(Fe_{1.94}Co_{0.06})_2As_2$ case. In superconductor, electron-phonon or electron-electron interaction is important parameter for superconducting transition temperature. Here, excess electrons from alkali metal play a important role to enhance superconducting transition temperature.

From the above examples, combination of $in\text{-}situ$ alkali metal dosing method with ARPES is a powerful tool to investigate surface states of materials or control some parameters such as band gap size or superconducting transition temperature[32, 33, 34]. Control of dosing rate, however, is quite dif-

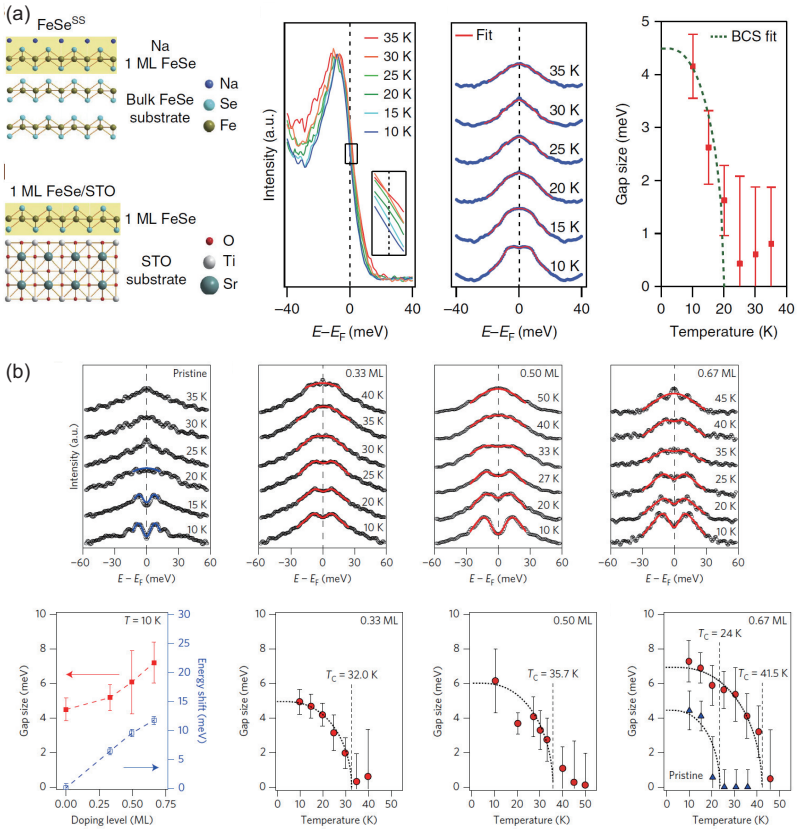

Fig. 2.6: Other examples of *in-situ* alkali metal dosing ARPES[30, 31]. Both cases are related to enhanced superconducting transition temperature of (a) FeSe and (b) $Ba(Fe_{1.94}Co_{0.06})_2As_2$.

ficult and excess atoms causes degradation effect on surface states. Thus, it requires a careful and thorough preparation.

3 Determination of the band parameters of bulk MX_2

In this chapter, I will precisely elaborate low-energy band model for group 6 TMD so called massive Dirac fermion model. This model comes from the graphene based massless Dirac fermion model. Starting from the massless Dirac fermion model, I will explain the massive Dirac fermion model for two cases (with and without SOI). In results section, I show the theoretical results about k_z dispersion relationship of Γ and K point of the Brillouin zone using tight binding model calculations. I also experimentally demonstrate the band parameters of massive Dirac fermion model for MoS_2, $MoSe_2$, WS_2, and WSe_2 using ARPES.

3.1 Introduction

3.1.1 Massive Dirac fermion model

Graphene has massless Dirac fermion and linear dispersion at K and $-$K point of the Brillouin zone. Due to its unusual band structure, the low energy quasiparticles within each valley can be described by the Dirac hamiltonian given by

$$\hat{H} = \hbar v_F \begin{pmatrix} 0 & k_x - ik_y \\ k_x + ik_y & 0 \end{pmatrix} = \hbar v_F \vec{\sigma} \cdot \vec{k}$$

where $\vec{k}$ is the momentum of massless electron, $\vec{\sigma}$ the 2D Pauli matrix and v_F indicates k-independent Fermi velocity[35]. Here, Fermi velocity v_F plays the role of the speed of light. This is the case of graphene where the inversion symmetry is protected.

On the other hand, monolayer TMD MX_2 has massive Dirac fermion due to the presence of inversion symmetry breaking. The low energy electronic properties of monolayer MX_2 are found to be explained within a minimal model, so called massive Dirac fermion model which is slightly modified from the massless Dirac fermion model of graphene. Equation 3.1 and 3.2 show the hamiltonian of massive Dirac fermion model without and with SOI, respectively[36].

$$\hat{H} = at(\tau k_x \vec{\sigma}_x + k_y \vec{\sigma}_y) + \frac{\Delta}{2}\vec{\sigma}_z \tag{3.1}$$

$$\hat{H} = at(\tau k_x \vec{\sigma}_x + k_y \vec{\sigma}_y) + \frac{\Delta}{2}\vec{\sigma}_z - \lambda\tau\frac{\vec{\sigma}_z - 1}{2}\vec{s}_z \tag{3.2}$$

Here, a is the lattice constant, t the effective hopping parameter, τ the valley index (+1 for K valley and -1 for $-$K valley), $\vec{\sigma}$ the Pauli matrices for the basis functions, Δ the direct band gap size without SOI at K and $-$K points, 2λ the SOI induced spin band splitting size, and $\vec{s}_z$ the Puali matrix for spin. In massive Dirac fermion model, there are only three independent parameters: the effective hopping (t), band gap without SOI (Δ), and SOI induced spin band splitting (2λ). There are several reports for these free parameters of monolayer MX_2. For example, the extracted values of Δ and 2λ are 1.465 and 0.15 eV for the monolayer MoS_2 on Au(111) using molecular beam expitaxy, and 1.67 and 0.18 for monolayer $MoSe_2$ grown on bilayer graphene[5, 37]. 2λ value for monolayer WS_2 on Au(111) is found to be

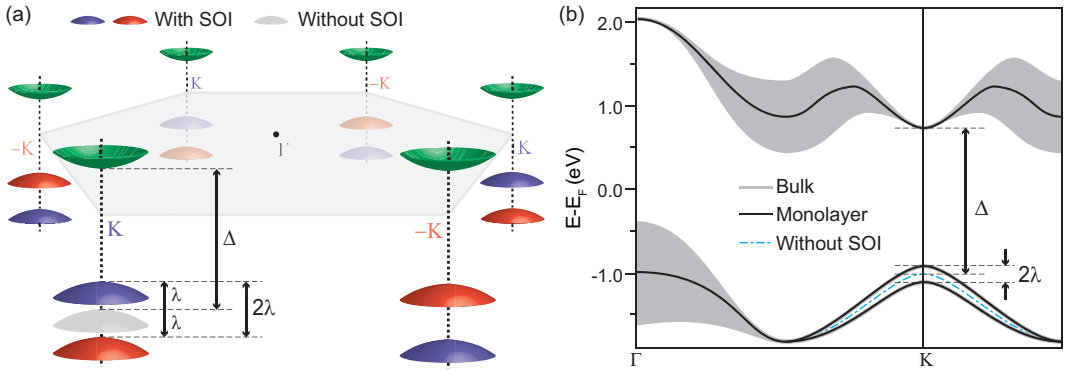

Fig. 3.1: (a) Schematic sketch of the massive Dirac fermion model[39]. Gray valence band at the front-left K point is for the case without SOI while red/blue valence bands correspond to the spin up/down states for including SOI. (b) Electronic structure of bulk projected monolayer MX_2.

0.42 eV[38]. These results indicate that free parameters of massive Dirac fermion model for monolayer MX_2 can be influenced by extrinsic factors such as the substrate and the carrier concentration of the system.

Figure 3.1 (a) shows the schematic sketch of the massive Dirac fermion model[39]. Two cases are included in the figure, one without SOI and the other with SOI. Note that while inversion symmetry is restored in the bulk and thus the valley physics is removed, three parameters are remain and still validate in the dispersion at the K point as shown in Figure 3.1 (b). In this sense, we try to show the electronic band dispersion near the K point and determine the three independent parameters of bulk MX_2.

3.2 Result and discussion

3.2.1 Tight binding calculations for electronic structure evolution from monolayer to bulk MX_2

A natural question is how the electronic band structure at K and Γ points from monolayer to bulk MX_2 evolves as the number of layers. In order to answer this, we performed tight binding calculations of electronic structure evolution at in-plane K and Γ points from monolayer to bulk MX_2. Our calculations based on tight binding model of MX_2 indicate that the electronic band dispersion along the k_z direction at the in-plane K point is almost zero, whereas band dispersion along k_z direction at Γ point has dispersive enough to induce indirect to direct band gap transition. This results show that we can still describe the band parameters of bulk MX_2 at K point using the massive Dirac fermion model. Here, we only use the dispersion of the massive Dirac fermion model for the bulk MX_2. Spin states at K point are degenerate in bulk MX_2.

First, we consider the k_z dispersion of the valence band at the in-plane Γ point. The conduction band is not considered here since it is not easy to find an effective tight binding model due to the multiple mixing orbital characters with other bands. On the other hand, orbital characters of the valence band are well separated from other bands and the mixing could be negligible. As mentioned above, we also neglect the spin degree of freedom at the valence bands which does not affect the band broadening at both K and Γ points. At Γ point, the orbital composition of the valence band is given by

$$|\psi_{\Gamma_{VB}}\rangle = \tilde{c}_1|d_0^{(e)}\rangle - c_1|p_0^{(e)}\rangle \tag{3.3}$$

where $|d_0^{(e)}\rangle = |d_{z^2}\rangle$ and $|p_0^{(e)}\rangle = (|p_z^A\rangle - |p_z^B\rangle)/\sqrt{2}$. Here, A and B represent the chalcogen atoms at the upper and lower side of the MX_2 slab. From now

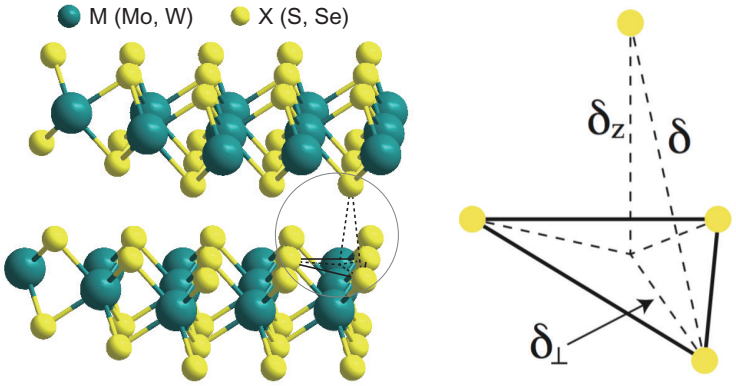

Fig. 3.2: Crystal structure of MX$_2$. The right figure indicates zoom-in of the circle of left figure. It shows the definitions of the parameters used in calculation.

on, I will remove the superscript (e) of the p_z orbital. $\tilde{c}_1 = \sqrt{1-c_1^2}$ and its value for various TMDs has been obtained by Fang *et. al.*[40].

The Bloch wave function with the translational symmetry along z-axis is given by

$$|\Psi^{l(u)}_{\Gamma_{VB},k_z}\rangle = \frac{1}{\sqrt{N}}\sum_n |\psi^{n,l(u)}_{\Gamma_{VB}}\rangle e^{ink_zc} \tag{3.4}$$

where n is layer index, and I and u represent the lower and upper MX$_2$ slab in the unit cell. c is the lattice constant along z direction and we set the gauge so that there is no k_z dependence in the same unit cell. Here, $|\psi^{n,l(u)}_{\Gamma_{VB}}\rangle$ is a function of k_x and k_y and is constructed to satisfy the Bloch condition in the xy-plane.

If we assume that $\epsilon_{\Gamma_{VB}}$ is the energy at Γ point of the valence band of monolayer MX$_2$, the effective Hamiltonian of the 3D bulk system at this point is given by

$$H_\Gamma \approx \begin{pmatrix} \epsilon_{\Gamma_{VB}} & \Delta_{\Gamma,k_z} \\ \Delta^*_{\Gamma,k_z} & \epsilon_{\Gamma_{VB}} \end{pmatrix}$$

where $\Delta_{\Gamma,k_z} = \langle \Psi^t_{\Gamma_{VB},k_z} | H' | \Psi^b_{\Gamma_{VB},k_z} \rangle$. Here, H' indicates interlayer hopping terms which will be explained in the followings. Its eigenvalues are evaluated to be

$$E^{\pm}_{\Gamma_{VB}} = \epsilon_{\Gamma_{VB}} \pm |\Delta_{\Gamma,k_z}| \tag{3.5}$$

The off-diagonal component Δ_{Γ,k_z}, which is dependent on k_z, corresponds to the band broadening and can be calculated as follows.

$$\begin{aligned} \Delta_{\Gamma,k_z} \approx & -\frac{c_1^2}{2} \sum_i \langle p_z^{B,n,u} | H' | p_z^{A,n,l}(\delta_i) \rangle \\ & - \frac{c_1^2}{2} \sum_i \langle p_z^{A,n,u} | H' | p_z^{B,n+1,l}(\tilde{\delta}_i) \rangle e^{ik_z c} \end{aligned} \tag{3.6}$$

where δ_i is vectors representing the nearest neighboring sites between MX_2 layers and $\tilde{\delta}_i = -\delta_i$. Note that the nearest neighboring vectors between slabs in the same unit cell are in opposite directions to those in different unit cells due to the way of the stacking[41]. There are no phase factors depending on k_x and k_y in the above since we are considering only the Γ point.

Now, we use the following Slater-Koster approximation.

$$\begin{aligned} t^{(LL)}_{p'_i,p_j} &= \langle p'_i(\mathbf{r}_i) | H' | p_j(\mathbf{r}_j) \rangle \\ &= (V_{pp\sigma} - V_{pp\pi}) \frac{r_i r_j}{r^2} + V_{pp\pi} \delta_{ij} \end{aligned} \tag{3.7}$$

where $V_{pp\sigma(\pi)}$ is exponentially decaying function of the distance between p orbitals[40].

For the case of Δ_{Γ,k_z}, only p_z orbital is involved so that $r_i r_j / r^2 = (\delta_z/\delta)^2$.

As a result, we have

$$\begin{aligned}\Delta_{\Gamma,k_z} &= -\frac{c_1^2}{2}\sum_i \langle p_z^{B,n,t}|H'|p_z^{A,n,b}(\delta_i)\rangle \left(1+e^{ik_z c}\right) \\ &= -\frac{D_\Gamma}{2}\left(1+e^{ik_z c}\right)\end{aligned} \tag{3.8}$$

where

$$D_\Gamma = 3c_1^2\left\{(V_{pp\sigma}-V_{pp\pi})\left(\frac{\delta_z}{\delta}\right)^2 + V_{pp\pi}\right\}. \tag{3.9}$$

Then, the energy spectra at Γ point becomes

$$E^{\pm}_{\Gamma_{VB}} = \epsilon_{\Gamma_{VB}} \pm D_\Gamma(1+\cos k_z c) \tag{3.10}$$

whose bandwidth is maximized at $k_z = 0$ and vanishing at the zone boundary. If one measure the bandwidth at Γ point along z direction by the experiment, we can extract the relation between two fundamental interlayer hopping parameters $V_{pp\sigma}$ and $V_{pp\pi}$ from the above. For example, for the case of MoS_2, we obtain $V_{pp\sigma} = 0.6344$ and $V_{pp\pi} = -0.0592$ in eV, assuming $\delta = 3.4261$ (S-S distance) and $\delta_z = 2.9$[40, 42]. As a result, we estimate $D_\Gamma = 0.4284$ eV so that the bandwidth at Γ point is about 1.7 eV which is comparable to the experimental results. Those parameters are from a simple model for the overlap integral and can be tuned a little in the realistic system.

Now, we consider the states at K point on the valence and conduction band. At this point, the orbital composition is completely different from that at Γ point. They have equal portion of p_x and p_y orbital components while p_z orbital contribution is vanishing. Their orbital constituents are given by

$$|\psi_{K_{VB}}\rangle = \tilde{c}_6|d_2^{(e)}\rangle + c_6|p_1^{(e)}\rangle \tag{3.11}$$

and

$$|\psi_{K_{CB}}\rangle = \tilde{c}_5|d_0^{(e)}\rangle + c_5|p_{-1}^{(e)}\rangle \tag{3.12}$$

where $|d_0^{(e)}\rangle = |d_{z^2}\rangle$, $|d_2^{(e)}\rangle = (|d_{x^2-y^2}^{(e)}\rangle + i|d_{xy}^{(e)}\rangle)/\sqrt{2}$ and $|p_{\pm1}^{(e)}\rangle = (|p_x^A\rangle + |p_x^B\rangle) \pm i(|p_y^A\rangle + |p_y^B\rangle)$. Here, $\tilde{c}_n = \sqrt{1-c_n^2}$.

In this case, we consider following effective 4×4 Hamiltonian for the conduction and valence bands of the 3D bulk system.

$$H_K \approx \begin{pmatrix} \epsilon_{K_{VB}} & 0 & \Delta_{K_{VB},k_z} & \alpha_{K,k_z} \\ 0 & \epsilon_{K_{CB}} & \beta_{K,k_z} & \Delta_{K_{CB},k_z} \\ \Delta^*_{K_{VB},k_z} & \beta^*_{K,k_z} & \epsilon_{K_{VB}} & 0 \\ \alpha^*_{K,k_z} & \Delta^*_{K_{CB},k_z} & 0 & \epsilon_{K_{CB}} \end{pmatrix}$$

where Δ_{K_{VB},k_z} and Δ_{K_{CB},k_z} are mixings between same orbitals and α_{K,k_z} and β_{K,k_z} are between different ones. The upper(lower) 2×2 diagonal block is for the top(bottom) slab.

As in the previous case, one can evaluate Δ_{K_{VB},k_z} approximately as follows. Removing negligible terms involving d orbitals, we have

$$\Delta_{K_{VB},k_z} = \langle \Psi^t_{K_{VB},k_z} | H' | \Psi^b_{K_{VB},k_z} \rangle \tag{3.13}$$

$$= \frac{c_6^2}{4} \sum_i \left\{ (V_{pp\sigma} - V_{pp\pi}) \frac{\delta^2_{i,\perp}}{\delta^2} + 2V_{pp\pi} \right\} e^{i\vec{K}\cdot\delta_i} \tag{3.14}$$

$$+ \frac{c_6^2}{4} \sum_i \left\{ (V_{pp\sigma} - V_{pp\pi}) \frac{\tilde{\delta}^2_{i,\perp}}{\tilde{\delta}^2} + 2V_{pp\pi} \right\}$$

$$\times e^{i\vec{K}\cdot\tilde{\delta}_i} e^{ik_z c}$$

where $\delta^2_{i,\perp} = \delta^2_{i,x} + \delta^2_{i,y}$ and $\vec{K}$ corresponds to the position vector of K point of the monolayer MX_2. Since the value of $\delta^2_{i,\perp}$ for all the nearest neighboring hopping processe are equal to each other, one can set $\delta^2_\perp = \delta^2_{i,\perp}$ and Δ_{K_{VB},k_z} can be further simplified as

$$\Delta_{K_{VB},k_z} = R_{K_{VB}} \left(f(\vec{K}) + f(\vec{K})^* e^{ik_z c} \right) \tag{3.15}$$

where

$$R_{K_{VB}} = \frac{c_6^2}{4} \left\{ (V_{pp\sigma} - V_{pp\pi}) \frac{\delta^2_\perp}{\delta^2} + 2V_{pp\pi} \right\} \tag{3.16}$$

and

$$f(\vec{k}) = \sum_i e^{i\vec{k}_\perp \cdot \delta_i}. \tag{3.17}$$

As was in the case of the Dirac point of graphene, $f(\vec{K}) = 0$ and we arrive at the conclusion that $\Delta_{K_{VB},k_z} = 0$ at the K point[4]. By the same procedure, one can easily check Δ_{K_{CB},k_z} is also vanishing. As a result, the matrix representation of the effective Hamiltonian reduces to

$$H_K \approx \begin{pmatrix} \epsilon_{K_{VB}} & 0 & 0 & \alpha_{K,k_z} \\ 0 & \epsilon_{K_{CB}} & \beta_{K,k_z} & 0 \\ 0 & \beta^*_{K,k_z} & \epsilon_{K_{VB}} & 0 \\ \alpha^*_{K,k_z} & 0 & 0 & \epsilon_{K_{CB}} \end{pmatrix}$$

Finally, α_{K,k_z} and β_{K,k_z} is calculated as

$$\begin{aligned} \alpha_{K,k_z} &= \langle \Psi^t_{K_{VB},k_z} | H' | \Psi^b_{K_{CB},k_z} \rangle \\ &\approx D_K \end{aligned} \tag{3.18}$$

and

$$\begin{aligned} \beta_{K,k_z} &= \langle \Psi^t_{K_{CB},k_z} | H' | \Psi^b_{K_{VB},k_z} \rangle \\ &\approx D_K e^{ik_z c} \end{aligned} \tag{3.19}$$

where

$$D_K = \frac{3c_5 c_6}{4} \left(\frac{\delta_\perp}{\delta} \right)^2 (V_{pp\sigma} - V_{pp\pi}) \tag{3.20}$$

Note that $\alpha_{K,k_z} \neq \beta^*_{K,k_z}$ due to the layer index. Here, $\delta_{1,\perp} = (a/2, a/2\sqrt{3}, 0)$, $\delta_{2,\perp} = (-a/2, a/2\sqrt{3}, 0)$, and $\delta_{3,\perp} = (0, -a/\sqrt{3}, 0)$. For the case of MoS_2 as an example, we have $D_K \approx 0.0263$ eV from the parameters given by $\delta_\perp = 1.8244$Å, $\delta = 3.4261$Å, $V_{pp\sigma} = 0.6344$ eV, and $V_{pp\pi} = -0.0592$ eV[40, 42].

Now, the effective Hamiltonian at K point reads

$$H_K \approx \begin{pmatrix} \epsilon_{K_{VB}} & 0 & 0 & D_K \\ 0 & \epsilon_{K_{CB}} & D_K e^{ik_c} & 0 \\ 0 & D_K e^{-ik_c} & \epsilon_{K_{VB}} & 0 \\ D_K & 0 & 0 & \epsilon_{K_{CB}} \end{pmatrix}$$

Its eigenvalues are evaluated as

$$E_K^{\pm} = \frac{\epsilon_{VB} + \epsilon_{CB} \pm \sqrt{(\epsilon_{VB} - \epsilon_{CB})^2 + 4D_K^2}}{2} \tag{3.21}$$

which is independent of k_z. Since $|\epsilon_{VB} - \epsilon_{CB}| \gg 2D_K$, as an approximation, we have

$$\epsilon_{K_{VB}} \to \epsilon_{K_{VB}} - \frac{D_K^2}{\epsilon_{CB} - \epsilon_{VB}} \tag{3.22}$$

and

$$\epsilon_{K_{CB}} \to \epsilon_{K_{CB}} + \frac{D_K^2}{\epsilon_{CB} - \epsilon_{VB}}. \tag{3.23}$$

This indicates that the energies of the conduction and valence bands at K point are k_z-independent and just experience the tiny energy shifts as we are going from the monolayer to the bulk. Obtaining the results, two factors were crucial. First, there are no p_z orbital components in the states on both bands at K point. Second, at K point, many sums of the phase factors are vanishing due to the C3 symmetry. One can obtain the same results at $-$K point since the basis wavevectors are just changed to the complex conjugates of the wavevectors at K point.

In summary, we have shown that the induced band dispersions along the k_z

direction, by the stacking of MX_2 slabs, are completely different between two high symmetry points Γ and K. This can be interpreted by the orbital composition and the discrete rotational symmetry of the system at those points. At Γ point, the eigenstate mainly consists of the out-of-plane orbitals such as the d_{z^2} orbital of the M atom and the p_z orbital of the X atom. As a result, the overlap integrals between different layers is expected to be large compared to the in-plane orbitals. Since any kind of phase cancellations related to the nearest neighboring hopping processes are not possible at Γ point ($k_x = k_y = 0$), the energy spectra of the 3D MX_2 become dispersive along the k_z direction at Γ point.

At K point, on the other hand, we have both the out-of-plane (d_{z^2}) and in-plane orbital (p_x and p_y) components in the M and X atoms each. Among them, only the p_x and p_y orbitals are responsible for the interlayer coupling because the distance between M atoms in the neighboring slabs is much larger than that of the nearest neighboring X atoms and the overlap between d_{z^2} orbitals is negligible. At first glance, one can expect the small dispersions along the k_z direction due to the smaller inter-plane hopping between p_x and p_y orbitals compared to the p_z orbitals. However, we have shown that even this small dispersion is suppressed and the band becomes almost dispersionless along the k_z direction at K point due to the graphene-like phase cancellation between the nearest hopping processes by the C3 symmetry of the system.

3.2.2 ARPES measurements on bulk MX_2 systems

I performed ARPES measurements at the beam line 4.0.3.2 (MERLIN) of the Advanced Light Source at the Lawrence Berkeley National Laboratory equipped with a VG-SCIENTA R8000 electron analyzer. Bulk MX_2 single crystal samples were purchased from HQgraphene and all samples cleaved $in\text{-}situ$. All data were taken below 50K in a vacuum chamber better than 5×10^{-11} Torr with linearly polarized light. For the photon energy dependence,

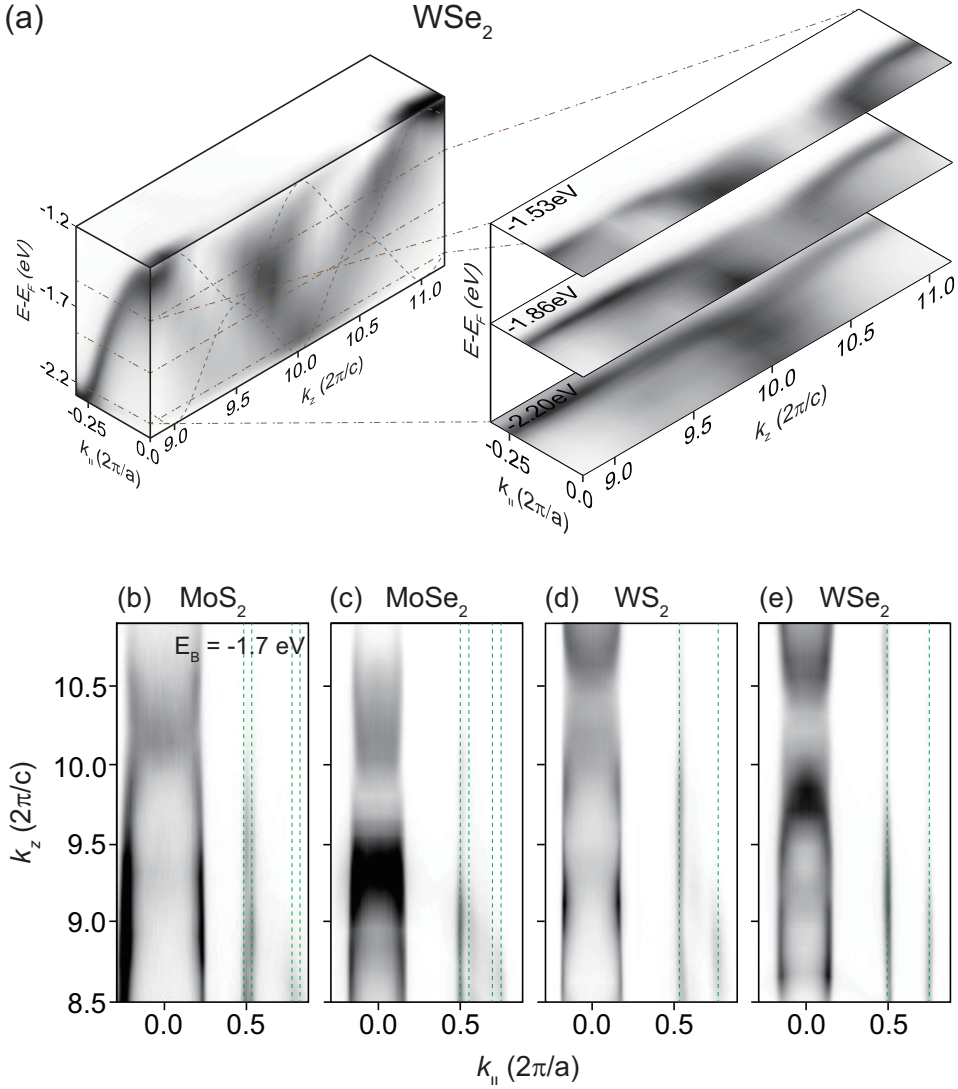

Fig. 3.3: Photon energy dependent ARPES data. (a) ARPES intensity plot in energy and momentum (k_z, $k_{||}$) space. ARPES intensity at different k_z but at same in-plane momentum is taken by different incident-photon energies from 50 to 110 eV. The data at k_z=9.0 and k_z=11.0 at in-plane Γ point were taken at incident-photon energy of 58 and 94 eV, respectively. The black dashed lines indicate calculated k_z dispersion of band with D_Γ=0.5 eV [Eq. 3.10]. Three selected cuts of right hand side along the brown dashed lines are ARPES intensity maps for three different binding energies in momentum space (k_z, $k_{||}$). ARPES intensity mapping of (b) MoS_2, (c) $MoSe_2$, (d) WS_2, (e) WSe_2 at constant binding energy of -1.7 eV. The dashed lines indicate the electronic states near K point, which are completely straight along k_z.

photon energies between 50 and 110 eV with 2 eV energy step were used. The total energy resolution was better than 20 meV with a momentum resolution of 0.04Å^{-1}. In order to determine the position of conduction band minimum, band gap size at K point, and indirect band gap size, we need to perform $in\text{-}situ$ alkali metal evaporation. Alkali metal dispensers from SAES Getters were used for potassium evaporation experiments and evaporation was conducted $in\text{-}situ$ with the samples at the measurement position.

First of all, I performed photon energy dependent ARPES measurement to obtain the information about k_z dispersion relationship of the valence band at Γ and K point of the hexagonal Brillouin zone. Figure 3.3 (a) shows the k_z dispersion relationship of electronic band structure of bulk WSe_2 at in-plane Γ point. Dashed lines indicate band dispersion from tight binding calculations which is shown in Eq. (3.10). The data provide consistent result with the calculation results and show quite strong k_z dispersion. Due to the finite escape depth of the ARPES process which means finite k_z resolution, the ARPES data look quite broad along the energy direction. k_z dispersions in bulk MoS_2, $MoSe_2$, and WS_2 near in-plane Γ point are as strong (dispersive) as that in bulk WSe_2 [Figure 3.3 (b), (c), (d)].

On the other hand, for the K point, photon energy dependent ARPES data show almost no k_z dispersion, consistent with tight binding calculation results of Eq. (3.21) as shown in Figure 3.3 (b) to (e). The dashed lines in Figure 3.3 (b)-(e) are guide-to-eye for the electronic bands near K point, which are straight along the k_z direction. Since the energy of electronic bands at a specific in-plane momentum is same regardless of photon energy, Spectral lineshapes near K point are very sharp in comparison to Γ point data.

In order to determine the exact number of three free parameters of massive Dirac fermion model, I first fix the photon energy at the exact Γ point of the 3D Brillouin zone of each materials. Figure 3.4 indicates the ARPES data cut from in-plane Γ to K point. The SOI induced spin band splitting (2λ) of four systems are clearly observed in Figure 3.4 (a)-(d). As the spin-orbit coupling of transition atom and chalcogen atom increases from Mo to W and from S

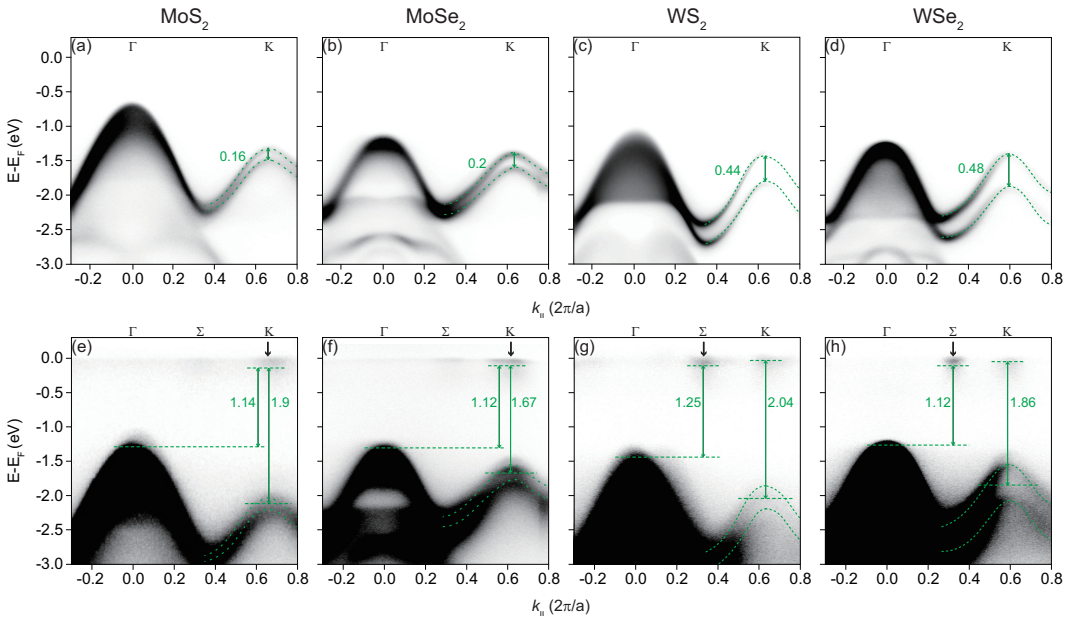

Fig. 3.4: Electronic structure of bulk MX_2 before and after K evaporation. (a)-(d) ARPES spectra along Γ to K point from MoS_2, $MoSe_2$, WS_2, and WSe_2, respectively. (e)-(h) ARPES spectra after potassium evaporation of each materials. The electron doping concentration are 1.7×10^{13}cm^{-2}, 2.5×10^{13}cm^{-2}, 3.5×10^{13}cm^{-2}, and 2.6×10^{13}cm^{-2} for MoS_2, $MoSe_2$, WS_2, and WSe_2, respectively.

to Se, the values of 2λ which entirely relies on the atomic spin-orbit coupling are drastically increased. The effective hopping integral, t, could be also observed from the data of Figure 3.4 (a)-(d) through the fitting process as t is basically linearly proportional to the curvature of valence band dispersion at K point. The extracted t value of MoS_2 is larger than that of $MoSe_2$ as the curvature is larger in MoS_2 than in $MoSe_2$. Also, WS_2 have larger t than WSe_2. Here, I assume that the conduction band dispersion which cannot be measured is mirror-symmetric with the valence band dispersion. This is not an unreasonable assumption considering the band calculation results[41].

In order to observe the direct band gap size at K point (Δ-λ) or the indirect band gap size between valence band maximum at Γ point and conduction band minimum at K or Σ point, it is necessary to see the conduction band,

	n (cm^{-2})	Δ	**2**λ	t	Δ-λ	**ID gap**
Bulk MoS_2	1.7×10^{13}	1.90	0.16	1.01	1.82	1.14
1ML MoS_2 [37]	>0 (ARPES)	1.465	0.15	1.10*	1.39	
1ML MoS_2 [43]	0 (STM)				2.15	
1ML MoS_2 [44]	0 (STM)				2.40	
1ML MoS_2 [44]	0 (STM)					2.10
1ML MoS_2 [44]	0 (STM)					1.75
Bulk $MoSe_2$	2.5×10^{13}	1.67	0.20	0.90	1.57	1.25
1ML $MoSe_2$ [5]	>0 (ARPES)	1.67	0.18	0.90*	1.58	
8ML $MoSe_2$ [45]	0 (STM)					1.41
1ML $MoSe_2$ [45]	0 (STM)				2.18	
Bulk WS_2	3.5×10^{13}	2.04	0.44	1.25	1.82	1.25
1ML WS_2 [38]	3.5×10^{13}		0.42			
Bulk WSe_2	2.6×10^{13}	1.86	0.48	1.13	1.62	1.12
1ML WSe_2 [46]	>0 (ARPES)		0.475		1.40	
1ML WSe_2 [46]	0 (STM)				1.95	

Tab. 3.1: Eletron density (n) and parameters for the massive Dirac fermion model determined from ARPES data. Also given in the table are the summarized values from published reports using ARPES and scanning tunneling spectroscopy (STM). ML indicates monolayer and ID gap indicates indirect band gap between Γ point of valence band and conduction band minimum at K or Σ point. All units of parameters are eV. Note that t values with * mark are obtained by fitting the dispersions of the published results.

where no electrons are occupied and ARPES signal cannot be detected. I use $in\text{-}situ$ potassium dosing technique on the surface of materials to see the conduction band minimum. Here, I mainly use the electron doping effect of alkali metal. Figure 3.4 (e)-(h) indicate the high symmetry cuts along the Γ to K direction after the potassium dosing on four samples. The conduction band minimum is located at K point in bulk MoS_2 and $MoSe_2$, whereas the conduction band minimum is located at Σ point in bulk WS_2 and WSe_2. The conduction band minimum of monolayer MoS_2, $MoSe_2$, WS_2, and WSe_2 is located at K point. Due to the k_z dispersion at Σ point conduction electronic band and strong spin orbit coupling which affects the band structure

of Σ point, in the bulk WS_2 and WSe_2, the conduction band minimum is located at Σ point which is even lower than that at K point. The energy of the conduction band minimum is determined from the onset of the photoemission intensity, as indicated by dashed lines near the Fermi level in Figure 3.4 (e)-(h).

All the parameters of the bulk MX_2 (my work) and the known parameters of other mono- or multi-layer MX_2 systems (published works) are summarized in the Table 3.1. We show in the first column the doped electron density by potassium dosing since doped electron density can affect some of parameters, especially Δ[47]. In the second through fourth columns, the three fundamental parameters of the model are summarized. In the last two columns, other interesting parameters, which are direct band gap at K point ($\Delta - \lambda$) and indirect band gap, are also summarized. Comparing the fundamental parameters of the bulk MX_2 and mono- or multi-layer MX_2, we notice that spin band splitting (2λ) is about 20 meV larger in the bulk MX_2. This is consistent with the results of optical experiments[48]. We also find that the doped electron density does not affect the size of the spin band splitting as shown in Figure 3.4.

On the other hand, the story for Δ is different from that of the spin band splitting size (2λ). Unlike SOI induced spin band splitting, Δ is affected by various factors such as the density of doped electrons. In order to measure Δ or direct band gap size ($\Delta - \lambda$) using ARPES, it is necessary to dope electrons into MX_2 to populate the conduction band minimum. The measured value of $\Delta - \lambda$ by ARPES in such a way is clearly smaller than that measured by STM on pristine/undoped MX_2 even though there is some variation in the reported STM values[43, 44, 45]. The observed trend is attributed to the fact that the doped electrons enhance the screening and thus reduce the size of the direct band gap. Likewise, it is expected that stacked layers or metallic substrates for thin film play a similar role in the screening effect and thus affect the band gap size. The effects on the band gap reduction from stacked layers and bilayer graphene substrate appear to be similar since the

band gaps for bulk $MoSe_2$ and 1ML $MoSe_2$ on bilayer graphene measured by ARPES are almost the same. On the other hand, the effect from Au substrate must be much larger, considering the fact that 1ML MoS_2 on Au(111) has significantly reduced band gap compared to the bulk MoS_2. However, we note that quantitative estimation of the band gap reduction from stacking or metallic substrates is not possible without the band gap size of a free-standing MX_2 monolayer.

3.3 Conclusion

In the theoretical part, we found that the band dispersion along the k_z direction at the in-plane K and $-$K points vanishes in bulk 2H-MX_2 due to the graphene-like phase cancellation. Therefore, the electronic band dispersions near the in-plane K and $-$K points in bulk MX_2 are well described by the massive Dirac fermion model. In the experimental part, we confirmed the vanishing k_z dispersion at the in-plane K and $-$K points in bulk MX_2. All the fundamental band parameters could be extracted for bulk MX_2. Most importantly, the direct band gap at the K point ($\Delta - \lambda$) shows significant variation depending on the doped electron density, the number of stacking layers and the substrates. The variation of the direct band gap size can be attributed to reduction of the direct band gap due to the enhanced screening. Our work provides useful information on the electronic band structure of bulk and their relation between the monolayer and multi-layer MX_2. It suggests a way to manipulate the band gap of MX_2.

4 Possible electric field induced indirect to direct band gap transition in bulk $MoSe_2$

In this chapter, I will introduce the Stark effect and screening effect which are deeply related with surface electric field and electron doping, respectively, as a consequence of $in\text{-}situ$ alkali metal evaporation on the surface of a material. I will show the theoretical prediction and experimental results about the Stark effect and screening effect in MX_2. After that, I elaborate about the reason why I selected bulk $MoSe_2$ for this study. In results section, using the rubidium (Rb) alkali metal evaporation, I demonstrate the electric field and electron doping effect in bulk $MoSe_2$.

4.1 Introduction

4.1.1 Stark effect

The Stark effect is the shifting and/or splitting of spectral lines of atoms and molecules due to the presence of an external electric field. It looks like electric field analogue of the Zeeman effect, where a spectral line is split into several components owing to the presence of the magnetic field. The Stark effect can also lead to splitting of degenerate energy levels of different orbitals such as 2s state and 2p states in the Bohr model.

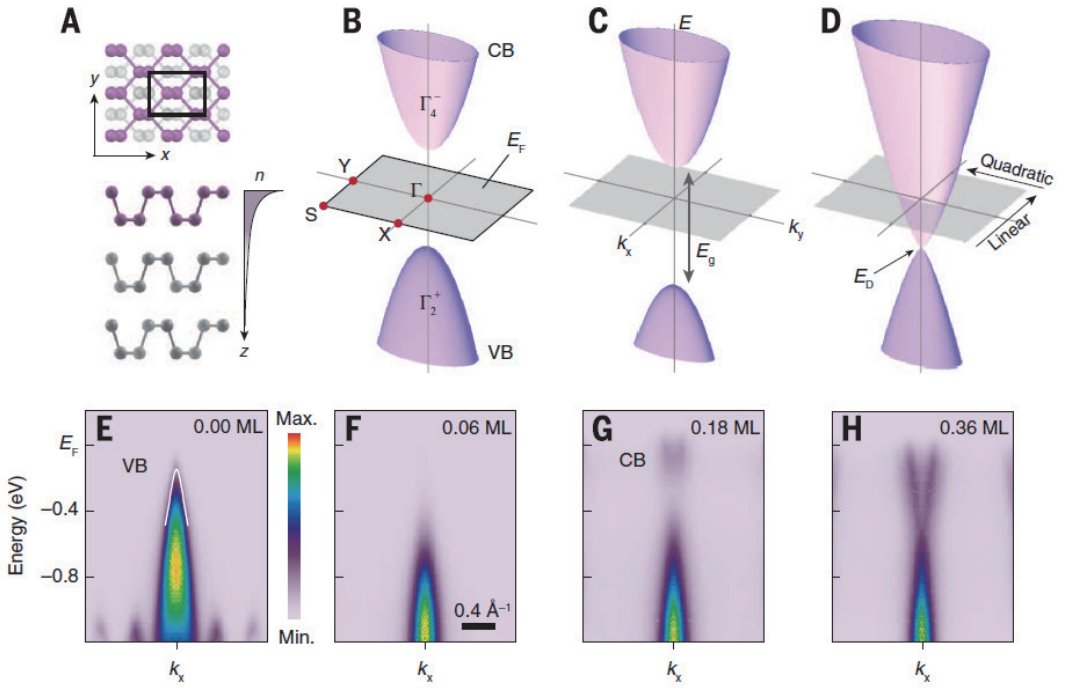

Fig. 4.1: Crystal and electronic structure of black phosphorus without and with electric field[8]. (a) Atomic structure of black phosphorus. (b)-(d) Schematic band structure of black phosphorus under electric field. (e)-(h) Experimental band structure under surface electric field using potassium evaporation.

The Stark effect not only split the spectral lines of atoms and molecules but also can change the electronic band structures. The electric field mixes the nearby subband states in the valence band complex and separately it mixes the nearby subband states in the conduction band complex. This feature leads to the band gap reduction in semiconductors under the enough electric field along the z-direction. Especially, the Stark effect is more dramatic and interesting in semiconducting or insulating materials due to a reduced screening of the electric field[49, 50, 8]. Figure 4.1 shows the band gap closing and reversing in black phosphorus due to the Stark effect. Here, the surface electric field is induced by surface alkali metal (potassium).

4.1.2 Screening effect

In the presence of surface alkali atoms, there is another effect, so called screening effect which also reduces the band gap of semiconductors. The screening effect is the damping of electric fields caused by the presence of mobile charge carriers. It is an important part of the behavior of charge carriers in electronic conductors such as semiconductors and metals. When the alkali metal evaporated on the surface of sample, it donate electron to the sample. Due to this electron, there is screening effect which affects to the band gap. In chapter 6, I will describe the effect of screening in the exciton binding energy of materials.

4.1.3 Theoretical prediction and experimental results about electric field effect in MX_2

Among several strategies recently being employed to engineer band gaps in semiconductors or insulators, external electric field is a particularly interesting one. For example, an external electric field applied perpendicular to the layer of bilayer graphene breaks the inversion symmetry and opens up a band gap. This gap is reversible and continuously tunable more than 200 meV[51]. Recent theoretical study also suggests the possibility of tunable band gap in hexagonal boron nitride[52]. This remarkable strategy can also be applied in not only black phosphorus but also group 6 TMD MX_2.

The electronic states near the Fermi level of bulk MX_2 are dominated by d orbital of transition metal atom and p orbital of chalcogen atom. MX_2 has different orbital character at Γ and K point of valence band. At Γ point, dominant orbital characters are d_{z^2} of transition metal atom and p_z of chalcogen atom. On the other hand, at K point, the occupied part of the d band has dominant d_{xy} and $d_{x^2-y^2}$ character while the unoccupied part is dominated by d_{z^2} orbital character. Due to these different orbital characters in distinct points of the Brillouin zone, electronic structure evolves differently under the

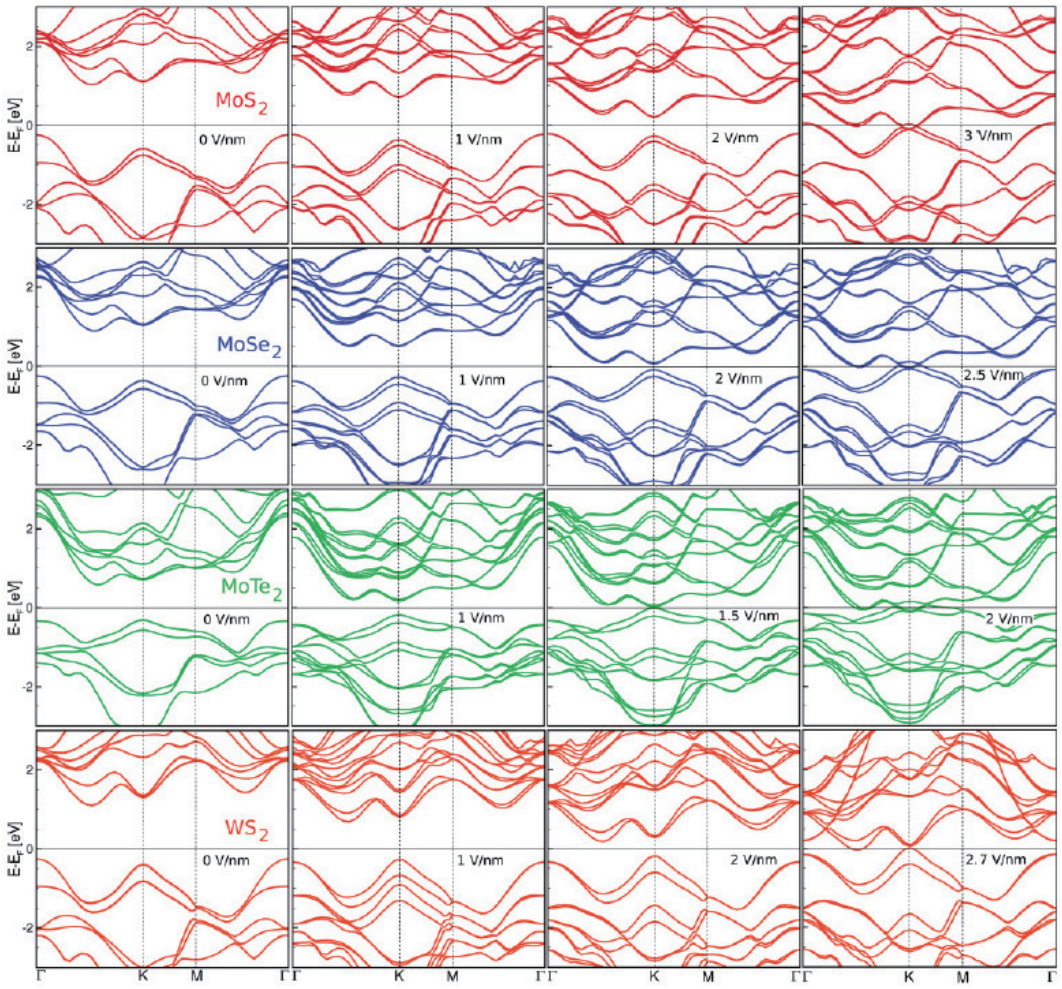

Fig. 4.2: Band structure evolution of bilayer MX_2 (MoS_2, $MoSe_2$, $MoTe_2$, and WS_2) under the electric field[53]. The band evolution of the Γ and K point is different due to the orbital character. MoX_2 compounds exhibit indirect to direct band gap transition before gap closing. On the other hand, for WS_2, the conduction band minimum still remains between Γ and K point, so called Σ point.

external electric field.

Figure 4.2 shows the band structure of MoS_2, $MoSe_2$, $MoTe_2$, and WS_2 as a function of applied external electric field[53]. It is apparent that the band gap in all cases decreases to zero with increasing external electric field. There is no excess electron, so this gap closing mainly comes from the electrical Stark effect.

4.1.4 Bulk $MoSe_2$

Making bulk MX_2 a direct gap material would be highly desirable because the necessity for high quality monolayer MX_2 puts severe limitation on the actual device application. There are many theoretical or experimental studies in search of a way to control or engineer the electronic structure and band gap size in bulk MX_2. It was found that the band gap size of MX_2 can be modified by using various techniques such as electric field[54, 55], chemical doping[56, 57], strain[58, 59], and using different substrates for thin films[5]. Nevertheless, there is no research proposal which shows the indirect to direct band gap transition in bulk MX_2.

I select the bulk $MoSe_2$ for the target material to study the electric field effect using $in\text{-}situ$ alkali metal dosing methods. There are two reasons for choosing the bulk $MoSe_2$. First, experimental conduction band minimum position is located at the K point in MoS_2 and $MoSe_2$, whereas WS_2 and WSe_2 has their conduction band minimum at the Σ point as shown in Figure 3.4. The other is the energy difference between the valence band maximum position at Γ and K point. The energy difference between the valence band maximum at Γ and K point decreases from S atom to Se atom which also shown in Figure 3.4. For example, the energy difference between Γ and K point is about 650 meV in MoS_2 case, while about 370 meV in $MoSe_2$. These two reasons directly affect to not only band gap engineering but also the possibility of indirect to direct band gap transition due to the electrical Stark effect.

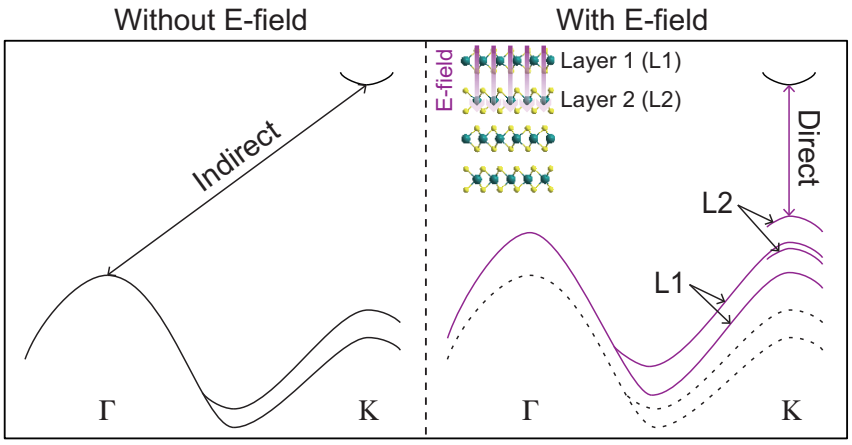

Fig. 4.3: Sketch of electronic structure evolution in bulk $MoSe_2$ under electric field. The nature of the gap (indirect/direct) is marked by the arrows. L1 and L2 refer to the surface and sub-surface layers, respectively.

4.2 Result and discussion

4.2.1 Possible band gap transition under an external electric field

First principles calculations show that electronic band structure of bilayer $MoSe_2$ can be greatly modified by applying an electric field perpendicular to the layers[53]. Bilayer $MoSe_2$, originally an indirect band gap semiconductor, could even become a metal under a strong electric field. In that process, the valence band maximum position moves from the Γ point (without electric field) to K point (with a enough electric field). This indicates an indirect to direct band gap transition under an electric field even though it was not explicitly discussed in the work due to mis-location of conduction band minimum position.

Figure 4.3 shows the schematic band structure of bulk $MoSe_2$ evolves under the electric field. The band gap is generally reduced by both screening and electrical Stark effect. Eventually, bulk $MoSe_2$ will have a direct band gap at the K point when the field becomes strong enough. Note that only

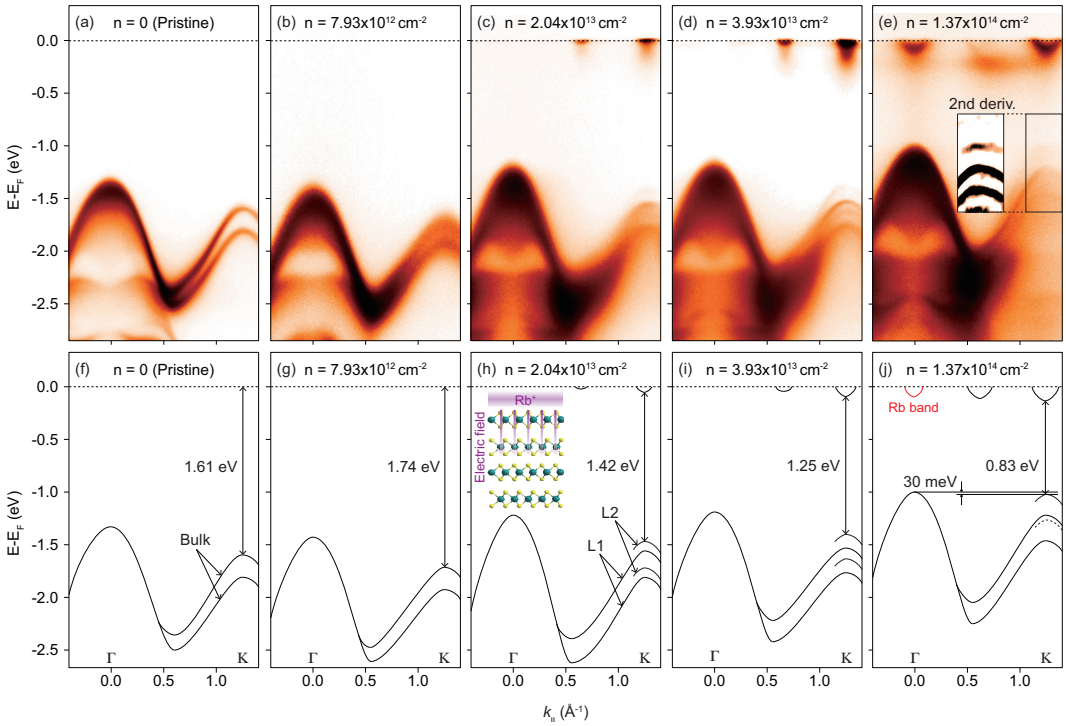

Fig. 4.4: Rb dosing dependent electronic structure of bulk $MoSe_2$. (a-e) Γ-K ARPES data as a function of Rb evaporation. n indicates the electron density doped by Rb atoms. The inset in (e) is the second derivative of the raw data at K point. (f-j) The band structure determined from the ARPES data. The inset in (h) indicates a schematic figure for induced electric field from Rb atoms. The black dashed line in (j) is the deduced lower L2 band which is not clearly distinguished in the data.

the bands near the K point are clearly split by the electric field due to the localized in-plane orbital characters. Electronic states of the lower bands (L2) and upper band (L1) mainly originate from the sub-surface and surface layers, respectively.

4.2.2 Rb evaporated electronic structure evolution of $MoSe_2$

Alkali metal atoms evaporated on the surface of bulk $MoSe_2$ not only dope electrons to the sample but also generate a strong electric field near the

surface due to the remaining alkali metal atoms which give their electrons into bulk $MoSe_2$. I use the rubidium (Rb) source for the alkali metal dosing. My strategy to induce indirect to direct band gap transition is to apply a strong electric field perpendicular to the bulk $MoSe_2$ layers. Valence band dispersions and conduction band minimum were measured by ARPES. The indirect band gap which is about 370 meV smaller than the direct band gap in bulk $MoSe_2$ is greatly reduced due to the alkali metal dosing, almost to the point of indirect to direct band gap transition.

The surface electron doping concentration (electron density, n) is estimated by calculating the Luttinger area of the conduction band Fermi surfaces at Σ and K point, as described in reference paper[47]. Valley multiplicity of the Σ and K points are 6 and 2, respectively. Here, I assume that the Fermi surface shape of Σ and K point is circle. For the low dosing limit, it is almost impossible to observe Fermi surfaces clearly, I assume that the electron doping concentration is proportional to Rb evaporation time.

Figure 4.4 shows the ARPES data taken along the Γ-K direction for various Rb amounts and dispersions determined from the data. Figure 4.4 (a) shows band structure from pristine (before dosing) bulk $MoSe_2$. As the Fermi level (E_F) is in the middle of the gap, we only see the valence band. With small amount of Rb evaporation, electrons are doped into the sample and E_F shifts (rigid band shift) to the conduction band minimum, causing downward shift of the valence band as seen in Figure 4.4 (b), compared to the data from the pristine $MoSe_2$ in Figure 4.4 (a). In principle, the very bottom of the conduction band should be visible but the intensity is too weak to be observed.

As the dosing amount increases further, more electrons are doped into the sample and bottom of the conduction band appears at the K point as well as Σ point as seen in Figure 4.4 (c). The electron density (n) can be measured from the Fermi surface volume of the conduction bands and is estimated to be about 2×10^{13} cm^{-2}. In high Rb dosing level, the electronic structure of bulk $MoSe_2$ shows downward shifts of the conduction band and

upward shifts for the valence band as seen in Figure 4.4 (d) and (e). Also, in such high dosing level, data show the extra band splitting at the K point as I mentioned above. Note that after formation of Rb monolayer which correspond to the situation of Figure 4.4 (e), there is no additional electron transfer from surface Rb atom to the sample as well as almost no electric field effect for additional Rb dosing on top of Rb monolayer. This indicates that there is limitation in the electron doping and electric field using alkali metal dosing methods. The maximum amount of electron density from this method was about $n_{max} \approx 1.4 \times 10^{14}$ cm^{-2}. The maximum induced electric field also limited by Rb monolayer. Figure 4.4 (f)-(j) shows the electronic structure along the Γ-K direction extracted from the ARPES data in Figure 4.4 (a)-(e) for the convenience of eye.

4.2.3 Screening effect and electrical Stark effect on electronic structure of $MoSe_2$

There are two important aspect of the data. One is the evolution of the overall valence band. The valence band shows an upward shift as amount of Rb dosing increase, which seems contrary to what is expected from electron doping. In common case, electron doping in the system makes the downward shift of the valence band (upward shift of E_F). However, using alkali metal evaporation on the surface of the MX_2, there is another factor which is more likely to move upward that leads to band gap reducing. This effect is screening effect due to the surface doped extra electron from alkali metal.

The most important aspect of dosing dependent band structure is electrical Stark effect. The valence band maximum at the K point moves upward faster than that at Γ point as surface electron density increases due to the in-plane orbital character at K point. The experimental results are well matched with the theoretical results with respect to the band gap transition. However the band gap size from the theoretical result seems overestimated or needs more electric field to see the insulator to metal transition.

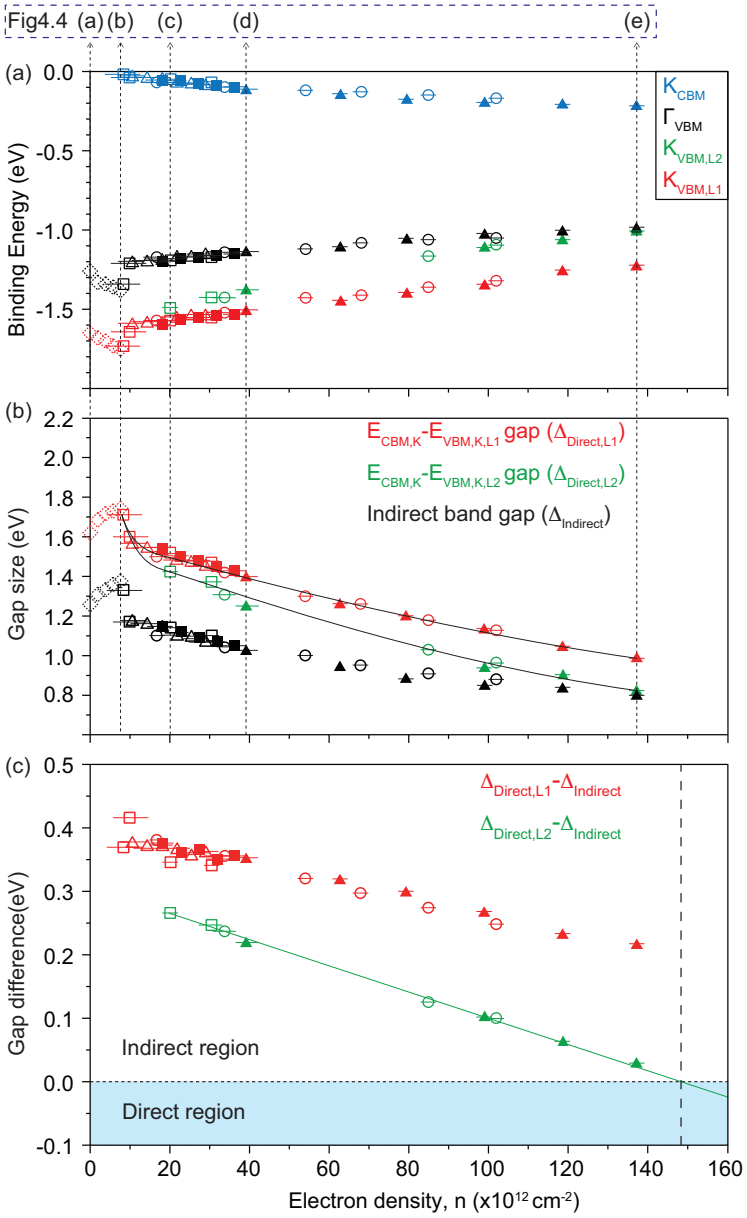

Fig. 4.5: Dosing dependent evolution of the band gap. (a) binding energies of each four points. Data with different symbols come from different sample. Dotted symbols in the low doping region indicate the data from the doping concentration in which conduction band minimum could not be observed. (b) Doping dependent two direct band gap and indirect band gap. (c) The energy difference between the indirect band gap and two direct band gaps at K point.

For the gap behavior and position of each valence band maximum and conduction band minimum as a function of Rb dosing, I plot the Figure 4.5. In Figure 4.5 (a), VB_Γ indicates the valence band maximum position at Γ point, $VB_{K,L1}$ and $VB_{K,L2}$ the valence band maximum position at K point and CB_K shows conduction band minimum position at K point. The vertical dotted lines across Figure 4.5 (a) and (b) indicate the electron densities correspond to ARPES data in Figure 4.4. The position of the valence band maximum at both Γ and K points move downward but conduction band minimum is not seen yet up to electron density of $8 \times 10^{12}\text{cm}^{-2}$. Starting from $n \approx 8 \times 10^{12}\text{cm}^{-2}$, conduction band minimum appears and move downward while the valence band maximum at Γ and K begin to ascend. The most important aspect is that $VB_{K,L2}$ moves faster than VB_Γ and almost catches up with VB_Γ at n_{max}.

Figure 4.5 (b) shows more useful information about the three band gap size. One is indirect band gap size ($\Delta^I = CB_K - VB_\Gamma$) and the other two are direct band gap at K point ($\Delta^D_{L1} = CB_K - VB_{K,L1}$ and $\Delta^D_{L2} = CB_K - VB_{K,L2}$). The energy differences of three band gap show an initially dramatic decrease right after $n \approx 8 \times 10^{12}\text{cm}^{-2}$ but begin to gradually decrease as electron density increases. Such gap decreasing behavior in the doping dependence originates from enhancement of screening effect by extra doped electrons.

The energy difference between CB_K and VB_Γ (Δ^I) is smaller than that of CB_K and $VB_{K,L2}$ (Δ^D_{L2}) in bulk $MoSe_2$ which indicates indirect band gap semiconductor. However, values for Δ^I and Δ^D_{L2} are getting closer as electron density approaches n_{max}. The energy difference between indirect band gap and two direct band gap sizes as a function of electron density are plotted in Figure 4.5 (c). Remarkably, the difference continually decreases with increasing electron density and have linear behavior as shown in Figure 4.5 (c). This strongly suggest that a stronger electric field which correspond to $n = 1.5 \times 10^{14}\text{cm}^{-2}$ can induce an indirect to direct band gap transition in bulk $MoSe_2$ as indicated by the vertical dashed line in the figure.

4.3 Conclusion

$In\text{-}situ$ Rb dosing on the surface has two main effects on the bulk $MoSe_2$: surface electron doping and surface electric field. Surface electron doping not only makes rigid band downward shift but also reduces the band gap size due to the enhanced screening by extra electron[60]. In fact, it has been already experimentally shown that the gap size of monolayer MX_2 thin films can be tuned by controlling screening environment using different substrates. In Figure 4.5 (c), I provide systematic information about this issue in bulk $MoSe_2$. However, it is not enough to induce indirect to direct band gap transition by screening effect. On the other hand, such transition can be attributed to the electrical Stark effect due to the surface electric field. The Stark effect can affect electronic band structures in a momentum dependent way since electronic states can have strong momentum dependence in the orbital character. This is the case of bulk MX_2. This work proposes a new way to induce direct band gap in multilayer or bulk MX_2 by applying external electric field. This should be significant for device application of MX_2.

5 Highly anisotropic electronic structure of ReX_2

In this chapter, I will introduce the theoretical and experimental electronic structure of ReX_2. Due to the low symmetry in crystal structure, its electronic structure has controversies and disparity within several reported papers. I will show the results of published works and remaining issues to be addressed. In result section, using ARPES, I demonstrate the position of global valence band maximum for both materials and quantitatively extract the angle dependent effective hole masses of valence band at Γ point for both materials.

5.1 Introduction

5.1.1 Theoretical and experimental electronic structures of ReX_2

There are mainly two controversies in electronic structure of ReX_2. One is valence band maximum position and another is band gap character (direct or indirect). Here, I just focus on the bulk ReX_2. The resulting structure of ReX_2 has only inversion symmetry and is highly anisotropic in many physical properties, in contrast to the hexagonal TMDs. Also, the staking of layers along the crystallographic c axis is not perpendicular to the layer plane. ReX_2 family have a large number of bands with narrow bandwidth due to the large unit cell.

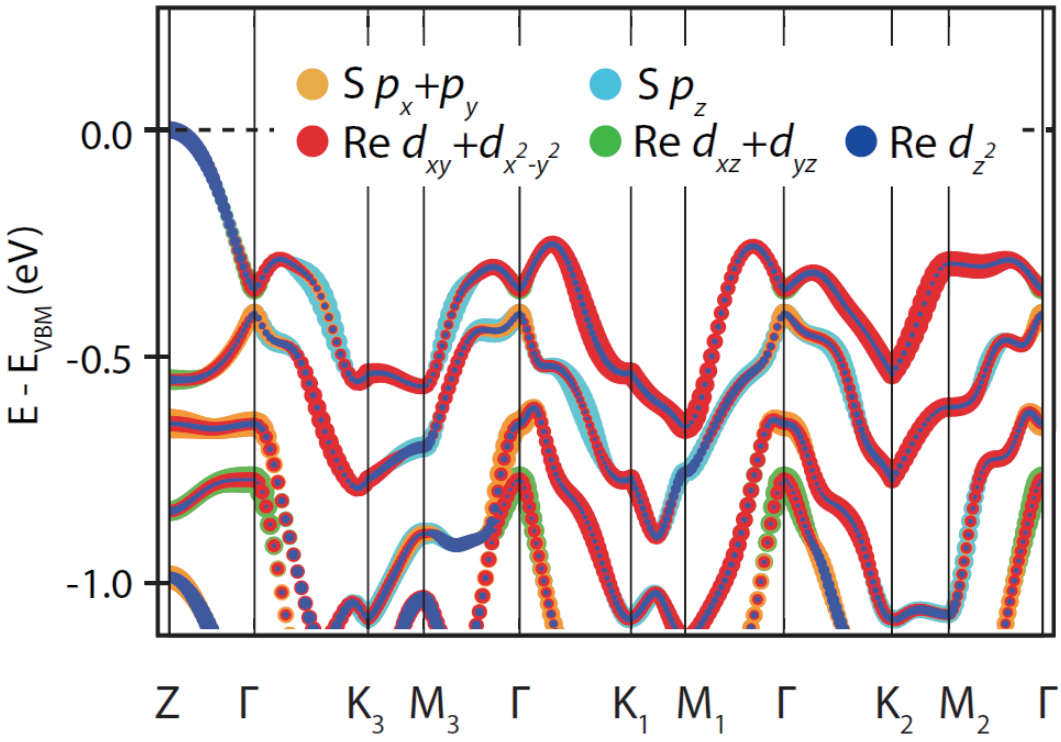

Fig. 5.1: Theoretical electronic structure of bulk ReS_2[61].

Figure 5.1 shows the orbitally resolved valence band dispersion from density functional theory of bulk ReS_2[61]. While the orbital character is strongly mixed throughout the valence bands, this calculations indicate that out-of-plane orbitals (Re $5d_{3z^2-r^2}$) contribute a significant weight close to the valence band maximum position at k_z Z point. On the other hand, in-plane orbitals dominate below the valence band maximum position. More lower bands are dominated by S $3p$ orbitals.

One more important aspect to discuss is the binding energy difference between k_z Γ point and k_z Z point. ReS_2 is well known for almost negligible interlayer coupling. Due to this almost zero interlayer coupling, electronic structure of monolayer and bulk ReS_2 seems almost identical in previous research[19]. However, recent theoretical and experimental data indicate

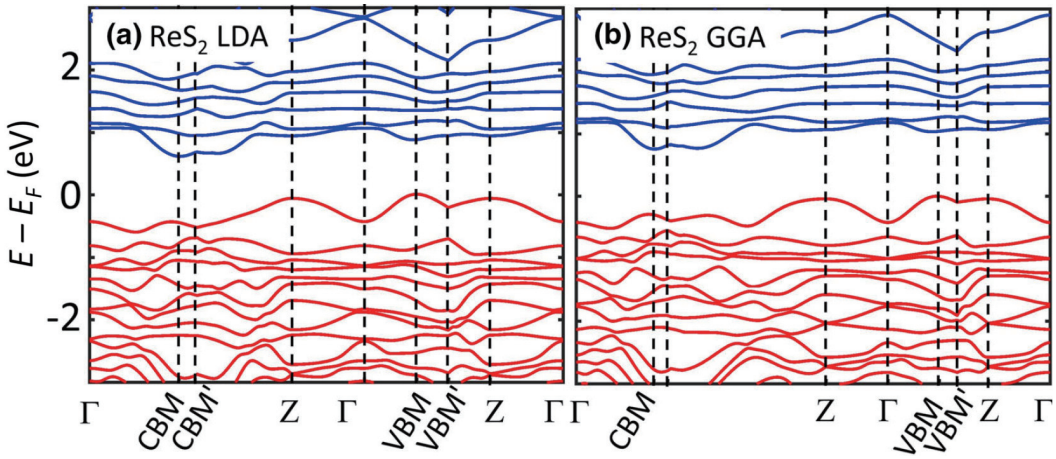

Fig. 5.2: Theoretical electronic structure of bulk ReS_2 using LDA and GGA[62].

that there are quite large interlayer coupling in bulk ReS_2.

Figure 5.2 shows another research about the electronic structures of bulk ReS_2 from the local density approximation (LDA) Perdew-Zunger and generalized gradient approximation (GGA) Perdew-Burke-Ernzerhof exchange-correlation functionals[62]. In this calculation, the valence band maximum is located away from k_z Z point and the precise location of the valence band maximum is hard to determine only via density functional theory. In order to determine the valence band maximum accurately, they use the LDA and GGA approximation. All the essential aspects of the constant energy contours are reproduced though there are minor difference in the exact energies and positions in the valance band maximum.

The position of conduction band minimum is also located away from the high symmetry point (Γ or Z point). Figure 5.2 shows clearly that the valence band maximum and conduction band minimum do not coincide. From this results, they claimed that ReS_2 is formally an indirect band gap semiconductor, but there is slightly larger direct band gap at Z point.

Figure 5.3 shows the experimental electronic structure of ReS_2 using $in-situ$ alkali metal (Rb) dosing ARPES[61]. Here, the valence band maximum

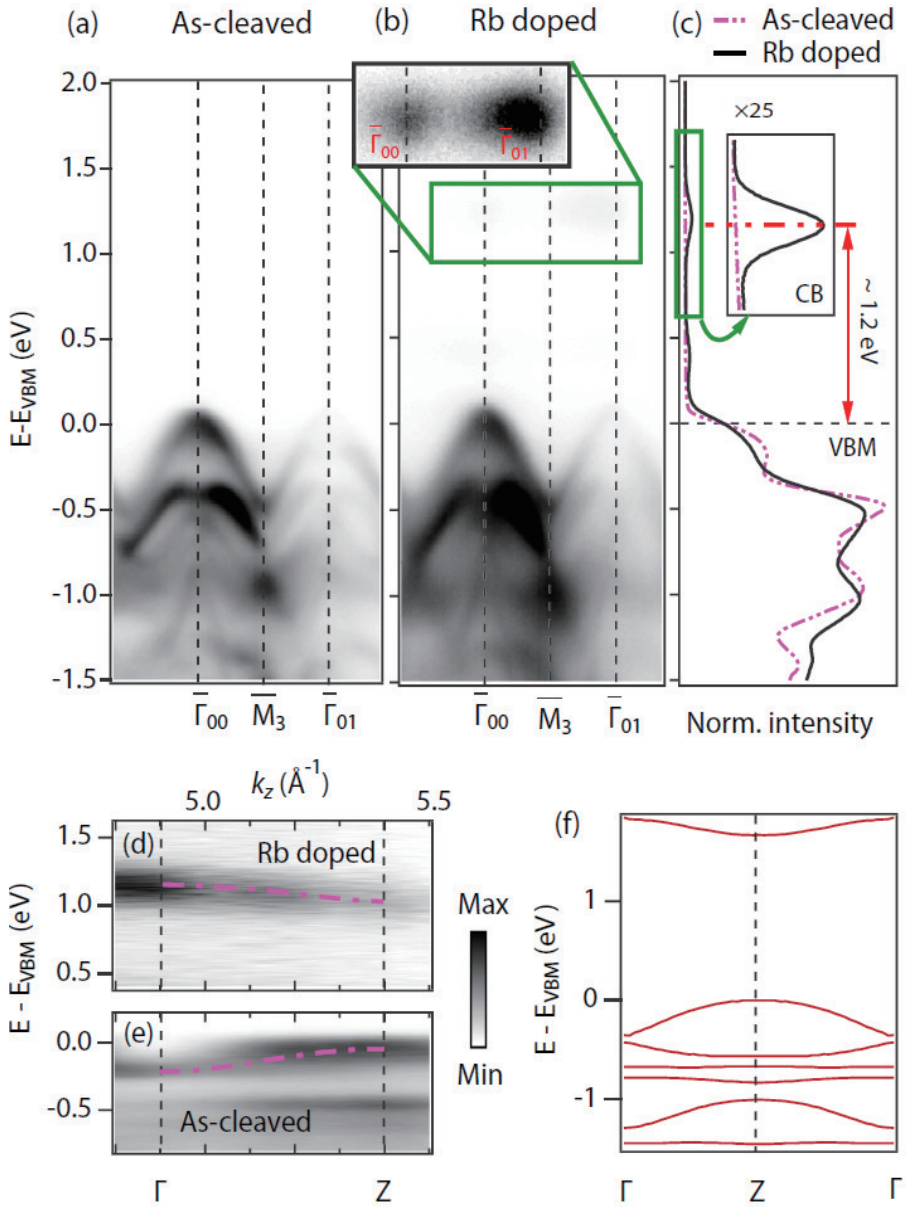

Fig. 5.3: Experimental electronic structure of bulk ReS_2[61].(a) and (b) ARPES data for pristine and Rb-dosed ReS_2. (c) Integrated spectra of energy distribution curves in (a) and (b). (d) and (e) k_z dispersion relationship for Rb dosed and pristine ReS_2. (f) Calculated k_z dispersion from density functional theory.

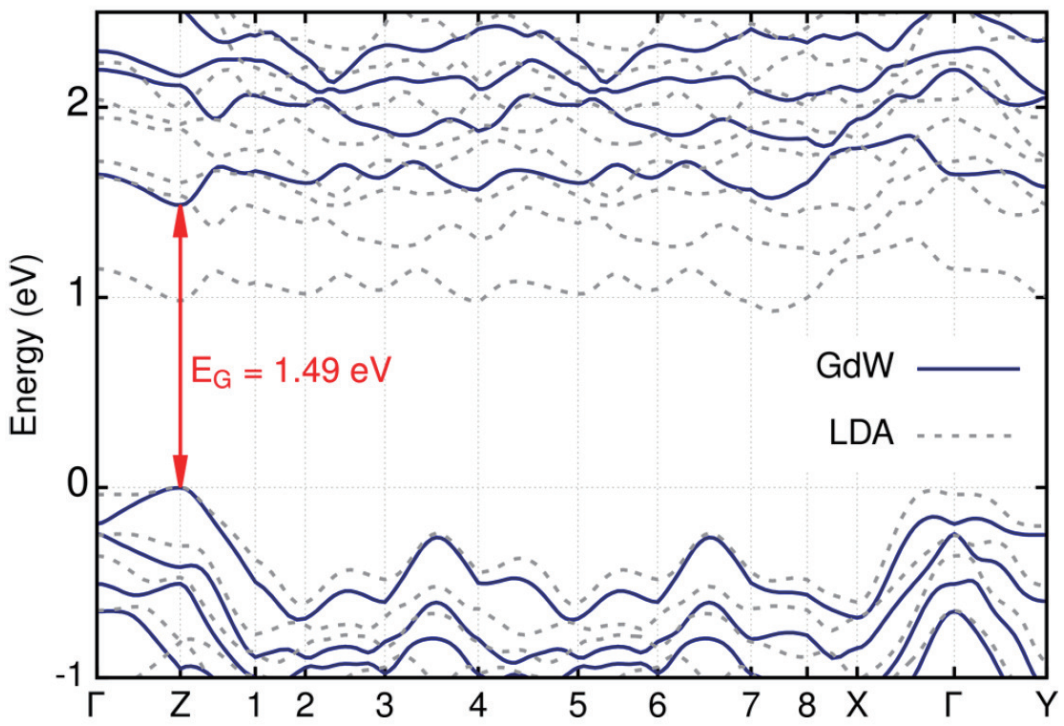

Fig. 5.4: Theoretical electronic structure of bulk $ReSe_2$[63]. The dashed lines indicate the LDA and the solid lines indicate GdW levels for bulk with a direct quasiparticle band gap at k_z Z point.

is located at the k_z Z point and conduction band minimum is also located at k_z Z point. They measured ARPES data from pristine and Rb-dosed (electron doped) bulk ReS_2. Figure 5.3 (b) indicates the conduction band minimum and this new states are populated around 1.2 eV above the valence band maximum located at Z point. Due to the electron screening effect of the excess electron doped by alkali metal, the size of the band gap is about 300 meV smaller than the measured optical band gap rather than inducing a rigid band shift of the conduction band states.

Photon energy dependent ARPES data show that not only the valence band maximum but also the conduction band minimum has a significant k_z dispersion. This results indicate the direct band gap in ReS_2 with high join

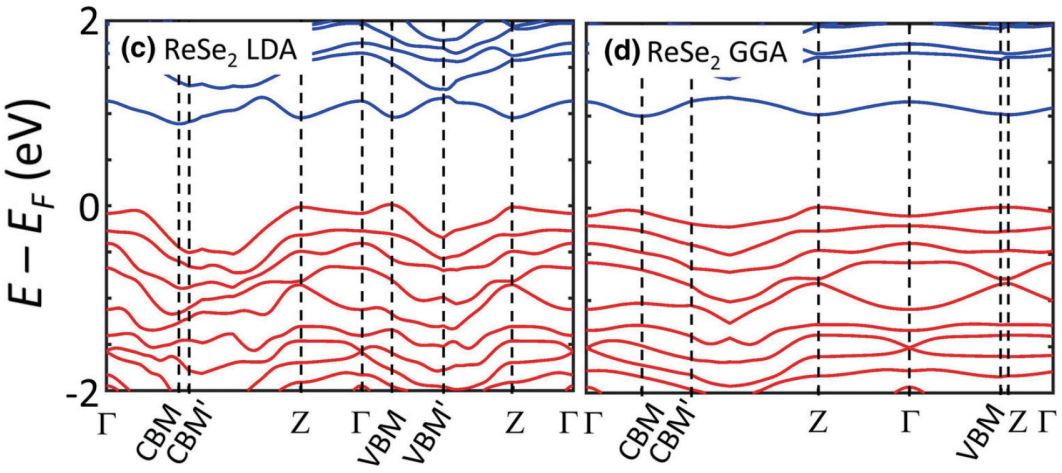

Fig. 5.5: Theoretical electronic structure of bulk ReS_2 using LDA and GGA[62].

density of states. Experimental data is also supported by the density functional theory calculations in Figure 5.3 (f). Here, the size of the out-of-plane dispersion is slightly overestimated by calculations which suggest too high interlayer coupling in the calculations. The results from this work has quite different conclusion with the above mentioned theoretical works.

Not only ReS_2 but also $ReSe_2$ has disparity between the theoretical and experimental works with respect to the global valence band maximum position. Figure 5.4 shows the theoretical band structure of bulk $ReSe_2$ using the LDA and GdW approximation[63]. Because of inversion and time reversal symmetry, each band is two-fold degenerate. In LDA calculation, the band gap character of bulk $ReSe_2$ is indirect band gap and size is 0.92 eV. On the other hand, in the GdW approximation, bulk $ReSe_2$ shows direct band gap with 1.49 eV. Here, the weak interlayer coupling preserves the direct band gap character.

In LDA approximation level, the k_z dispersion along the in-plane Γ point is very small (about 20 meV) which indicates the almost zero interlayer coupling. This weak interlayer coupling will be precisely elaborated in chapter 6 with my ARPES results.

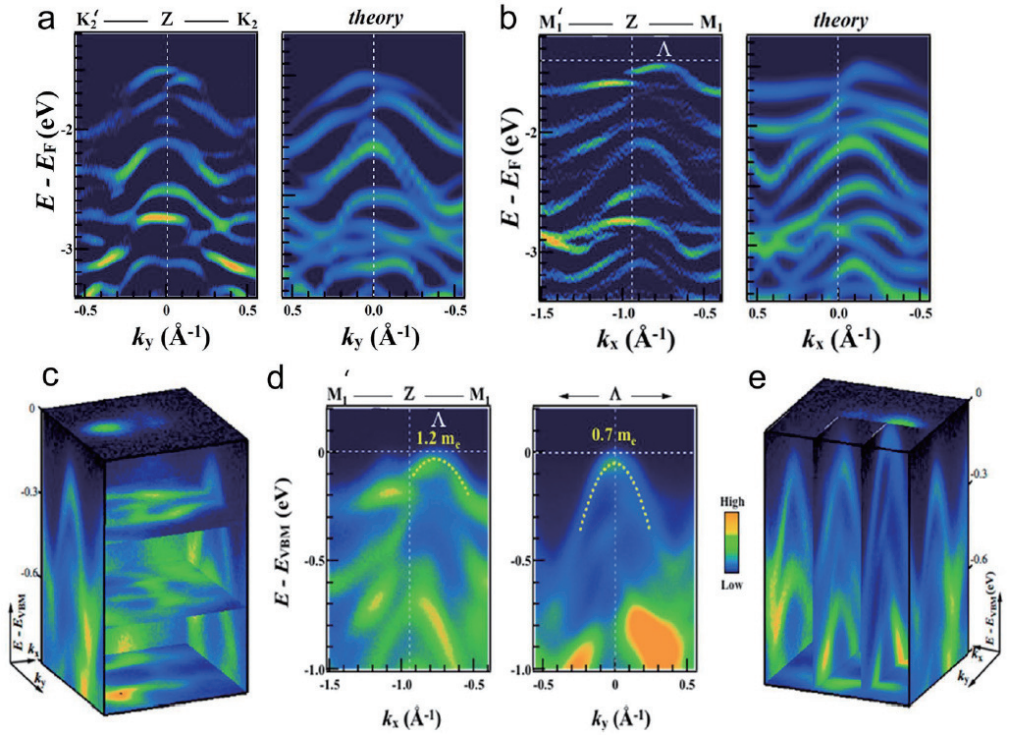

Fig. 5.6: Experimental electronic structure of bulk $ReSe_2$[17]. (a) Measured and calculated valence band dispersions along the K_2-Z-K_2 direction and (b) M_1-Z-M_1 direction. M_1-Z-M_1 direction is perpendicular to the Re chain in real space and K_2-Z-K_2 direction is parallel to the Re chain direction in real space. (c) Constant energy contours of bulk $ReSe_2$. (d) Extracted effective mass of two direction in bulk $ReSe_2$. (e) 3D data plot of (b).

Bulk $ReSe_2$ also has controversies in its valence band maximum position. Figure 5.5 shows another theoretical band structure with equivalent constant energy surface of bulk $ReSe_2$. Here, they claimed that bulk $ReSe_2$ has indirect band gap character within the two calculation methods and valence band maximum is located away from the k_z Z point. The size of the indirect band gap is 0.87 eV and 0.99 eV in LDA and GGA approximation, respectively.

Figure 5.6 shows the experimental electronic structure of bulk $ReSe_2$. The valence band maximum position of bulk $ReSe_2$ in this research is k_z Z point

along the k_z line but not at the in-plane Γ point. They claimed that the valence band maximum position is slightly located away from in-plane Γ point, but their quality of experimental data is quite low. Also, there is no two fold symmetry along the M_1-Z-M_1 direction. This is quite odd feature and my experimental results are different with respect to not only effective mass but also the valence band maximum position. I will discuss this in result section.

Location of valence band maximum is important issues to determine the band gap character. $ReSe_2$ has two possible points at in-plane k space which can be the valence band maximum as shown in Figure 5.7. One is at $k_{\|} = 0$ $Å^{-1}$, another is at $k_{\|} = -0.12$ $Å^{-1}$. For the $k_{\|} = 0$ $Å^{-1}$ case, the corresponding energy distribution curves are shown in Figure 5.7 (b) as red line scans. For the non-normal electron emission ($k_{\|} = -0.12$ $Å^{-1}$) case, the experimental results are shown in Figure 5.7 (b) as black line scans. With increasing k_z (photon energy), the theory predicts the local valence band maximum first at negative $k_{\|}$ values. Then it appears at $k_{\|} = 0$ $Å^{-1}$ when approaching the k_z Z point, where the global valence band maximum is located in theory.

In addition, the experimental data are compared with the calculated dispersion along k_z direction as shown in Figure 5.7 (c) and (d). They claimed that the bandwidth is about 165 meV. However, the resolution of this experiment is not good enough to determine the bandwidth of bulk $ReSe_2$ accurately.

In Figure 5.7 (c) and (d), while there is qualitative agreement between theoretical and experimental valence band maximum position, the new maximum in experiment appears at lower energy as a saddle point in theory. Unfortunately, due to the limitation of the experimental resolution, they cannot distinguish whether the global valence band maximum position is at the above mentioned non-high-symmetry point in k space or at the k_z Z point.

Due to the complicate lattice structure and low symmetry, the theoretical and experimental electronic band structure of both bulk ReS_2 and $ReSe_2$ is very complicate and controversial as mentioned above. In order to determine

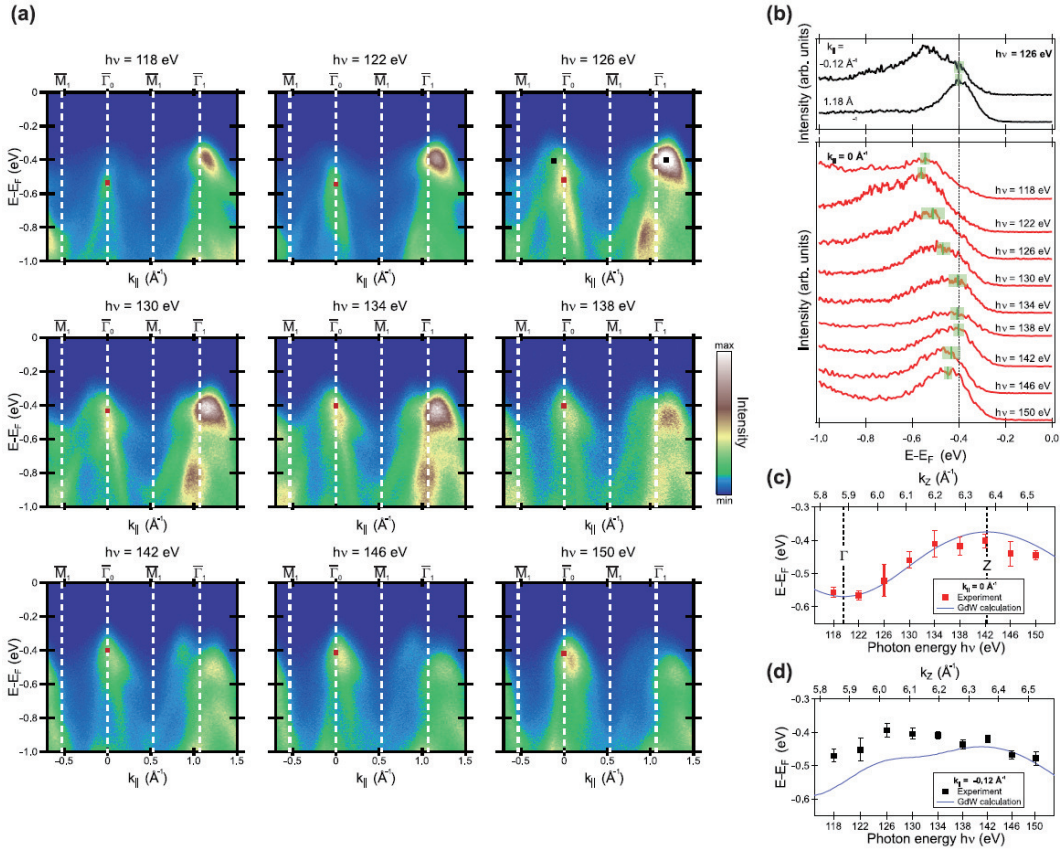

Fig. 5.7: Location of the valence band maximum in bulk $ReSe_2$[18]. (a) Photon energy dependent ARPES data along the perpendicular to the Re chain direction. (b) Energy distribution curves for normal emission and certain points in k space. (c) and (d) k_z dispersion relationship of the highest valence band for $k_{||} = 0$ Å^{-1} and $k_{||} = -0.12$ Å^{-1}. The solid line indicate the calculated k_z dispersion using GdW theory.

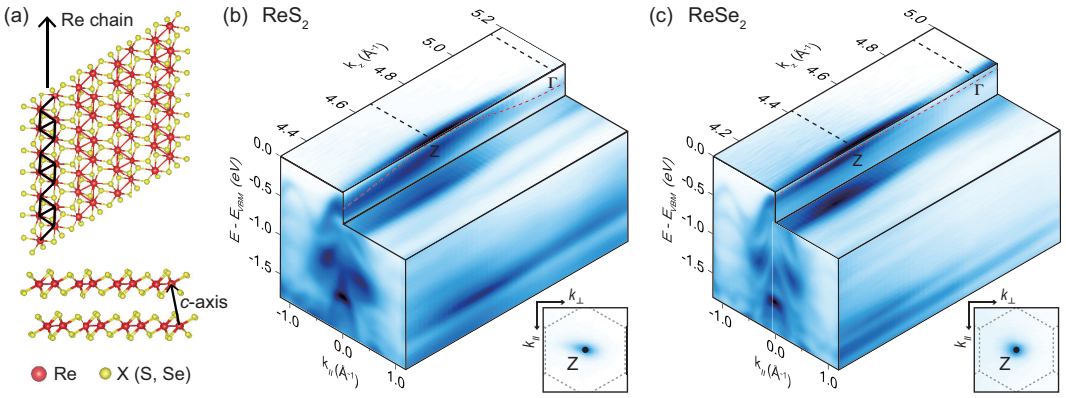

Fig. 5.8: Crystal structure and out-of-plane valence band dispersions. (a) Top and side views of the crystal structure of ReX_2 (X = S, Se). It shows distorted 1T structure with Re chains indicated by black solid lines. (b, c) Intensity plots of ReS_2 and $ReSe_2$ ARPES data in the energy and momentum space, respectively. k_z dependent intensities are taken by using different photon energies from 60 eV to 110 eV with 2 eV step. k_z is obtained with inner potentials of 17.8 and 12.4 eV for ReS_2 and $ReSe_2$, respectively. Red dashed lines are guides to eye for k_z dispersion of the top-most valence bands (E = E_{VBM}). Insets are 2D constant energy intensity map in the momentum-space (as functions of $k_{||}$ and $k_{\perp}$) at the k_z = Z point. Note that there is a single peak at the zero in-plane momentum point (Z point).

the valence band maximum position and accurately measure the experimental electronic band structure of both material, I use high resolution ARPES.

5.2 Result and discussion

5.2.1 Global valence band maximum position of ReX_2

First, I address the issue about the global valence band maximum position of ReX_2. In order to measure the valence band maximum accurately, I first measure the photon energy dependent ARPES from 60 eV to 110 eV for both materials as shown in Figure 5.8.

From the photon energy dependent ARPES measurement, the inner potential can be estimated from the k_z dispersion of electronic band with the

reciprocal lattice vector c^*. Based on the results of reported X-ray diffraction measurement[64], the reciprocal lattice vector c^* is calculated to be 1.032 $Å^{-1}$ (0.984 $Å^{-1}$) for ReS_2 ($ReSe_2$). The estimated inner potentials are V_0 = 17.8 and 12.4 for ReS_2 and $ReSe_2$, respectively. These estimated inner potential values are similar to those of other TMD materials[39, 65]

After photon energy dependent ARPES measurement, I take ARPES intensity maps on both materials to obtain electronic band dispersions of the hole carriers. ARPES intensities as a function of the energy referenced to the valence band maximum (E_{VBM}) are mapped along two momentum directions, parallel to chain ($k_{\|}$) and perpendicular to the layer (k_z) (Figure 5.8 (b) and (c)). While many narrow band dispersions are observed within the experimental energy range, the top-most valence band is of interest as it determines the low energy properties of the materials such as electrical conductivity or optical conductivity. Due to the van-der Waals layered structure, the top-most bands of ReS_2 and $ReSe_2$ show relatively weak dispersions along k_z than along in-plane momentum. Interestingly, we observed as shown in Figure 5.8 that the k_z dispersion of $ReSe_2$ (about 20 meV) is even weaker compared to that of ReS_2 (about 150 meV) which is known as a material with very weak inter-layer interaction[19]. Therefore, our results show an strong evidence for even smaller interlayer coupling between layers in $ReSe_2$, not ReS_2.

From the photon energy dependence data, I reveal that valence band maximum is located at Z for both ReS_2 and $ReSe_2$ as indicated by the red dashed lines in Figure 5.8 (b) and (c). While previous ARPES studies also showed that valence band maximum of ReS_2 is located at Z, valence band maximum of $ReSe_2$ has been under debate. One paper reported that the k_z for valence band maximum of $ReSe_2$ is located at the Z point but the in-plane momentum was reported to be non-zero[17]. More recently, another paper reported two valence band maximum of $ReSe_2$[18]. One of them is at Z point and the other is away from Z point. However, they could not decide which is global valence band maximum, due to the limitation of their experimental resolu-

tion. In my case, the global valence band maximum of $ReSe_2$ can be decided to be located at Z point owing to relatively high quality data. In fact, I find that $ReSe_2$ result about valence band maximum is consistent with a recent theoretical prediction as well[63].

As mentioned above, I address the issue on the position of the global valence band maximum in $ReSe_2$ as shown in Figure 5.9. For exact determination, I choose two in-plane momenta ($k_\perp$ = 0 Å^{-1} and $k_\perp$ = $-$0.12 Å^{-1}) which are possible global valence band maximum in previous reports[18]. For $k_\perp$ = 0 Å^{-1}, the valence band maximum is located at k_z Z point and for $k_\perp$ = $-$0.12 Å^{-1}, the valence band maximum is located at non-high symmetry point along k_z direction. Comparing these two momenta, my data clearly show that the global valence band maximum is located at the Z point. I demonstrate that the binding energy of the top most band is about 10 meV higher at the Z point (k_z = 4.43 Å^{-1}), which can be obtained by 68 eV photon energy, than any other point as shown in Figure 5.9 (d).

5.2.2 Angle dependent effective hole mass of ReX_2

In order to accurately investigate the effective mass of the hole carrier which affects to the electrical or optical properties, I analyze ARPES data obtained at the same in-plane momentum space which includes the Z point. As shown in Figure 5.10 (a) and (b), constant energy contours of ReS_2 and $ReSe_2$ at E $-$ E_{VBM} = $-$0.2 eV show two-fold symmetry due to Re chain and strong anisotropic band contours which are not closed along the direction perpendicular to the chain. From now on, I refer to "Re chain" as "chain". These observations indicate much narrower bandwidth along the direction perpendicular to the chain. The top-most band dispersions, which I am interested in, along the chain are much stronger than those along the other for both ReS_2 and $ReSe_2$. For quantitative analysis, I try to fit the band dispersions with a quadratic function for which the effective mass is a free parameter[63]. The yellow dotted lines in Figure 5.10 (c) and (d) indicate the fit functions. From

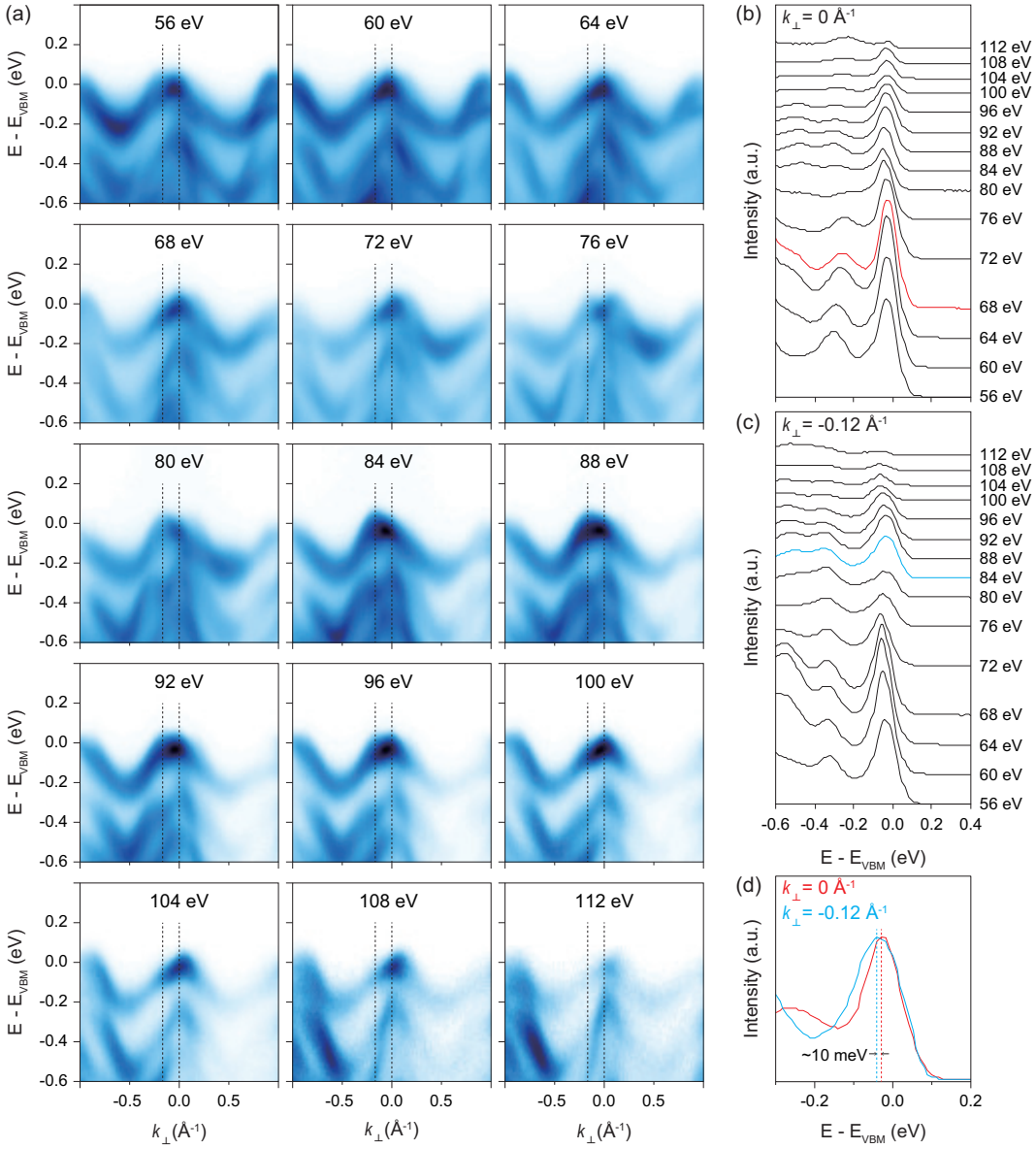

Fig. 5.9: Photon energy dependent high symmetry cuts of $ReSe_2$. (a) High symmetry cuts perpendicular to the Re chain for various photon energies from 56 eV to 112 eV. Energy step is 4 eV. Black dotted lines indicate positions of the in-plane momentum $k_\perp = 0$ Å^{-1} and $k_\perp = -0.12$ Å^{-1}. Energy distribution curves (EDCs) of (b) $k_\perp = 0$ Å^{-1} and (c) $k_\perp = -0.12$ Å^{-1} for different photon energies. Red and blue lines are valence band maximum of $k_\perp = 0$ Å^{-1} and $k_\perp = -0.12$ Å^{-1}, respectively. (d) Expanded view of the two EDCs (red and blue curves in (b) and (c), respectively) for a better comparison.

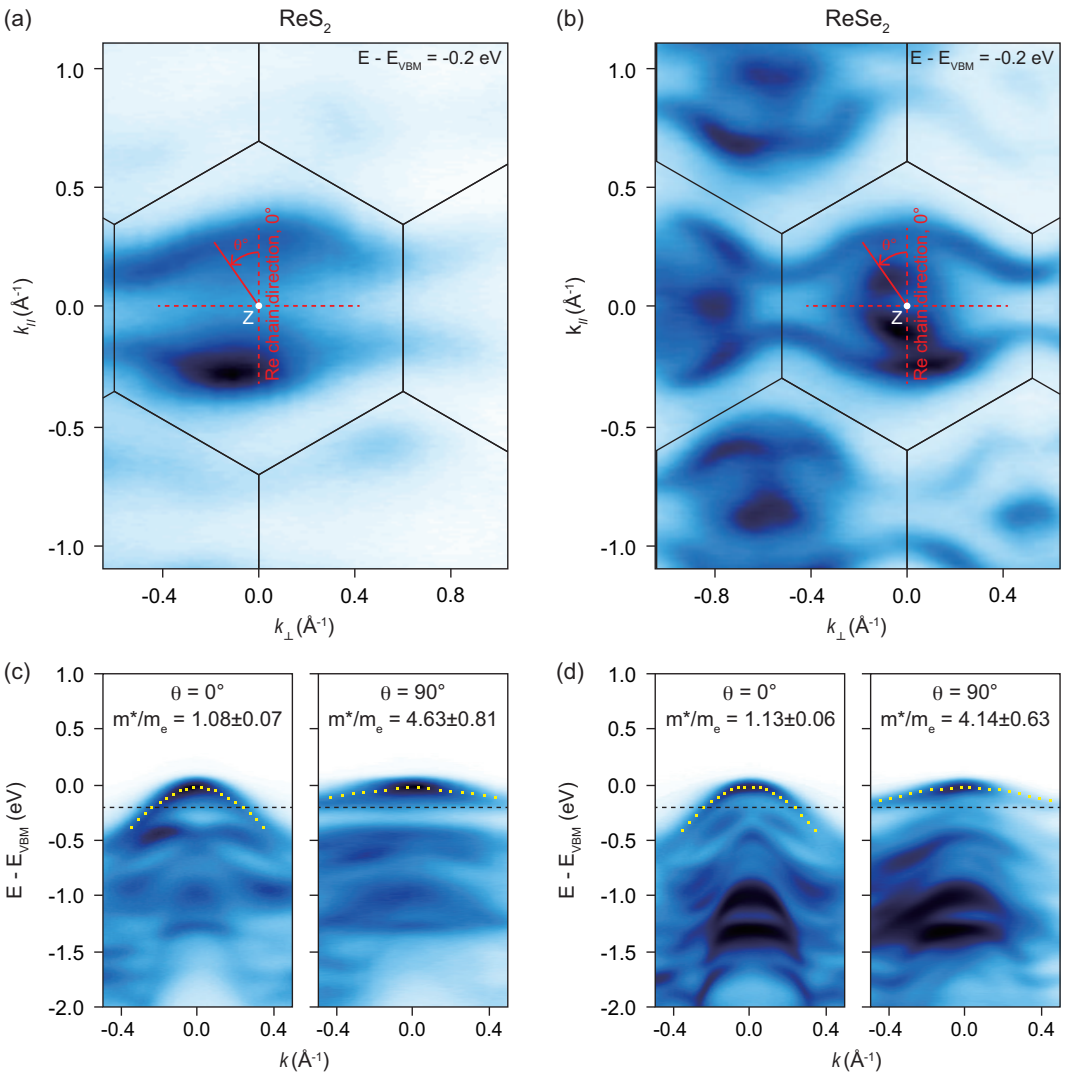

Fig. 5.10: In-plane valence band dispersions near the valence band maximum. Constant energy (E $-$ E_{VBM} $=$ -0.2 eV) contours of (a) ReS_2 and (b) $ReSe_2$. The photon energy used for the experiment was 70 eV for ReS_2 and 68 eV for $ReSe_2$. For these photon energies, k_z = Z point (white dot) where valence band maximum is located is included in the data. Red dashed lines in (a) and (b) indicate the direction parallel and perpendicular to the Re chain as shown in the figure. The honeycomb structured line indicates the projected Brillouin zone boundary. (c, d) High symmetry cuts along ($\theta = 0°$) and perpendicular ($\theta = 90°$) to the Re chain. The yellow dotted lines in (c) and (d) are quadratic fit to the top-most bands. The effective masses of hole carriers along both direction of ReX_2 extracted from the fitting functions are shown in figures.

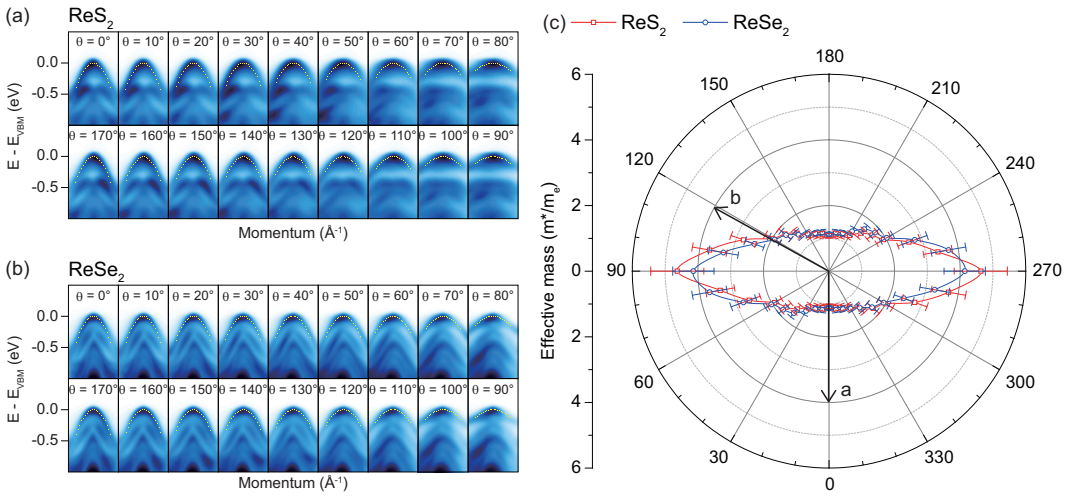

Fig. 5.11: Anisotropic effective hole masses. ARPES cut data along the in-plane momentum defined by the angle θ (see Figure 5.10 (a) for definition) for (a) ReS_2 and (b) $ReSe_2$. All the data sets are centered around the Z point at which valence band maximum is located. The yellow dotted lines indicate a quadratic function fitting the dispersions of the top-most bands. The effective mass from the quadratic fit function for each angle can be extracted and is plotted for ReS_2 and $ReSe_2$ in (c). Arrows indicate crystallographic orientation of ReX_2.

my data, extracted effective hole masses along the direction parallel to the chain (1.08 m_e for ReS_2 and 1.13 m_e for $ReSe_2$) are much lighter than the effective hole masses along the direction perpendicular to the chain (4.63 m_e for ReS_2 and 4.14 m_e for $ReSe_2$). That is, the effective mass along the direction perpendicular to the chain is about 4 times heavier than that along the chain for both ReS_2 and $ReSe_2$. This in-plane anisotropy value in the effective hole mass is the largest among semiconducting TMDs[66, 67].

The valence band dispersion can also be analyzed for different theta angle and corresponding effective hole mass can be obtained. Shown in Figure 5.11 (a) and (b) are ARPES data along in-plane momentum set by the θ angle defined in Figure 5.10 (a). The data are subsequently analyzed and the corresponding effective hole mass is obtained for a systematic study of direction dependence. Note that the top-most band can be fitted well with a

quadratic function indicated by dotted lines, which makes us confident in my analysis. The extracted effective mass from the quadratic function is plotted in polar coordinate as a function of the theta angle in Figure 5.11 (c). The plot clearly shows two-fold symmetry and strong in-plane anisotropy of the effective hole mass for both ReS_2 (red) and $ReSe_2$ (blue).

There is an important point to discuss in comparison with the results of first principles calculations on ReS_2. The experimentally observed effective mass is about twice larger than that from the first principles calculations. The effective mass from the first principles calculations is 2.4 m_e along the direction perpendicular to the chain and 0.8 m_e along the chain[68]. The electron-electron and electron-phonon interaction or atomic spin-orbit coupling of Re atom which were not considered in the calculation may play a crucial role in the clear enhancement of the effective hole mass.

5.3 Conclusion

In this study, I performed systematic ARPES measurement and analysis of ReS_2 and $ReSe_2$ to reveal the energy-momentum dispersion relationships of the top most valence bands. I found that $ReSe_2$ have much smaller k_z dispersion than ReS_2, indicating the more 2D-like feature in $ReSe_2$ than in ReS_2. Also, I systematically investigated in-plane directional dependence of the effective hole masses of ReS_2 and $ReSe_2$. The effective masses show strong anisotropy, about 4 times heavier along the direction perpendicular to the chain than the direction parallel to the chain. In-plane anisotropy of the hole effective masses in ReS_2 and $ReSe_2$ is larger than in black phosphorus which also shows anisotropic electrical and optical properties[69, 70]. Therefore, ReS_2 and $ReSe_2$ are quasi 1D materials in terms of the low energy hole carrier dynamics, which makes ReS_2 and $ReSe_2$ promising bulk materials for 1D semiconducting electronics. The effective mass of ReS_2 observed by ARPES is found to be significantly enhanced compared to that from

first principles calculations. Electron-electron and electron-phonon interactions or atomic spin-orbit coupling of Re atom may be attributed to the mass enhancement. The quasi 1D character of the hole carriers as well as possibility of the electron-electron and electron-phonon interactions may leads to charge density wave order if enough amount of hole carriers are doped into ReS_2 and $ReSe_2$.

6 Giant exciton binding energy of $ReSe_2$ and importance of k_z dispersion

In this chapter, I will demonstrate the extremely large exciton binding energy in bulk $ReSe_2$ using scanning tunneling spectroscopy (STS), ARPES, and optical spectroscopy (Ellipsometry). First, I will briefly introduce the exciton related physics in 2D and 3D system and exciton binding energy. In the experiment section, I will explain about two experimental tools, scanning tunneling microscopy and ellipsometry, which are used for measuring band gaps of materials. In results section, I will show the ARPES cut data of high symmetry point along k_z direction (Z point and Γ point) of ReX_2 to demonstrate the 2D character of bulk $ReSe_2$. After that, I will show two band gaps and exciton binding energies of both materials which can be extracted from subtracting two band gaps. Lastly, I will elaborate the relation between exciton binding energy and k_z dispersion of both materials.

6.1 Introduction

6.1.1 Exciton and exciton binding energy

An exciton is a bound state of quasiparticle which consist of an electron and a hole. An electron and a hole attracted to each other by electrostatic Coulomb force. Exciton is an electrically neutral quasiparticle formed in insulators, semiconductors and in some liquids which have band gaps in their electronic band structure. The exciton is elementary and important quasiparticle of

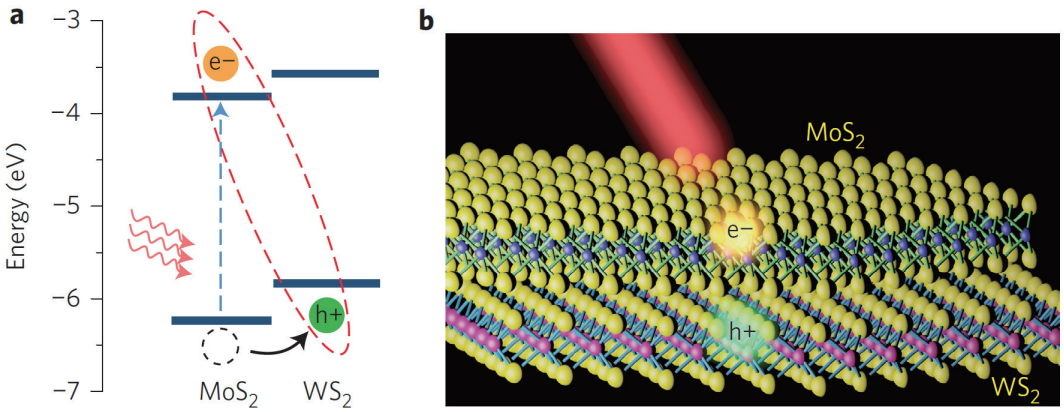

Fig. 6.1: Schematic figure about band diagram and atomic structure of MoS_2/WS_2 heterostructures. (a) Theoretically predicted band diagram of MoS_2/WS_2 heterostructures. (b) Illustration of electrons and holes which form charge-transfer excitons. Electrons and holes for charge-transfer excitons are created by photon in different kind of layers.

not only condensed matter physics, but also device application due to their capability of energy transportation without transporting net electric charge.

An exciton can form when light is absorbed by a material with band gap. Here, band gap size is not important when form the exciton. Incident light excites an electron from the valence band to the conduction band. Then, this leaves behind a hole (positive charge) in the valence band. The electrons in conduction band and holes in valence band are attracted each other by electrostatic Coulomb forces. This attraction between electrons and holes provides a stabilizing energy balance. Consequently, the exciton has slightly less energy than the unbound electron and hole. The wave-function of the exciton state is known to be hydrogenic because this bounded exciton state akin to that of a hydrogen atom. However, the size of exciton is much larger and the binding energy of exciton is much smaller than a hydrogen atom. This is because of both the screening effect by other electrons which do not formed exciton in the semiconductor and small effective masses of the excited electron and hole (The binding energy of exciton is closely related with

reduced effective mass and dielectric constant of material). I will discuss this later.

There are mainly three types of exciton, Frenkel, Mott-Wannier, and charge-transfer exciton. Commonly in organic molecules which has relatively smaller dielectric constant than inorganic materials, the size of excitons tend to be small due to the strong attractive Coulomb interaction between an electron and a hole which is almost the same order of the unit cell. These organic material based molecular excitons, for example as in fullerenes, may even be entirely located on the same molecule. This Frenkel exciton has its binding energy ranging from 0.1 to 1 eV. As I mentioned above, Frenkel excitons are typically found in alkali halide crystals and in organic molecular crystals. Due to this extremely large exciton binding energy, organic materials which have Frenkel excitons are widely studied in device applications such as excitonic solar cell.

On the other hand, generally in inorganic semiconductors, the dielectric constant is relatively large. Consequently, due to the electric field screening, the Coulomb interaction between electron and hole is reduced. This is the case of a Mott-Wannier exciton, which has relatively larger radius than the lattice spacing of the unit cell. Small effective mass of electrons also favors large exciton radii. As a result, the effect of the lattice potential can be incorporated into the effective masses of the electron and hole. Likewise, due to the lower masses and the screened Coulomb interaction, the exciton binding energy is usually much less than that of a hydrogen atom or Frenkel exciton, typically on the order of 0.01 eV. Mott-Wannier excitons are typically found in inorganic semiconductors which have small energy gaps and high dielectric constants such as MoS_2, $MoSe_2$, WS_2, and WSe_2. They are also known as large excitons due to their size.

An intermediate case between Frenkel and Mott-Wannier excitons is charge-transfer exciton. This type of exciton forms when the electron and hole occupy adjacent molecules or forms in bilayer van-der Waals heterostructures. In van-der Waals heterostructure, electron is located in one monolayer and

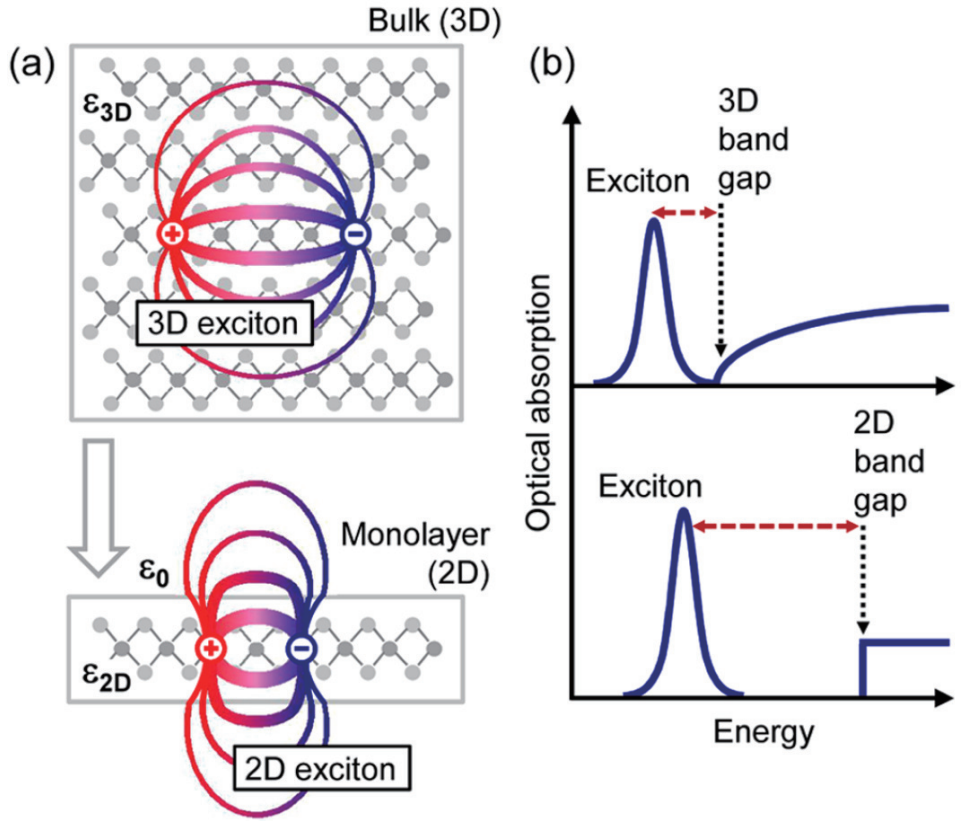

Fig. 6.2: Schematic figure of exciton in 3D and 2D system. (a) Real space representation of excitons in 3D and 2D system. (b) Electronic and optical band gap of 3D and 2D system represented by optical absorption picture.

the other hole is located in the other monolayer as shown in Figure 6.1[71]. Due to this spatial isolation of electron and hole, exciton lifetime is generally very long in comparison with other excitons.

The binding energies of excitons are significant for optoelectronics and photovoltaic devices. Exciton binding energy is defined by subtracting the optical band gap from electronic band gap which can be determined by optical spectroscopy and scanning tunneling spectroscopy, respectively. In common inorganic semiconductors which generally forms Mott-Wannier excitons, the size of exciton binding energy is relatively smaller than that in

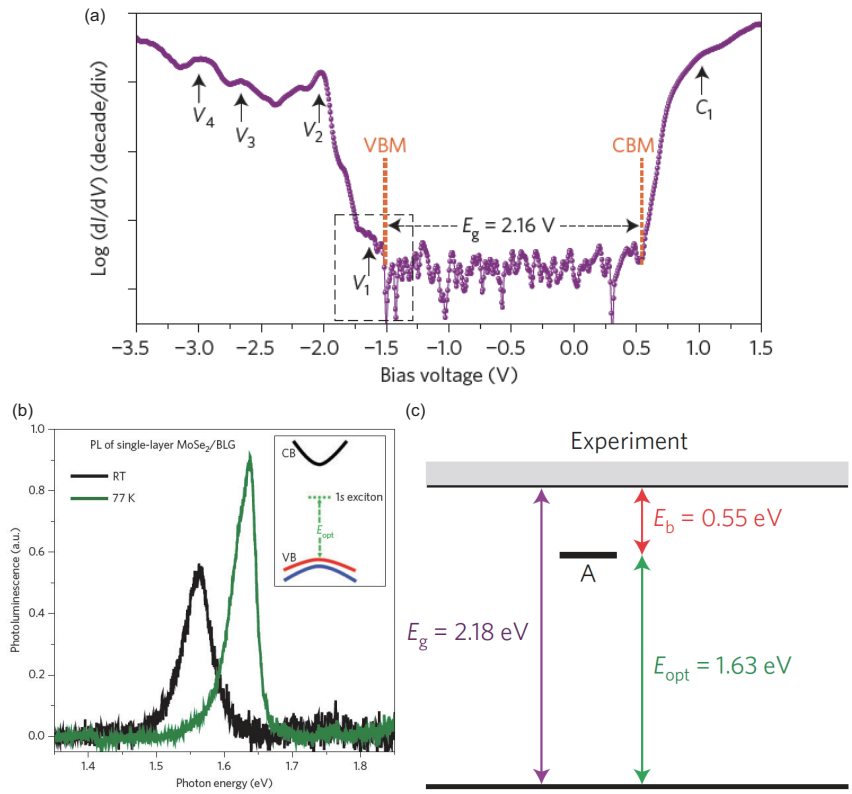

Fig. 6.3: Exciton binding energy of monolayer $MoSe_2$ on bilayer graphene. (a) Electronic band gap of monolayer $MoSe_2$ using scanning tunneling spectroscopy. (b) Optical band gap of monolayer $MoSe_2$ using photoluminescence. (c) Summary of experimental results and extracted exciton binding energy of monolayer $MoSe_2$.

organic semiconductors.

6.1.2 Exciton in 3D and 2D system

When excitons are formed in 3D system, usually excitons have small binding energy due to the large dielectric screening environment. This large dielectric screening affects to reduction of electronic band gap and Coulomb interaction which are essential part of exciton binding energy. The upper part of Figure 6.2 (a) shows the schematic figure of excitons in 3D system.

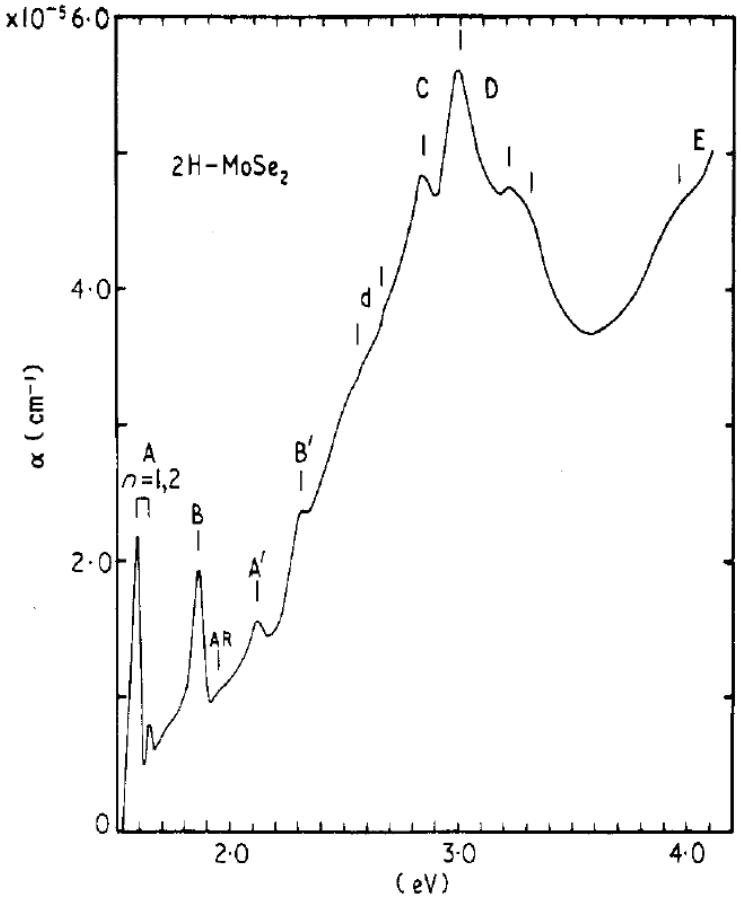

Fig. 6.4: Absorption spectrum of bulk $MoSe_2$.

Due to the upper and lower side layers, excitons in 3D system undergo large dielectric screening.

On the other hand when excitons are formed in 2D system, excitons have large exciton binding energy in comparison with 3D system due to the small dielectric screening environment as shown in lower part of Figure 6.2 (a). In 2D system, There is almost no reduction in the electronic band gap. Figure 6.3 shows the example of 2D system (Monolayer $MoSe_2$ on bilayer graphene) which has extremely large exciton binding energy around 550 meV. One can notice that if there is no substrate, i.e. freestanding monolayer case, the

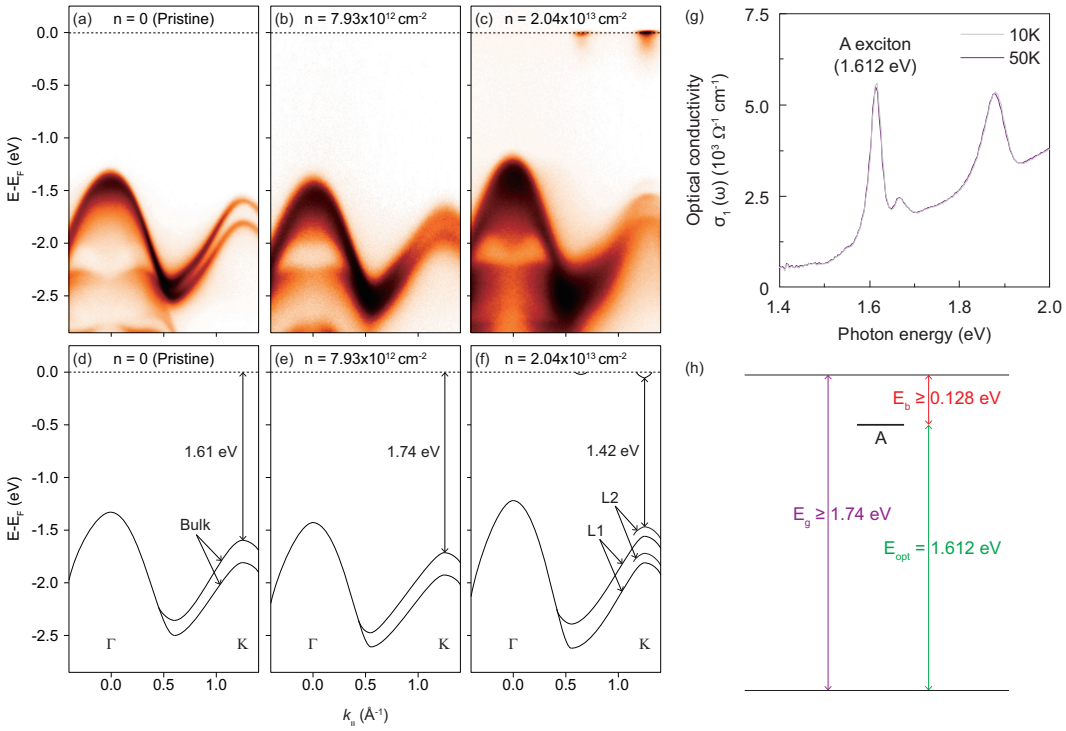

Fig. 6.5: Exciton binding energy of bulk $MoSe_2$. (a)-(c) *In-situ* Rb dosing ARPES raw data measured below 50 K. (d)-(f) Guide to eye for the raw data (a)-(c), respectively. (g) Optical conductivity data measured at 10 K and 50 K. There is no difference between 10 K and 50 K. (h) Exciton binding energy of bulk $MoSe_2$.

exciton binding energy increases even larger than 550 meV.

6.1.3 Motivations

There are two motivations of this work. One is the disparity in the exciton binding energy between extracting from absorption spectroscopy and subtracting optical band gap from ARPES quasiparticle band gap. In the past, the exciton binding energy usually measured only by optical spectroscopy. Figure 6.4 shows the transmission spectrum of bulk $MoSe_2$[72]. In this paper, they mentioned that origin of the lowest energy exciton is 1s state of A

exciton and second lowest one is 2s state of A exciton. Using this two peak energy, they deduce the exciton binding energy whose value is 67 meV.

However, when we compare the quasiparticle/electronic band gap (Figure 6.5 (b) and (e)) and optical band gap (Figure 6.5 (g)) of bulk $MoSe_2$ using ARPES and ellipsometry, respectively, we can determine that the minimum value of exciton binding energy is 128 meV as shown in Figure 6.5 (h). The reason why I use the word "minimum" is as follows. Here, we use the alkali metal evaporation method during ARPES measurement to extract the electronic band gap. In low electron density limit (Figure 6.5 (b)) before the conduction band minimum appears, we can extract the minimum value of the quasiparticle band gap. Here, the minimum means when we evaporate the alkali metal, excess electron is doped into the surface of the sample which induce screening. This screening makes the reduction of the quasiparticle band gap. If we evaporate more alkali metal, the conduction band minimum appears as shown in Figure 6.5 (c). In this evaporation level, due to more screening and electrical Stark effect, the quasiparticle band gap even more decreased. This is our first motivation of exciton binding energy study in bulk materials.

The second motivation is natural question about the relation between the dimensionality and exciton binding energy. As I mentioned before, usually bulk materials have small exciton binding energy. However, if bulk material have very weak interlayer coupling which indicates 3D but very 2D like, maybe it has quite large exciton binding energy. This is our second motivation of this work.

In order to study the exciton binding energy of bulk system, we need to choose the appropriate materials. How about the most famous TMDs, bulk MX_2? Unfortunately, MX_2 has not so weak interlayer coupling as already shown in Figure 3.3 (b)-(e). On the other hand, $ReSe_2$ has very weak interlayer coupling as shown in Figure 5.8. Due to this weak interlayer coupling, we select ReX_2 to study the exciton binding energy in bulk system.

6.2 Experiment

6.2.1 Scanning tunneling microscope (STM)

Tunneling spectroscopy has developed into a field of intensive research since its first application in 1961. In general, tunneling experiments are performed with metal-insulator-metal sandwich structures with a solid state insulator. This classical tunneling technique evidently has two inherent limitations. One is that once the tunnel junction has been made, access to the electrode surfaces for further treatment and investigation is lost. The other is that the information is averaged over an area limited in smallness by current lithographic techniques. However, using vacuum as tunnel barrier can resolve both of limitations. In addition, vacuum is conceptually the most simple tunnel barrier. The easiest application of vacuum tunneling is scanning tunneling spectroscopy (STM).

STM is one of most powerful experimental tools to investigate surfaces of solid systems at the atomic level. It consists essentially in scanning a metal tip over the surface to be investigated. The metal tip is fixed to a rectangular piezodrive, made out of commercial piezoceramic material. For an STM, good resolution is considered to be 0.1 nm lateral resolution and 0.01 nm (10 pm) depth resolution. Due to this extremely high resolution, individual atoms within materials are routinely imaged and manipulated by topographic technique during STM measurement. Other strength of STM is that the STM can be used not only in ultra-high vacuum but also in air, water, and various other liquid or gas ambients, and at temperatures ranging from near zero kelvin to over 1000 C.

Here, we use scanning tunneling spectroscopy (STS), an extension of STM, to measure the electronic band gap. When a metal tip is brought very near to the surface, a bias voltage applied between the metal tip and surface of sample can allow electrons to tunnel through the vacuum between them. The resulting tunneling current is a function of tip position, applied voltage,

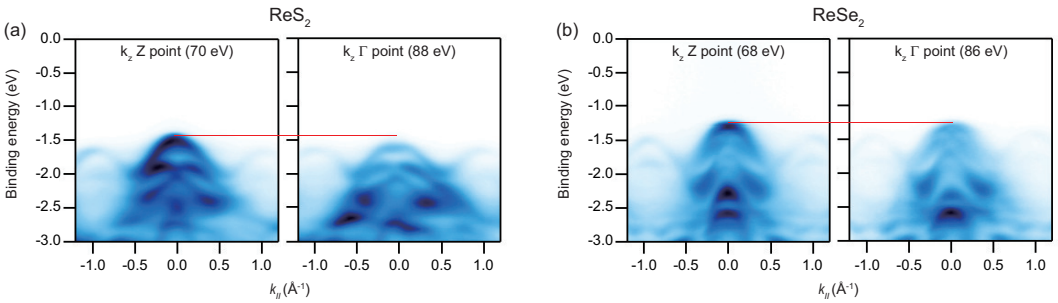

Fig. 6.6: High symmetry cut data along k_z direction of ReS_2 and $ReSe_2$. (a) ARPES raw data of ReS_2 at k_z Z point and Γ point. (b) ARPES raw data of $ReSe_2$ at k_z Z point and Γ point. All data were taken along the Re chain direction at 180 K. Red lines are guides to eye for the bandwidth of k_z dispersion.

and the local density of states (LDOS) of the sample. The change of the current with the energy of electrons is the simplest spectrum using STS. It is often referred to as an I-V curve. The slope of the I-V curve (dI/dV curve) corresponds to LDOS. Using this dI/dV curve, we can define the electronic band gap size of the system.

6.2.2 Ellipsometry

Ellipsometry is one of most popular optical measurement techniques to investigate light reflection or transmission from samples. The main feature of ellipsometry is that it measures the change of light polarization from incident photon to outgoing photon. Ellipsometry mainly measure the two values. One is amplitude ratio (ψ) and the other is phase difference (Δ) between light polarization (s- and p-polarization). These two values are measured by changing the wavelength of light. In ellipsometry measurement, one can extract the absorption coefficient or optical conductivity from these measured two values. Generally, the spectroscopic ellipsometry can measure ranging from infrared to ultraviolet/visible region.

There are two general limitations on the spectroscopic ellipsometry mea-

surement. One is that surface roughness of samples has to be small. If the size of surface roughness exceeds around 30% of a measurement wavelength, errors generally increase. The other is that the measurement must be performed at oblique incidence of light source. In spite of these limitations, the spectroscopic ellipsometry has a strong advantage to study samples. The spectroscopic ellipsometry can measure the all kind of samples such as metals, insulators, and semiconductors regardless of the band gap characters (Indirect or direct).

The spectra from the optical measurement including spectroscopic ellipsometry are always related to the exciton and optical band gap. In absorption spectra which can be extracted by spectroscopic ellipsometry, the peak correspond to the exciton state. Position of the lowest energy exciton state is optical band gap.

6.3 Result and discussion

6.3.1 k_z dispersion of ReX_2

First of all, we need to check whether ReX_2 have really 2D like feature or not. As I briefly introduced, we measure the photon energy dependent (k_z dependent) ARPES. Here, we precisely examine the k_z dispersion of ReS_2 and $ReSe_2$. Though I already show the k_z dependent ARPES data of both materials in Figure 5.8, it is worth to check the valence band maximum position of high symmetry point along k_z direction (Γ and Z point) to see the bandwidth of k_z dispersion.

Figure 6.6 (a) shows the valence band dispersion of ReS_2 at Z point and Γ point and Figure 6.6 (b) shows the valence band dispersion of $ReSe_2$ at same high symmetry points. For the ReS_2, the Z point and Γ point correspond to 70 and 88 eV, respectively. $ReSe_2$ also has similar photon energy for high symmetry point, 68 and 86 eV. There are red lines in Figure 6.6 (a) and (b) which are guides to eye for energy difference of valence band maximum

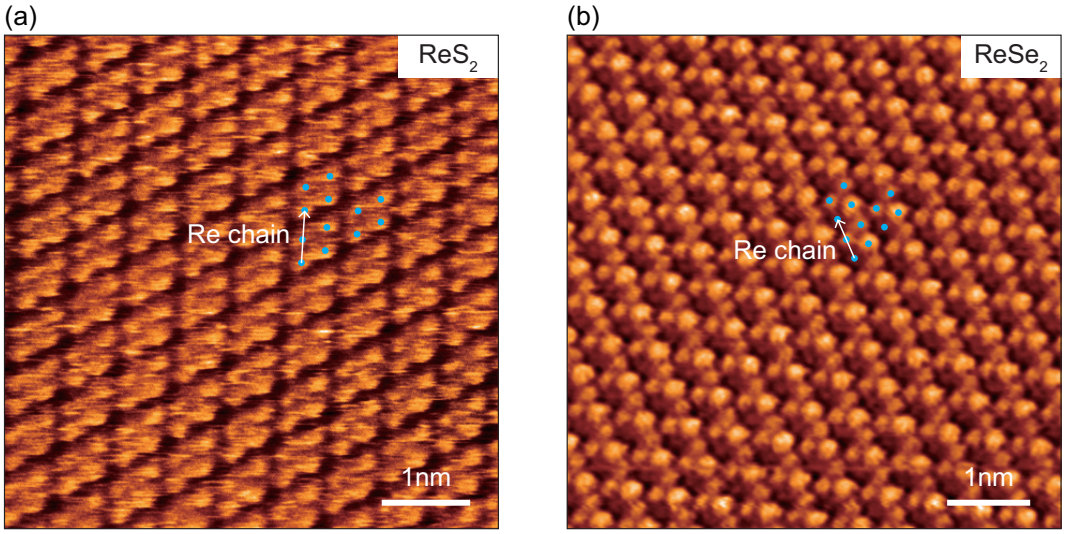

Fig. 6.7: Topography images of bulk ReS_2 and $ReSe_2$. (a) and (b) are topography images of bulk ReS_2 and $ReSe_2$, respectively. Blue dots in (a) and (b) indicate Re atoms. Re chain direction is marked using white arrow. Scale bar is 1nm.

between Z and Γ point. The energy difference in ReS_2 is about 150 meV. On the other hand, that in $ReSe_2$ is about 20 meV. This indicates that $ReSe_2$ is almost 2D like character rather than ReS_2. Here, our hypothesis is that $ReSe_2$ might has a large exciton binding energy due to its 2D like character and ReS_2 should has a small exciton binding energy as usual. In order to check this, we measure the electronic band gaps of both materials using scanning tunneling spectroscopy (STS) and optical band gaps of both materials using optical spectroscopy (PL, ellipsometry).

6.3.2 Electronic band gap of ReX_2

Figure 6.7 shows the topography image from STM measurement of ReS_2 and $ReSe_2$. All atoms in both topography images are Re atoms. We couldn't take the image of chalcogen atoms due to the dominant Re d-orbital characters near the valence band maximum. As mentioned before, ReX_2 has Re chain

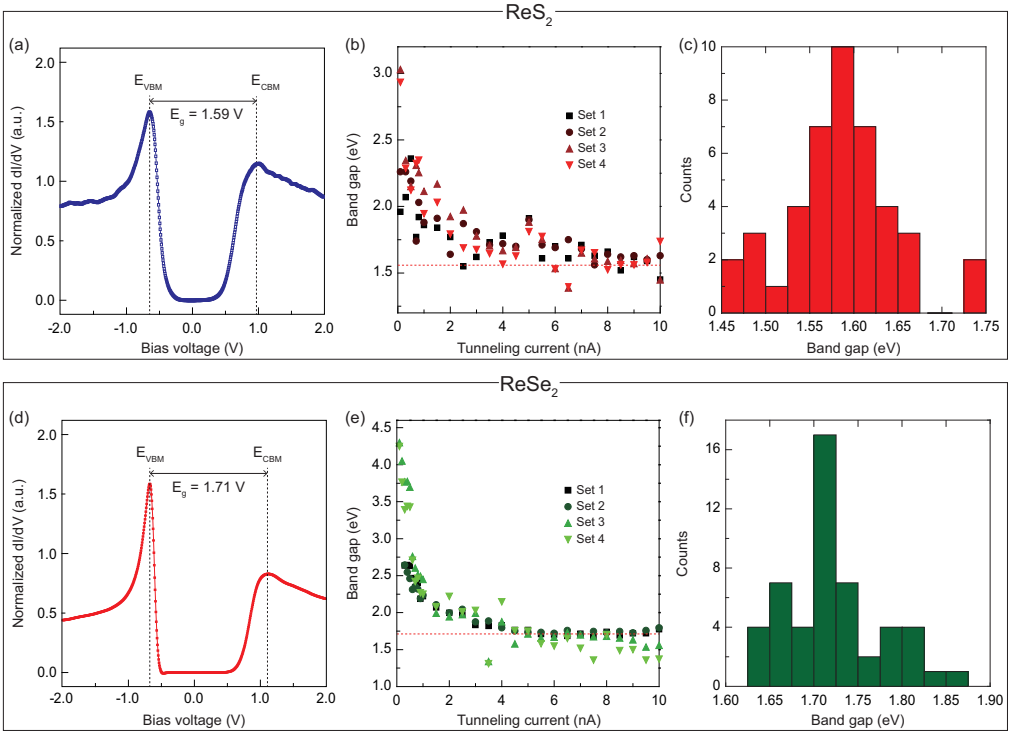

Fig. 6.8: STS data of bulk ReS_2 and $ReSe_2$. (a) Normalized dI/dV as a function of bias voltage in ReS_2. (b) Tunneling current dependent band gap size of ReS_2. (c) Histogram of the band gap size in ReS_2 (43 data points). (d) Normalized dI/dV data of $ReSe_2$ as a function of bias voltage. (e) Tunneling current dependent band gap size of $ReSe_2$. (f) Histogram of the band gap size in $ReSe_2$ (48 data points).

in their crystal structure which also clearly shown in our topography images (White arrow). We determine the Re chain direction using Fourier transformation for both topography images. All data are taken at 180 K to avoid the charging effect in bulk $ReSe_2$. In fact, ReS_2 can be measured around 80 K, but it is impossible to measure the topography image of $ReSe_2$ below 180 K due to high resistivity. This high resistivity in bulk $ReSe_2$ also can be another evidence that $ReSe_2$ has almost 2D like character.

After measuring topography images, we measure the scanning tunneling spectroscopy to determine the electronic band gap size of ReX_2. Figure 6.8

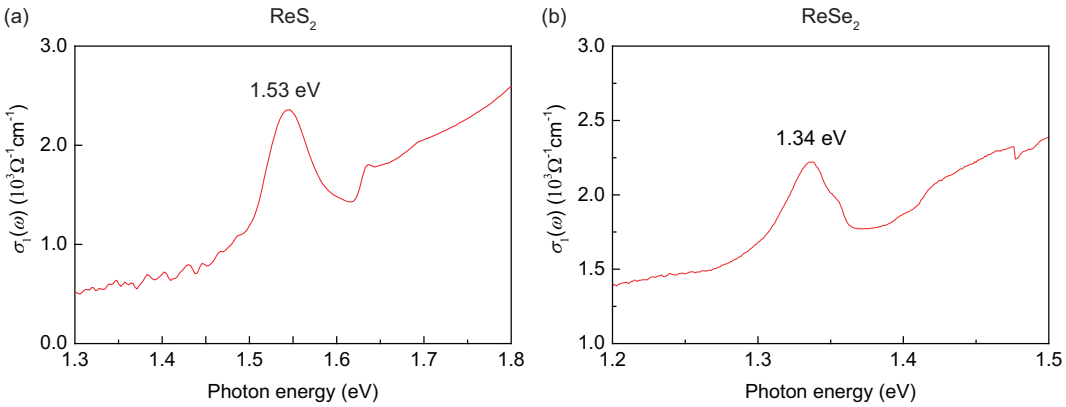

Fig. 6.9: Optical band gap of bulk ReS_2 and $ReSe_2$. All data were taken at 180 K. Bulk ReS_2 has 1.53 eV optical band gap and $ReSe_2$ has 1.34 eV optical band gap.

(a) and (d) shows the electronic band gaps of bulk ReS_2 and $ReSe_2$, respectively. While ReS_2 has 1.59 eV electronic band gap, $ReSe_2$ has 1.71 eV electronic band gap. These values are average value of more than 40 points as shown in Figure 6.8 (c) and (f). Figure 6.8 (b) and (e) are tunneling current dependent electronic band gaps of ReS_2 and $ReSe_2$, respectively.

In our data, there is no signal of tip induced band bending (TIBB). If there is TIBB, electronic band gap increases as tunneling current increases. However, our data show the saturation of the electronic band gap as tunneling current increases. In low tunneling current region, the distance between tip and sample is too large to measure electronic band gap accurately. For precise measurement, we measure the tunneling current dependent STS of all data points and average the band gap value between the 5 nA to 10 nA tunneling current which almost saturated.

Here, we plot the normalized dI/dV as a function of bias voltage. We assume that (I/V)(dI/dV) = $constant$ which widely used for normalization of dI/dV. Due to our finite measurement temperature, there should exist thermal broadening and other effects in STS data. For these reasons, extracting electronic band gap from onsets of valence band and conduction band edge

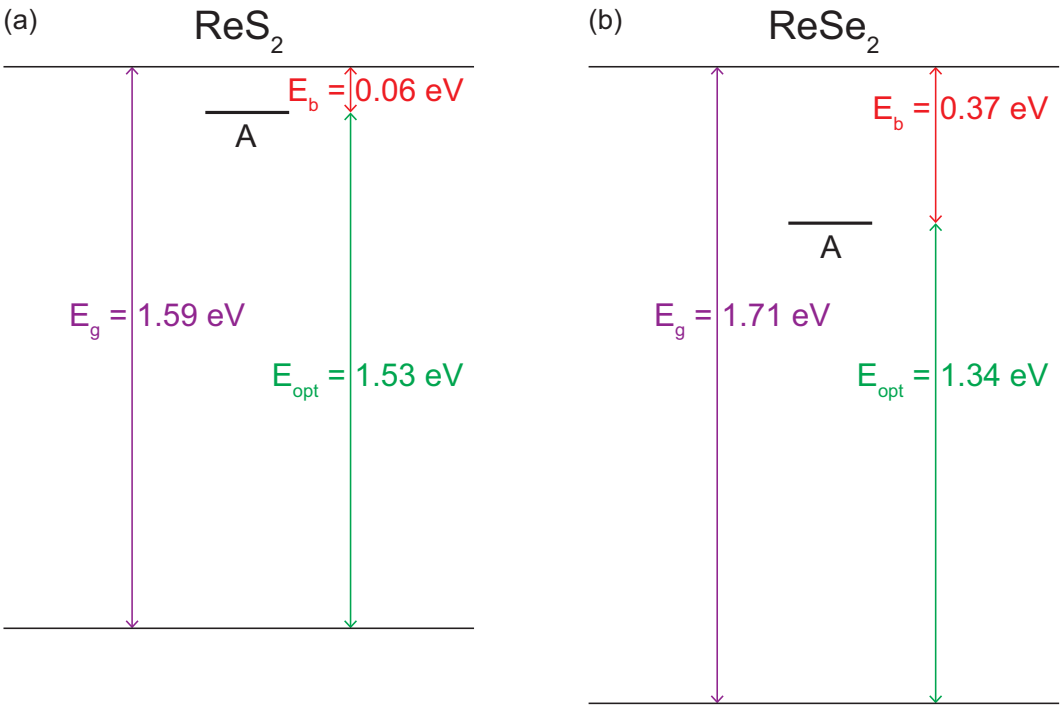

Fig. 6.10: Exciton binding energy of bulk ReS_2 and $ReSe_2$. Summarizing schematic band diagram of electronic band gap, optical band gap, and exciton binding energy of (a) bulk ReS_2 and (b) bulk $ReSe_2$.

is unreasonable and inaccurate. Of course, we couldn't exactly determine the electronic band gap of both materials due to the finite temperature, however, at least we can determine the difference in the electronic band gap between ReS_2 and $ReSe_2$. Bulk $ReSe_2$ has 120 meV larger electronic band gap than bulk ReS_2.

6.3.3 Optical band gap of ReX_2

Figure 6.9 shows the optical band gaps of ReS_2 and $ReSe_2$ using ellipsometry. The optical band gaps have opposite pattern to the electronic band gaps. For the electronic band gap, $ReSe_2$ has larger value than ReS_2. On the contrary, for the optical band gap, ReS_2 has even larger value than $ReSe_2$. The size of

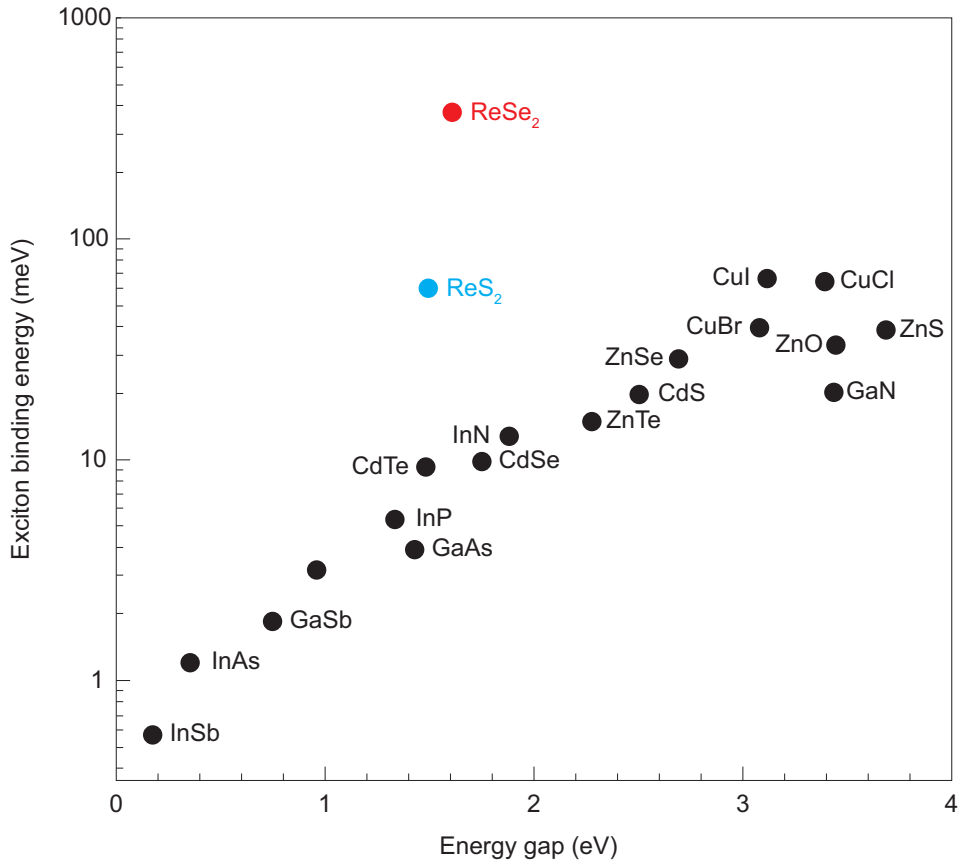

Fig. 6.11: Comparing exciton binding energy with other 3D semiconductors. Especially, bulk $ReSe_2$ is located far away from other 3D semiconductors.

optical band gap in ReS_2 is about 1.53 eV and in $ReSe_2$ is about 1.34 eV. All data were taken at 180 K to compare with STS data.

6.3.4 Exciton binding energy of ReX_2

Figure 6.10 shows the results from optical spectroscopy and STS of ReS_2 and $ReSe_2$. Subtracting optical band gaps from electronic band gaps gives exciton binding energies of both materials. As we expected, $ReSe_2$ has extremely large exciton binding energy (about 370 meV) even in bulk form due

to not only 2D character along out-of-plane direction but also 1D character in ab-plane of crystal structure. On the other hand, ReS_2 has quite small exciton binding energy (about 60 meV) which is comparable with other bulk semiconductors.

When we compare these two values with other 3D or 2D semiconductors, one can see how large the exciton binding energy of bulk $ReSe_2$ is. Figure 6.11 shows the exciton binding energies of 3D semiconductors as a function of electronic band gap size. Almost of 3D semiconductors have linear behavior in this Figure 6.11, however, bulk $ReSe_2$ is located far away from this linear scale. Here, y-axis (exciton binding energy) is log scale value.

On the other hand, comparing with 2D semiconductors, bulk $ReSe_2$ has quite well matched linear scaling behavior[73]. Figure 6.12 indicates the scaling universality between electronic band gaps and exciton binding energies of 2D monolayer semiconductors. Here, they proposed that electronic band gap is correspond to about 4 times exciton binding energy. Even in bulk form, as shown in Figure 6.12, bulk $ReSe_2$ has similar behavior with other 2D monolayer semiconductors.

6.3.5 Relation between exciton binding energy and two free parameters

We attribute this extraordinarily large exciton binding energy of bulk $ReSe_2$ to dielectric constant and effective mass along out-of-plane direction of crystal structure. The binding energy of ground exciton state in material is given by

$$E_b = -\frac{\mu^*_{e,h} e^4}{2\epsilon^2 \hbar^2} \tag{6.1}$$

where $\mu^*_{e,h}$ is reduced effective mass of lowest electron band and highest hole band, ϵ the dielectric constant of material, and e is elementary charge.

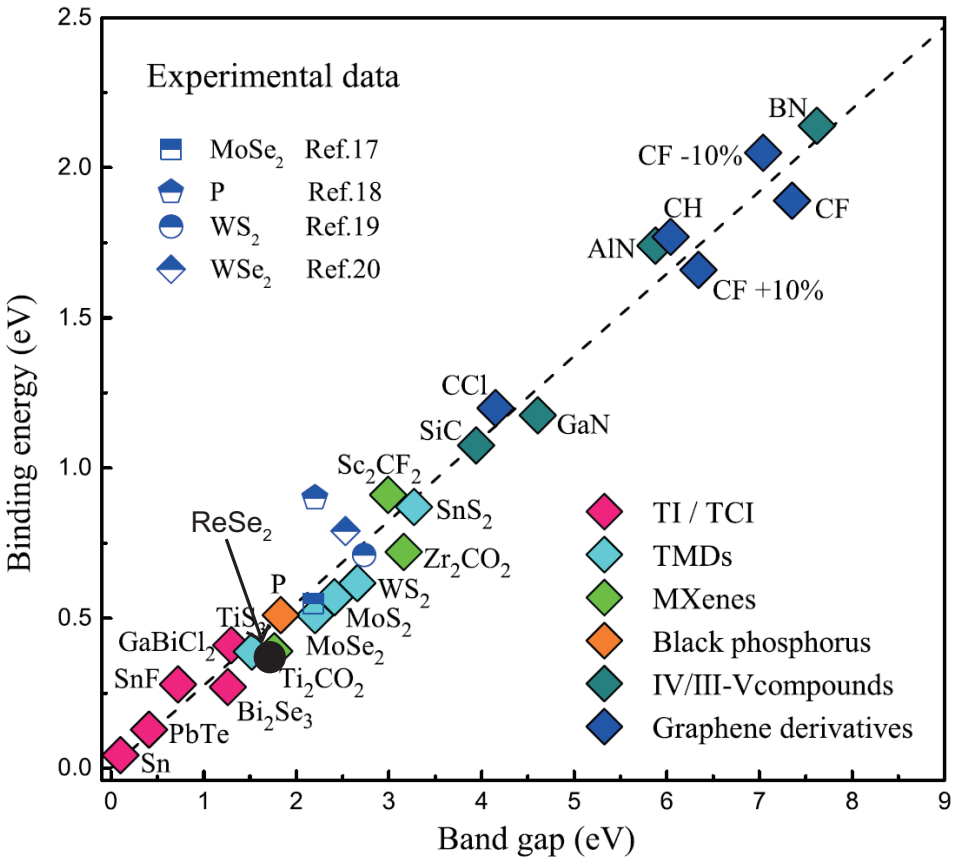

Fig. 6.12: Comparing exciton binding energy with other 2D semiconductors. There are theoretical value of exciton binding energy as a function of band gap except four experimental values.

There are two free (material dependent) parameters in this equation, $\mu^*_{e,h}$ and ϵ. The size of exciton binding energy is proportional to the reduce effective mass and square inverse proportional to the dielectric constant.

When we measure the dielectric constant along three direction (a-, b-, and c-axis), the main difference in dielectric constant of ReS_2 and $ReSe_2$ is along c-axis. The dielectric constant along c-axis of ReS_2 is about $15\epsilon_0$. On the other hand, the value of dielectric constant in $ReSe_2$ along c-axis is about $9\epsilon_0$. Here, ϵ_0 indicates dielectric constant of vacuum. The in-plane value is

almost same in both materials. This discrepancy can makes big difference in exciton binding energy.

Not only dielectric constant but also effective hole mass along k_z direction has large difference between bulk ReS_2 and $ReSe_2$. As shown in Figure 5.10 and Figure 5.11, effective hole masses along in-plane direction of both materials are almost same. However, there exists large difference in effective hole mass along out-of-plane (k_z) direction. The effective hole mass of bulk ReS_2 along k_z direction is about 7.2m_e. On the other hand, that of bulk $ReSe_2$ along k_z direction is about 52m_e.

From our results, these two large discrepancies in dielectric constant and effective hole mass along out-of-plane direction of ReS_2 and $ReSe_2$ make dramatic difference in exciton binding energy. Though we couldn't measure the effective mass of electron bands of both materials, bulk $ReSe_2$ has enough reasons for such large exciton binding energy value.

6.4 Conclusion

In this study, we performed systematic electronic structure studies on bulk ReS_2 and $ReSe_2$ using various spectroscopic techniques including ARPES, STM and optical spectroscopies. From the ARPES data, we reveal that the bandwidth of $ReSe_2$ is much smaller than that of ReS_2 which indicates heavier effective hole mass in $ReSe_2$ than ReS_2. Using this result as a motivation of this study, we measured electronic band gap and optical band gap of both materials by STS and optical spectroscopies, respectively. Comparing two band gaps of ReS_2 and $ReSe_2$, we determine the exciton binding energies of both materials. Even in bulk form, $ReSe_2$ has extraordinarily large exciton binding energy. We attribute this to large effective hole mass along k_z direction in momentum space and small dielectric constant along c-axis in real space. This study can pave a new way for measuring exciton binding energy in bulk materials. Also, by substituting Se atoms to S atoms (ReS_xSe_{2-x}),

there exists large possibility for tuning the exciton binding energy from 60 meV to 370 meV.

7 Summary

In this thesis, I mainly study the comprehensive electronic structures of bulk semiconducting transition metal dichalcogenides with direct and indirect band gaps. Through chapter 3 and 4, band parameters and band gap tuning of indirect band gap semiconductors, group 6 TMDs MX_2, have been discussed. In chapter 5 and 6, electronic band structure and exciton binding energy of direct band gap semiconductors, group 7 TMDs ReX_2, have been discussed. I mainly used ARPES technique to investigate electronic structures of TMDs. For studying exciton binding energy in chapter 6, I also used STM and optical spectroscopy (Ellipsometry) with the support from my collaborators.

In chapter 3, band parameters including conduction band minimum position, indirect band gap size, direct band gap size at K point, and SOI induced spin-band splitting size are revealed by using $in\text{-}situ$ alkali metal dosing ARPES. For the MoS_2 and $MoSe_2$, unlike what is known, the conduction band minimum position is located at the K point. Another remarkable point is that the energy difference between valence band maximum at K and Γ point decreases from S atom to Se atom. Lastly, by comparing the band parameters with other published papers including studies on monolayer and multilayer thin films, I demonstrated the effect of the number of layers and substrate.

By using $in\text{-}situ$ alkali metal evaporation method, I systematically studied electric field effect on the band gap size and strong possibility of indirect to direct band gap transition in bulk $MoSe_2$. I attributed the tunable band gap to the electron doping effect, screening effect, and electrical Stark effect.

In low electron density, there exist the electron doping effect and screening effect from excess charges from surface Rb atoms. However, in high electron density, there is one additional effect so called electrical Stark effect from surface Rb layer. By changing electron density, I extract the critical electron density which can induce the indirect to direct band gap transition.

In chapter 5, moving from indirect band gap semiconductors to direct band gap semiconductors, I investigated the electronic band structure of group 7 TMDs ReX_2. ReX_2 is recently highlighted material due to weak interlayer coupling and monolayer behavior even in bulk form. Also, ReX_2 has high anisotropy due to their triclinic crystal structure. I systematically extracted the angle dependent effective hole mass of ReS_2 and $ReSe_2$. In addition, I address the issue about conduction band minimum position of $ReSe_2$. From the photon energy dependent ARPES measurement, I reveal that ReS_2 has quite large bandwidth along the k_z direction (large k_z dispersion/light effective hole mass) which indicates 3D nature, whereas $ReSe_2$ has very small bandwidth along the k_z direction (small k_z dispersion/heavy effective hole mass). This 2D character of $ReSe_2$ is connected to the motivation of the research in the next chapter.

Finally, in chapter 6, we investigated the exciton binding energies of bulk ReS_2 and $ReSe_2$ subtracting optical band gap from electronic band gap measured by STS and optical spectroscopy, respectively. There is disparity between exciton binding energy extracting from only optical spectroscopy and subtracting optical band gap from quasiparticle/electronic band gap from ARPES. This indicates that deduced exciton binding energy only by optical spectroscopy can underestimate the value of exciton binding energy. In addition, we thought that if material has small k_z dispersion, it might have large exciton binding energy even in bulk form. Bulk ReX_2 is one of good candidates to address this two possible scenarios due to its 2D character and direct band gap nature. In order to extract the exciton binding energies of both materials, we used STS and optical spectroscopy. From the results of STS and optical spectroscopy at 180 K, we successfully extract the exciton

binding energies of ReS_2 and $ReSe_2$. As we expected, $ReSe_2$ has extraordinarily large exciton binding energy, whereas ReS_2 has small exciton binding energy. Consequently, we reveal that bulk materials also can have large exciton binding energy and extracting the exciton binding energy only by optical spectroscopy can underestimate the value of exciton binding energy. We also provide the possibility of tuning the exciton binding energy by substituting chalcogen atoms from S to Se.

For the future, I will study the new state of ReX_2 induced by the alkali metal evaporation. When I dosed alkali metal on the surface of ReX_2, there is no electron doping or electric field effect. Instead, there are two new bands which have dispersion and structure. In the low dosing limit, Brillouin zone of this new state is rectangular shape. On the other hand, in high dosing limit, the shape of unit cell changes from rectangular to triangle. I will study this exotic new state from alkali metal on the ReX_2.

Bibliography

[1] H. W. Kroto, J. R. Heath, S. C. O'Brien, R. F. Curl, and R. E. Smalley, Nature **318**, 162 (1985).

[2] S. Iijima, Nature **354**, 56 (1991).

[3] K. S. Novoselov, A. K. Geim, S. V. Morozov, D. Jiang, Y. Zhang, S. V. Dubonos, I. V. Grigorieva, and A. A. Firsov, Science **77**, 3419 (1996).

[4] A. H. Castro Neto, F. Guinea, N. M. R. Peres, K. S. Novoselov, and A. K. Geim, Rev. Mod. Phys. **81**, 109 (2009).

[5] Y. Zhang, T.-R. Chang, B. Zhou, Y.-T. Cui, H. Yan, Z. K. Liu, F. Schmitt, J. Lee, R. Moore, Y. Chen, H. Lin, H.-T. Jeng, S.-K. Mo, Z. Hussain, A. Bansil, and Z.-X. Shen, Nat. Nanotech. **9**, 111-115 (2014).

[6] J. M. Lu, O. Zheliuk, I. Leermakers, N. F. Q. Yuan, U. Zeitler, K. T. Law, and J. T. Ye, Science **350**, 1353-1357 (2015).

[7] P. Chen, W. W. Pai, Y.-H. Chan, A. Takayama, C.-Z. Xu, A. Karn, S. Hasegawa, M. Y. Chou, S.-K. Mo, A.-V. Fedorov, and T.-C. Chiang, Nat. Commun. **8**, 516 (2017).

[8] J. Kim, S. S. Baik, S. H. Ryu, Y. S. Sohn, S. H. Park, B.-G. Park, J. D. Denlinger, Y. J. Yi, H. J. Choi, and K. S. Kim, Science **349**, 723-726 (2015).

[9] N. Ehlen, A. Sanna, B. V. Senkovskiy, L. Petaccia, A. V. Fedorov, G. Profeta, and A. Grüneis, Phys. Rev. B **97**, 045143 (2018).

[10] S. Manzeli, D. Ovchinnikov, D. Pasquier, O. V. Yazyev, and A. Kis, Nat. Rev. Mater. **2**, 17033 (2017).

[11] J. H. Kim, X. P. Hong, C. H. Jin, S.-F. Shi, C.-Y. S. Chang, M.-H. Chiu, L.-J. Li, and F. Wang, Science **346**, 1205-1208 (2014).

[12] R. Wakatsuki, Y. Saito, S. Hoshino, Y. M. Itahashi, T. Ideue, M. Ezawa, Y. Iwasa, and N. Nagaosa, Sci. Adv. **3**, e1602390 (2017).

[13] N. Alidoust, G. Bian, S.-Y. Xu, R. Sankar, M. Neupane, C. Liu, I. Belopolski, D.-X. Qu, J. D. Denlinger, F.-C. Chou, and M. Z. Hasan, Nat. Commun. **5**, 4673 (2014).

[14] J. M. Riley, F. Mazzola, M. Dendzik, M. Michiardi, T. Takayama, L. Bawden, C. Granerød, M. Leandersson, T. Balasubramanian, M. Hoesch, T. K. Kim, H. Takagi,W. Meevasana, Ph. Hofmann, M. S. Bahramy, J. W. Wells, and P. D. C. King, Nat. Phys. **10**, 835-839 (2014).

[15] S. X. Yang, S. Tongay, Q. Yue, Y. T. Li, B. Li, and F. Y. Lu, Sci. Rep. **4**, 5442 (2014).

[16] E. Liu, M. S. Long, J. Zeng, W. Luo, Y. J. Wang, Y. Pan, W. Zhou, B. G. Wang, W. Hu, Z. H. Ni, Y. You, X. Zhang, S. Q. Qin, Y. Shi, K. Watanabe, T. Taniguchi, H. T. Yuan, H. Y. Hwang, Y. Cui, F. Miao, and D. Y. Xing, Adv. Funct. Mater. **26**, 1938-1944 (2016).

[17] L. S. Hart, J. L. Webb, S. Dale, S. J. Bending, M. Mucha-Kruczynski, D. Wolverson, C. Chen, José Avila, and M. C. Asensio, Sci. Rep. **7**, 5145 (2017).

[18] P. Eickholt, J. Noky, E. F. Schwier, K. Shimada, K. Miyamoto, T. Okuda, C. Datzer, M. Drüppel, P. Krüger, M. Rohlfing, and M. Donath, Phys. Rev. B **97**, 165130 (2018).

[19] S. Tongay, H. Sahin, C. H. Ko, A. Luce, W. Fan, K. Liu, J. Zhou, Y.-S. Huang, C.-H. Ho, J. Y. Yan, D. F. Ogletree, S. Aloni, J. Ji, S. S. Li, J. Li, F. M. Peeters, and J. Q. Wu, Nat. Commun. **5**, 3252 (2014).

[20] S. W. Sim, D. Lee, M. J. Noh, S. Y. Cha, C. H. Soh, J. H. Sung, M.-H. Jo, and H. Y. Choi, Nat. Commun. **7**, 13569 (2016).

[21] D. Wolverson, S. Crampin, A. S. Kazemi, A. Ilie, and S. J. Bending, ACS Nano **8**, 11154-11164 (2014).

[22] Y. Q. Feng, W. Zhou, Y. J. Wang, J. Zhou, E. Liu, Y. Fu, Z. H. Ni, X. L. Wu, H. Yuan, F. Miao, B. G. Wang, X. G. Wan, and D. Xing, Phys. Rev. B **92**, 054110 (2015).

[23] A. Damascelli, Z. Hussain, and Z. X. Shen, Rev. Mod. Phys. **75**, 473 (2003).

[24] H. Hertz, Ann. Phys. **17**, 983 (1887).

[25] A. Einstein, Ann. Phys. **31**, 132 (1905).

[26] S. Hüfner, *Photoelectron spectroscopy : principles and application*, Oxford University, New York : Springer-Verlag, 1995.

[27] http://web.stanford.edu/ bmoritz/ARPES.html

[28] S. R. Park, J. H. Han, C. Kim, Y. Y. Koh, C. Kim, H. J. Lee, H. J. Choi, J. H. Han, K. D. Lee, N. J. Hur, M. Arita, K. Shimada, H. Namatame, and M. Taniguchi, Phys. Rev. Lett. **108**, 046805 (2012).

[29] B. S. Kim, W. S. Kyung, J. J. Seo, J. Y. Kwon, J. D. Denlinger, C. Kim, and S. R. Park, Sci. Rep. **7**, 5206 (2017).

[30] J. J. Seo, B. Y. Kim, B. S. Kim, J. K. Jeong, J. M. Ok, J. S. Kim, J. D. Denlinger, S.-K. Mo, C. Kim, and Y. K. Kim, Nat. Commun. **7**, 11116 (2016).

[31] W. S. Kyung, S. S. Huh, Y. Y. Koh, K.-Y. Choi, M. Nakajima, H. Eisaki, J. D. Denlinger, S.-K. Mo, C. Kim, and Y. K. Kim, Nat. Mater. **15**, 1233-1236 (2016).

[32] T. Ohta, A. Bostwick, T. Seyller, K. Horn, and E. Rotenberg, Science **313** 5789, 951-954 (2006).

[33] Z.-H. Zhu, G. Levy, B. Ludbrook, C. N. Veenstra, J. A. Rosen, R. Comin, D. Wong, P. Dosanjh, A. Ubaldini, P. Syers, N. P. Butch, J. Paglione, I. S. Elfimov, and A. Damascelli, Phys. Rev. Lett. **107**, 186405 (2011).

[34] Y. K. Kim, O. Krupin, J. D. Denlinger, A. Bostwick, E. Rotenberg, Q. Zhao, J. F. Mitchell, J. W. Allen, and B. J. Kim, Science **345**, 6193, 187-190 (2014).

[35] A. K. Geim, and K. S. Novoselov, Nat. Mater. **6**, 183-191 (2007).

[36] D. Xiao, G.-B. Liu, W. X. Feng, X. D. Xu, and W. Yao, Phys. Rev. Lett. **108**, 196802 (2012).

[37] J. A. Miwa, S. Ulstrup, S. G. Sørensen, M. Dendzik, A. G. Čabo, M. Bianchi, J. V. Lauritsen, and P. Hofmann, Phys. Rev. Lett. **114**, 046802 (2015).

[38] M. Dendzik, M. Michiardi, C. Sanders, M. Bianchi, J. A. Miwa, S. S. Grønborg, J. V. Lauritsen, A. Bruiz, B. Hammer, and P. Hofmann, Phys. Rev. B **92**, 245442 (2015).

[39] B. S. Kim, J.-W. Rhim, B. Y. Kim, C. Kim, and S. R. Park, Sci. Rep. **6**, 36389 (2016).

[40] S. Fang, R. KuateDefo, S. N. Shirodkar, S. Lieu, G. A. Tritsaris, and E. Kaxiras, Phys. Rev. B **92**, 205108 (2015).

[41] X. Su, R. Z. Zhang, C. F. Guo, M. Guoc, and Z. Y. Rena, Phys. Chem. Chem. Phys. **16**, 1393 (2014).

[42] J. A. Stewart and D. E. Spearot, Modelling Simul. Mater. Sci. Eng. **21**, 045003 (2013).

[43] C. D. Zhang, A. Johnson, C.-L. Hsu, L.-J. Li, and C.-K. Shin, Nano Lett. **14**, 2443-2447 (2014).

[44] Y. L. Huang, Y. F. Chen, W. J. Zhang, S. Y. Quek, C.-H. Chen, L.-J. Li, W.-T. Hsu, W.-H. Chang, Y. J. Zheng, W. Chen, and A. T. S. Wee, Nat. Commun. **6**, 6298 (2015).

[45] M. M. Ugeda, A. J. Bradley, S.-F. Shi, F. H. da Jornada, Y. Zhang, D. Y. Qiu, W. Ruan, S.-K. Mo, Z. Hussain, Z.-X. Shen, F. Wang, S. G. Louie, and M. F. Crommie, Nat. Mater. **13**, 1091-1095 (2014).

[46] Y. Zhang, M. M. Ugeda, C. H. Jin, S.-F. Shi, A. J. Bradley, A. Martín-Recio, H. J. Ryu, J. H. Kim, S. J. Tang, Y. K. Kim, B. Zhou, C. G. Hwang, Y. L. Chen, F. Wang, M. F. Crommie, Z. Hussain, Z.-X. Shen, S.-K. Mo, Nano Lett. **16**, 2485-2491 (2016).

[47] J. M. Riley, W. Meevasana, L. Bawden, M. Asakawa, T. Takayama, T. Eknapakul, T. K. Kim, M. Hoesch, S.-K. Mo, H. Takagi, T. Sasagawa, M. S. Bahramy, and P. D. C. King, Nat. Nanotech. **10**, 1043-1047 (2015).

[48] K. P. Dhakal, D. L. Duong, J. B. Lee, H. G. Nam, M. S. Kim, M. Kan, Y. H. Lee, and J. Y. Kim, Nanoscale **6**, 13028-13035 (2014).

[49] K. H. Khoo, M. S. C. Mazzoni, and S. G. Louie, Phys. Rev. B **69**, 201401 (2004).

[50] F. Zheng, Z. R. Liu, J. Wu, W. H. Duan, and B.-L. Gu, Phys. Rev. B **78**, 085423 (2008).

[51] Y. Zhang, T.-T. Tang, C. Girit, Z. Hao, M. C. Martin, A. Zettl, M. F. Crommie, Y. R. Shen, and F. Wang, Nature **459**, 820-823 (2009).

[52] Z. Yang, and J. Ni, J. Appl. Phys. **107**, 104301 (2010).

[53] A. Ramasubramaniam, D. Naveh, and E. Towe, Phys. Rev. B **84**, 205325 (2011).

[54] H. Yuan, M. S. Bahramy, K. Morimoto, S. Wu, K. Nomura, B.-J. Yang, H. Shimotani, R. Suzuki, M. Toh, C. Kloc, X. Xu, R. Arita, N. Nagaosa, and Y. Iwasa, Nat. Phys. **9**, 563-569 (2013).

[55] T. Chu, H. Ilatikhameneh, G. Klimeck, R. Rahman, and Z. H. Chen, Nano Lett. **15**, 8000-8007 (2015).

[56] S. I. Mouri, Y. Miyauchi, and K. N. Matsuda, Nano Lett. **13**, 5944-5948 (2013).

[57] Y. F. Chen, J. Y. Xi, D. O. Dumcenco, Z. Liu, K. Suenaga, D. Wang, Z. G. Shuai, Y.-S. Huang, and L. Xie, ACS Nano **7**, 4610-4616 (2013).

[58] H. J. Conley, B. Wang, J. I. Ziegler, R. F. Haglund Jr., S. T. Pantelides, and K. I. Bolotin, Nano Lett. **13**, 3626-3630 (2013).

[59] K. L. He, C. Poole, K. F. Mak, and J. Shan, Nano Lett. **13**, 2931-2936 (2013).

[60] Y. F. Liang, and L. Yang, Phys. Rev. Lett. **114**, 063001 (2015).

[61] D. Biswas, A. M. Ganose, R. Yano, J. M. Riley, L. Bawden, O. J. Clark, J. Feng, L. Collins-Mcintyre, M. T. Sajjad, W. Meevasana, T. K. Kim, M. Hoesch, J. E. Rault, T. Sasagawa, D. O. Scanlon, and P. D. C. King, Phys. Rev. B **96**, 085205 (2017).

[62] S. M. Gunasekera, D. Wolverson, L. S. Hart, and M. Mucha-Kruczynski, J. Electron. Meter. **47**, 4314 (2018).

[63] A. Arora, J. Noky, M. Drüppel, B. Jariwala, T. Deilmann, R. Schneider, R. Schmidt, O. D. Pozo-Zamudio, T. Stiehm, A. Bhattacharya, P. Krüger, S. Michaelis de Vasconcellos, M. Rohlfing, and R. Bratschitsch, Nano Lett. **17**, 3202-3207 (2017).

[64] C. H. Ho, Y. S. Huang, P. C. Liao, and K. K. Tiong, J. Phys. Chem. Solids **60**, 1797-1804 (1999).

[65] M. Bovet, S. van Smaalen, H. Berger, R. Gaal, L. Forró, L. Schlapbach, and P. Aebi, Phys. Rev. B **67**, 125105 (2003).

[66] P. Miró, M. Audiffred, and T. Heine, Chem. Soc. Rev. **43**, 6547-6554 (2014).

[67] N. Zibouche, P. Philipsen, A. Kuc, and T. Heine, Phys. Rev. B **90**, 125440 (2014).

[68] S. Yu, H. Zhu, K. Eshun, C. Shi, M. Zeng, and Q. Li, Appl. Phys. Lett. **108**, 191901 (2016).

[69] F. Xia, H. Wang, and Y. Jia, Nat. Commun. **5**, 4458 (2014).

[70] Y. Akahama, S. Endo, and S.-I. Narita, J. Phys. Soc. Jpn. **52**, 2148-2155 (1983).

[71] X. P. Hong, J. H. Kim, S.-F. Shi, Y. Zhang, C. H. Jin, Y. H. Sun, S. Tongay, J. Q. Wu, Y. F. Zhang, and F. Wang, Nat. Nanotech. **9**, 682-686 (2014).

[72] A. R. Beal, J. C. Knights, and W. Y. Liang, J. Phys. C: Solid State Phys. **5**, 3540 (1972).

[73] Z. Jiang, Z. R. Liu, Y. C. Li, and W. H. Duan, Phys. Rev. Lett. **118**, 266401 (2017).

국문 초록

벌크 전이금속 칼코겐화합물의 준입자 밴드 갭 및 엑시톤 결합 에너지에 대한 연구

최근 특이한 물리적 성질 및 장치로서의 도입 가능성으로 인하여 얇은 단층 영역의 이차원 물질에 대한 연구가 각광 받고 있다. 이러한 이차원 물질들은 부도체, 반도체, 준금속 및 금속의 성질들을 가지고 있으며, 넓은 영역의 광학적 성질 그리고 전기적 성질을 포함한다. 뿐만 아니라, 적당하고 조절 가능한 준입자 밴드 갭을 가지고 있다. 특히, 벌크 상태의 반도체 전이금속 칼코겐화합물은 단층과는 완전히 다른 성질을 띄기도 한다. 이러한 중요성에도 불구하고, 벌크 상태의 전이금속 칼코겐화합물에 대한 연구는 거의 되어 있지 않은 상태이다. 이 박사 학위 논문에서는, 각분해능 광전자 분광 실험, 광분광 실험, 주사 터널링 현미경 실험을 통한 반도체 전이금속 칼코겐화합물의 전자구조에 대해 자세한 연구를 진행하였다.

먼저, 각분해능 광전자 분광 실험을 통해 벌크 상태의 그룹 6 전이금속 칼코겐화합물 MX_2 (M = Mo, W; X = S, Se)의 전자구조에 대해 연구하였다. 이 물질들은 벌크 상태에서는 간접 밴드 갭을 가지고 있고, 단층 상태에서는 직접 밴드 갭을 가지고 있다. 또한 강한 스핀-궤도 결합으로 인해 브릴루앙 영역의 K 지점에서 스핀 밴드 나뉨을 가지고 있다. 단층의 경우에는 많은 연구가 진행이 된 반면, 벌크 상태의 물질에 대해서는 기본적인 전자구조 및 밴드 변수들 조차 연구가 되어 있지 않은 상태이다. 이 연구에서는, 각분해능 광전자 분광 장치를 통하여 반도체를 연구를 할 때, 어떤 식으로 밴드 갭의 크기 및 각종 변수들을 도출해 낼 수 있는지에 대해 방법론을 확립하였다.

다음으로는 간접 밴드 갭을 갖는 벌크 상태의 물질에 강한 표면 전기장을 인가하여 직접 밴드 갭으로 바꾸는 것에 대한 연구를 진행하였다. 또한, 전기장 뿐만 아니라 전자 도핑이 밴드 갭 크기 및 성질에 어떠한 영향을 미치는 지에 대한 연구도 진행하였다. 간접 밴드 갭의

경우에는 광학적인 효율이 직접 밴드 갭에 비하여 상대적으로 많이 떨어지기 때문에, 물질이 직접 밴드 갭을 갖는 것은 매우 중요하다. 그렇기 때문에, 외부의 변수를 바꾸는 과정을 통하여 간접 밴드 갭을 직접 밴드 갭으로 바꾸는 것에 대한 연구가 활발히 진행되고 있고, 그 중에서도 외부의 전기장을 인가하면서 각분해능 광전자 분광 실험을 진행하였다. 일반적인 방법으로는 전기장을 인가할 수 없기에, 여기서는 알칼리 금속 분무라는 방법을 통하여 전기장이 전자구조에 미치는 영향에 대해 연구하였다. 이 연구에서는 외부 전기장을 통해 전자구조가 간접 밴드 갭에서 직접 밴드 갭으로 변화하는 것을 직접적으로 확인하였다.

여기서부터는 간접 밴드 갭이 아닌 직접 밴드 갭을 가지는 반도체에 대하여 연구를 진행하였다. 그룹 7 전이금속 칼코겐화합물 ReX_2 (X = S, Se)는 그룹 6과는 달리 직접 밴드 갭을 가지고 있다. 또한, 삼사정계의 구조를 가지고 있어서 위에서 구조를 봤을 때 한쪽 방향으로 Re 원자가 사슬 구조를 이루고 있다. 이러한 이유로, 전기적이나 광학적 측면에서 매우 비등방적인 성질을 띄고 있다. 이에 더하여, 다른 층간 물질에 비해 훨씬 더 약한 층간 결합을 가지고 있어서 단층과 벌크 상태의 성질이 거의 차이가 없는 물질로 각광받게 되었다. 하지만 위와 같은 흥미로운 성질에도 불구하고, 실험적인 전자구조에 대해서는 전혀 알려진 바가 없었다. 전기 혹은 광학 장치의 도입을 위해서는 전자구조에서 정공 밴드 혹은 전자 밴드가 어떠한 유효질량을 가지는지가 매우 중요하다. 본 연구에서는 각분해능 광전자 분광 실험을 통해 ReX_2 물질의 전자구조 및 정공 밴드의 유효질량에 대한 자세한 분석을 진행하였다.

마지막으로는 ReX_2 물질의 엑시톤 결합 에너지에 대하여 연구하였다. 밴드 갭은 두 가지 종류로 나뉜다. 하나는 준입자 밴드 갭 (전기적인 밴드 갭) 이고, 다른 하나는 광학적인 밴드 갭이다. 이 두 밴드 갭의 차이가 엑시톤 결합 에너지이다. 일반적으로 벌크 상태에서는 강한 스크리닝 환경 때문에, 엑시톤 결합 에너지가 작고, 단층에서는 상대적으로 약한 스크리닝 환경 때문에, 엑시톤 결합 에너지가 크다. 하지만 각분해능 광전자 분광 실험의 결과로 보면, $ReSe_2$의 경우에는 벌크 상태에서 다른 물질에 비해 엄청나게 작은 층간 결합을 가지고 있어서, 엑시톤 결합 에너지 값이 커질 수 있는 가능성을 내포하고 있다. 이를 정확하게 규명하기 위하여, 주사 터널링 현미경을 이용하여 전기적인 밴드 갭을 측정하고, 엘립소미터를 이용하여 광학적인 밴드 갭을 측정하여 ReX_2 물질의 엑시톤 결합 에너지를 도출해 내었다. 실제로 매우 결합이 약한 $ReSe_2$의 경우에는 370 meV라는 매우 큰 엑시톤 결합 에너지를 가지는 것

으로 나타났다. 반면, ReS_2의 경우에는 60 meV라는 일반적인 벌크 상태의 물질과 비슷한 수준의 엑시톤 결합 에너지를 가지는 것을 확인했다. 더 나아가, S와 Se를 치환하게 되면, 엑시톤 결합 에너지를 조절할 수도 있다는 가능성을 제시하였다.

주요어: 각분해능 광전자 분광 실험, 전이금속 칼코겐화합물, 준입자 밴드 갭, 엑시톤 결합 에너지, 알칼리 금속 분무, 전자구조

학번: 2015-30972